Electrostatic Interactions of Non-Polar Colloidal System and Implications for Industrial Applications

by

Mohamad Danial Shafiq

A dissertation submitted to the University of Bristol
in accordance with the requirements for award
of the degree of Doctor of Philosophy in the

Faculty of Science

2019

Word count: 45600

Declaration of Authorship

I declare that the work in this dissertation was carried out in accordance with the requirements of the University's Regulations and Code of Practice for Research Degree Programmes and that it has not been submitted for any other academic award. Except where indicated by specic reference in the text, the work is the candidate's own work. Work done in collaboration with, or with the assistance of, others, is indicated as such. Any views expressed in the dissertation are those of the author.

Signed: _____

Date: _____

"Acquire knowledge, and learn tranquility and dignity."

"Raihlah ilmu, dan untuk meraih ilmu, belajarlah tenang dan sabar."

Umar ibn Al-Khattab

Abstract

Colloidal science is vital in many industrial processes due to its outstanding properties, viability and versatility to tailor numerous industrial applications such as formulations in food and beauty products, decorative layering and painting as well as ink and electronic printing. Hence, the stability of a colloidal system is an important key to determine the final properties of the colloidal-based products. The stability of colloids by electrostatic means in a fluid is outlined by the Derjaguin-Landau-Verwey-Overbeek (DLVO) theory and the behaviour of colloids in the non-aqueous system is still uncertain despite its' importance in industrial applications. The main objective of this thesis is primarily to investigate the electrostatic interactions, mainly between colloidal particles in non-aqueous systems which can be applied to industrial needs such as printing and coating.

We generate controllable micrometer-range electrostatic interactions in a suspension by using a charge control additive (the surfactant, dioctyl sodium sulfosuccinate [AOT]), and an organic salt, tetradodecylammonium tetrakis (3,5-bis (trifluoromethyl)phenyl)borate (TDAT) in non-aqueous solvents. Both systems adapted different mechanisms of altering the electrostatic interaction between PMMA colloids. For AOT system, the particle surface charge is modified by adsorption of charged and neutral AOT micelles on the surface, hence affecting the interactions between particles. For the electrolytic TDAT non-aqueous system, the screening length of the solution was altered due to the presence of free ions in the solution. This is confirmed by the conductivity and theoretical Debye length values. However, from force measurement using the blinking optical tweezers (BOT), we found out that the measured screening length shows a non-monotonic dependence on the TDAT concentration. The deviation between these values revealed that at high TDAT concentrations, the classical DLVO theory is no longer valid for the system. We postulate that the formation of Janus-like particles due to charge instability resulted from the non-uniform charge distribution on the colloidal surfaces. This is preliminarily confirmed by the rotation of a PMMA colloids chain when an electric field is applied.

In a later series, the electrostatic interactions between charged PMMA colloids were investigated in an ionic liquid solution. The correlation between the number of ions in solution and the screening length was reported and the usual trend observed. The particle attraction was observed in all systems, which leads to the formation of colloidal clusters and aggregates. At high ionic liquid concentrations, we discovered that the colloidal stabilization is achieved and this may be due to the decaying particle aggregation rate, driven by the enhanced viscosity of the solution.

We relate the formation of clusters and aggregates formed in the bulk system with the deposition patterns of a colloidal droplet on a hydrophobically-coated glass substrate. The drying of droplets containing monodisperse PMMA particles was studied by confocal light scanning microscopy. Image analysis was used to quantify the spatial deposition of the particles. We explore the competition between the long-range colloidal force with the evaporation kinetics of the solvent. In highly-volatile solvents, such as hexane, hydrodynamic flows dominate particle deposition. With weak electrostatic interactions, a well-defined coffee-ring is produced. Increasing the strength of repulsions, the intensity of the 'ring' is observed to first reduce and then in highly-charged systems to be totally suppressed. In less volatile solvents, such as dodecane where evaporation is diffusion-controlled, the role of colloidal

forces is more complex with evidence for modification of both particle-particle and particle-substrate interactions. Finally, high TDAT concentrations induce particles attraction and the formation of clusters in bulk solution which inhibit the formation of a ring-like deposit.

Acknowledgements

Firstly, I would like to express my gratitude to my project supervisor, Professor Paul Bartlett for sharing his extensive knowledge on soft matter science through stimulating discussions and meetings. His guidance and general concern have immensely inspired me to understand further and helped me went through the challenges, academically and in life. My sincere gratitude to Franceska Waggett, whom I have been working with for the last few years and primarily involved in projects and experiments and also the preparation of this thesis and research papers. Her constant support, encouragement and guidance have significantly progressed my enthusiasm to work efficiently and productively. I also would like to express my appreciation to past and current members of Soft Matter and Colloid groups in Bristol, namely Oliver Hughes, Samuel Hare, Samuel Finlayson, Michael Avery and Christopher Hill, who have been supportive and helpful in discussions relating to science and other matters. Next, I would like to thank a number of other postgraduate and project students involved in the projects; Charlotte Pugsley, Jamie McIvor, Tilly MyHill, Isaac Charlton, Edward Norris, Sian Fussel, Victoria Hamilton and Esther Townsend. I also thank all the staffs in School of Chemistry, University of Bristol.

My deep and heartiest gratitude to my family; dearest papa and ibu (Mr S. and Mrs R. Hashim) and my lovely siblings (Messa, Dan, Tyra and Adrianna) for their unparalleled love, constant emotional support and motivation throughout my life and study in Bristol and the preparation of this thesis. This thesis would not have been possible without these important people in my life. I thank my friends (Inda, Asyraf, Miera, Nadiah, Ismah, Izah, Andy, Hanim, Ana, Jasmine, Chris, Andrea, Jo, Amirul, Azie, Syima, and Joanne) and all housemates in the hall for their support through hard and fun times. Sincerest gratitude to my educators in Malaysia (Professor Ahmad Fauzi, Professor Hanafi, Dr Nadras, Professor Zulkifli, Professor Azura and Pak Din) for their support, advice and encouragement. Last but not least, I thank my sponsors; The Ministry of Higher Education Malaysia and University of Science Malaysia (USM). This project and thesis would not be a success without the support from them.

List of Publications

Publications during this PhD:

- F. Waggett, M. D. Shafiq and P. Bartlett, 'Failure of Debye-Hückel Screening in Low-Charge Colloidal Suspensions', *Colloids and Interfaces*, **2**, 51-59, (2018)
- M. D. Shafiq, F. Waggett, E. Norris and P. Bartlett, 'Droplet Evaporation: Colloidal Interactions Vs. Evaporation Kinetics', *Colloids and Surfaces A: Physicochemical and Engineering Aspects*, **578**, (2019).

Contents

List of Figures

List of Tables

List of Abbreviations

vDW	**v**an **d**er **W**aals
DLVO	**D**erjaguin **L**andau **O**verbeek
CSP	**C**onstant **S**urface **P**otential
CSC	**C**onstant **S**urface **C**harge
CR	**C**harge **R**egulation
PB	**P**oisson **B**oltzmann
DH	**D**ebye **H**uckel
KS	**K**irkwood **S**chumaker
PZC	**P**harge of **Z**ero **C**harge
IL	**I**onic **L**iquid
IM	**I**onic **M**onomer
BOT	**B**linking **O**ptical **T**weezers
AOT	**A**erosol **O T** surfactant
PIL	**P**oly **I**onic **L**iquid
PMMA	**P**oly **M**ethyl **M**ethacrylate
PALS	**P**hase **A**nalysis **L**ight **S**cattering
TDAT	**T**etra **D**odecyl **A**mmonium Salt

Physical Constants

Boltzmann constant, k_B	$1.3806485 \times 10^{-23} = \mathrm{J\,K^{-1}}$
Avogadro constant, N_A	$6.0221409 \times 10^{23} = \mathrm{mol^{-1}}$
Elementary charge, e	$1.6021766 \times 10^{-19} = \mathrm{C}$
Permittivity of free space, ϵ	$8.8541878 \times 10^{-12} = \mathrm{F\,m^{-1}}$
Planck's constant, h	$6.6260700 \times 10^{-34} = \mathrm{m^2\,kg\,s^{-1}}$

List of Symbols

ΔW	Work done
ΔG	Gibbs free energy
A	Surface area
γ	Surface interfacial tension
h	Separation between surfaces
ϵ_r	Relative permittivity
e	Elementary charge
k_B	Boltzmann constant
T	Absolute temperature
λ_B	Bjerrum length
q	Point of charge
U	Potential energy
r	Distance between two charges
U_B	Born energy
a_i	Ion radius
n_{agg}	Micelle aggregation number
v_m	Volume of micelle
r_s	Radius of surfactant
σ_s	Surface charge
ξ_c	Dimensionless coupling constant
γ	Surface Interfacial Tension
ζ	Zeta potential
Z	Charge
a	Particle radius
Δf	Frequency shift
λ	Laser wavelength
K	Conductivity
A_H	Hamaker constant
h	Planck constant
v_e	Mean absorption frequency
J	Ion dissociation constant
ψ	Electrostatic potential
ψ_s	Surface potential
x	Distance out of plane on x-direction
ρ_{ion}	Ion density
ρ_o	Ion density in bulk solution
ψ_∞	Potential away from the surface
ψ	Electrostatic potential
κ^{-1}	Debye length
λ_s	Screening length
ϕ	Volume fraction

M	Neutral micelle
M^{+-}	Charged micelle
F_{drag}	Drag force
E	Electric field
S_{cell}	Entropy of a cell
$\prod$	Osmotic pressure
μ_{GC}	Gouy-Chapman length
χ	Electrostatic coupling parameter
α	Ion dissociation constant
k	Ion pair equilibrium constant
k_s	Coefficient rate of particle aggregation
ϵ_t	True dielectric constant
ϵ	Dielectric constant
ρ	Density
ρ_{ring}	Density of particle at the edge
n^*	Critical salt concentration
Λ	Molar conductivity
A_d	Droplet area
$H(t)$	Droplet height changes with time
$R(t)$	Droplet radius changes with time
$\rho(r,d)$	Density of particle at local radial distance
I_i	Intensity of particle
D	Diffusivity
P_v	Vapour Pressure
P	Pressure
v	Volume
η	Viscosity
$J(r,t)$	Evaporation flux
θ	Contact angle
Bo	Bond number
Re	Reynolds number
Pe	Peclet number
τ_{mix}	Diffusional mixing time
k_{cl}	Contact line friction coefficient
k_{ev}	Evaporation coefficient
ξ_{cl}	Contact line friction
ξ_{hydro}	Hydrodynamic friction
F	Force
α_D	Thermal Diffusivity
α_a	Thermal Expansion

Chapter 1

Introduction

This chapter introduces the concept of colloids and discusses their use in industrial applications. Then a detailed and focused comparison with the literature and discussions are made on the systems used in this thesis, which is the non-aqueous colloidal system. The models and boundary conditions discussed in this chapter are the underlying fundamentals which will be further elaborated in the result chapters, depending on the response from experimental findings and analysis.

1.1 Colloids and Soft Matter

Colloid is a well-known term among scientists across many area of the biological and physical sciences but they are also key to many everyday activities. Simple daily routines such as washing clothes or dishes, preparing hot milk to compliment a cup of hot latte and applying facial product every day are examples of the use of colloids in everyday humans' life. If we take a look at a much smaller scale, we may start pondering that colloidal-based products do not remain as they were when applied with external mechanical or thermal forces act on the system. For example, when we boil a cup of milk, a layer of protein forms on the liquid surface due to the coagulation of casein micelles, leaving other elements such as water and fat in the bulk solution (Singh, 2004). From this, we get the idea of what is exactly a colloidal substance. Colloidal-based products visually appear as homogenous mixtures but they are heterogeneous microscopically.

Colloid is a broad term of a mixture containing two or more phases in one system. One phase is known as the matrix or dispersed phase while the other one is referred to as the dispersion medium (continuous phase). Numerous types of colloidal systems including aerosol; consist of fine solid or liquid particles suspended in air, an emulsion; a system containing two miscible liquids, a suspension; a term when solid particles dispersed in a liquid, and foam; trapped gaseous particles in liquid or solid. Familiar examples of colloids are fog, smoke and mist (consisting of

liquid or solid droplets in air); milk (an emulsion); blood, paint, mud and slurries (typical examples of suspension).

Colloidal science has great importance in numerous industrial applications including medical and food products, water purification, soaps and beauty products, rubber-based products and applications which require aesthetic values such as coating, painting, layering and printing. Inkjet printing is an emerging technique, especially as an alternative for the electroplating and etching processes in printing circuit boards (PCB) industry.

1.2 Colloidal Suspension: Non-Polar System

1.2.1 The stability of colloids in non-polar solvent

The term 'colloidal suspension' refers to a heterogeneous mixture consisting large particles (up to 1 μm or 1000 nm) in a dispersed liquid phase. This thesis is focused on the behaviour of a colloidal suspension with particles of approximately 1.55 μm. Optically, these colloidal particles appear to be stable throughout the bulk liquid in a suspension. The destabilisation of the colloid is mainly controlled by the physical and interfacial properties of both dispersing material and medium (Chanamai and McClements, 2000). Gravitational forces may destabilize the dispersion; if the solid particles are less dense than the dispersing solvent, the particles tend to float on the surface. The flotation of these particles is referred to as creaming. A simple example of colloidal creaming was observed by Hancock in 1824 and Faraday in 1825, where the creaming or flotation of rubber latex particles in water (the density of polyisoprene particles is 0.92 g/mL) and a stable dispersion could be achieved by incorporating hydrophilic colloids such as gums, pectins and gelatins. Meanwhile, sedimentation (sometimes referred to as 'downward creaming') occurred when the density of the colloid is higher than of the dispersing medium (Hauser and Dewey Jr., 1941; Bondy, 1939). This phenomenon is not only observed in natural rubber latex emulsion, but also in milk and mineral suspensions. However, flotation and sedimentation are prone to occur in lyophobic colloids, in which the dispersed phase is not solvated by the dispersing media. In our work, we used lyophilic colloids; where the colloids are solvated and characterized by a strong affinity to the dispersing medium. The dispersion of the suspension is achieved spontaneously without mechanical agitation and the dispersed colloidal particles have no tendency to coalesce or aggregate.

Now, imagine one single particle suspended in a liquid, the particle moves with a velocity in the surrounding fluid with no preferential direction. In reality, a colloidal system contains many particles and these particles move randomly in the

fluid and subsequently collide each other. The movement is called Brownian motion as observed by Robert Brown in 1827 when he studied the movement of pollen grain in water. The collisions between particles may result in destabilization of the colloids. The stabilization of colloidal particles suspended in a fluid can be achieved by controlling the interparticle interactions mainly by manipulating the electrostatic properties of the colloids (charge stabilization) and incorporating a polymeric stabilizer on the surface of the colloids, which is normally referred as steric stabilization (Everett, 2007).

In fluids, colloidal particles will naturally ionize surface groups and generate surface charge, especially when dispersed in a polar solvent. Charge stabilization of colloids is achieved simply based on Coulomb's law where similarly-charged bodies repel each other while oppositely-charged entities form attractions (Everett, 2007). The stability of colloidal suspensions due to electrostatic interactions, which is the fundamental study of this thesis, can be described by Deruaguin, Landau, Verwey and Overbeek (DLVO) theory. DLVO theory combines the effect of van der Waals (vdW) attraction and electrostatic repulsion between two interacting charged colloids. We will discuss further the background of this theory in a later part of this chapter. Before understanding the basis of interactions of two colloidal spheres, it is crucial to introduce the concept of free energy.

In a system that consists of bodies which are not at their equilibrium state, their free energy is at a high value. At this high free energy state, their stability is controlled by the balance of interactions (attraction and repulsion), and an infinitesimal perturbation will favour the colloids to be arranged at their lower free energy state and this will induce an instability in the system, thus forming aggregations or coagulation. The amount of perturbation or work done to initiate the instability must exceed the free energy of activation (Everett, 2007; Israelachvili, 2011; Hogg, Healy, and Fuerstenau, 1966). At this stage, the system is metastable, in which the energy required for the process to occur is provided as kinetic energy rather than thermodynamic control. In order to maintain the stability of the colloidal dispersion, the surface area of the colloid must be sufficiently large as the interactions form on the surface between colloid-colloid and colloid-solvent. This interface affects the free energy of the system; the amount of work done ΔW to counter the attraction between the surfaces must be sufficiently large and it is equal to the increase in Gibbs free energy ΔG,

$$\Delta W = \Delta G = 2A\gamma_s \tag{1.1}$$

where A is the surface area and γ is the interfacial surface tension. When the separation between two surfaces, h becomes infinitely large, the Gibbs free energy is directly proportional to $2A$. To compliment the factor affecting the energy

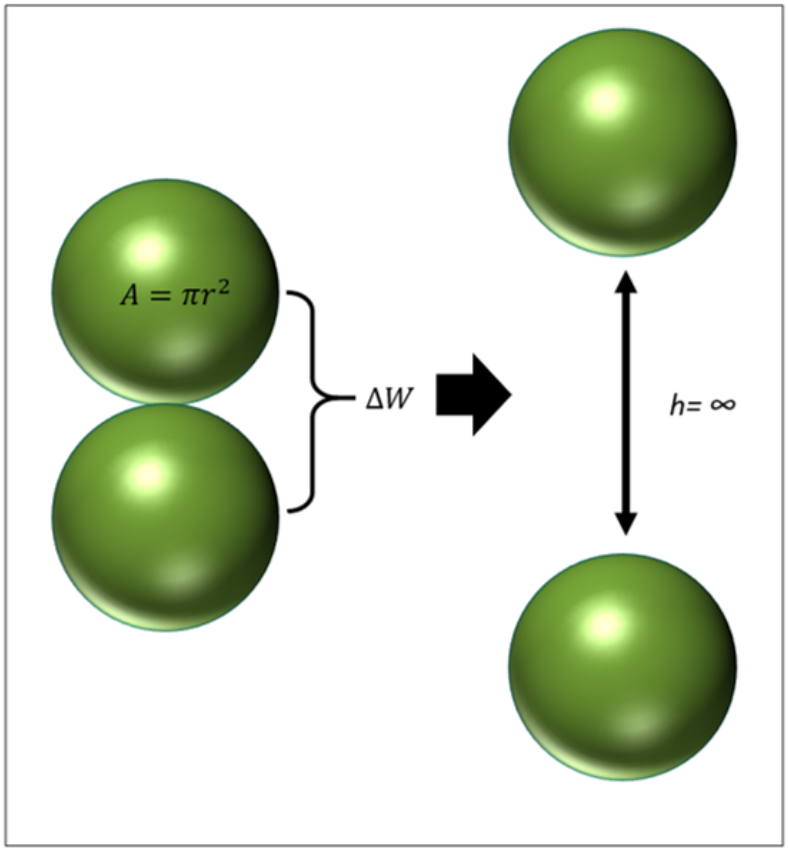

FIGURE 1.1: Illustration of the dependence of Gibbs free energy on the separation between colloids

barrier and the stability of the colloidal system, we will discuss the effect on the interparticle interactions in the colloidal dispersion later in this chapter. In the next subchapter, we will introduce the key parameter affecting the interaction of colloids and how the charge is generated in non-polar colloidal systems.

1.2.2 Non-polar Systems

The polarity of a solvent has a great influence in determining the stability of colloids in a liquid medium. Non-polar solvents are chemically referred to solvents which contain bonds with similar electronegativities, where the electrons are shared equally between the atoms in the molecules. Familiar examples of non-polar solvents are hydrocarbons (alkanes) and gasoline. On the other hand, a polar solvent contains atoms with a large difference in electronegativities and one simple example is water. Relative permittivity ϵ_r is a dimensionless measure of the strength of electrical energy stored in a substance (or solvent) when an electric field is applied and it is a common measure to compare the polarity of different solvents.

Table 1.1 compares the relative permittivity of several non-aqueous solvents and water at room temperature and pressure. Fundamentally the electrical

Solvent	**Relative Permittivity,** ϵ_r
Hexane	1.89
Dodecane	2.03
Cyclohexyl Bromide (CHB)	7.92
Tetrachloroethane (TCE)	8.42
Water	80

TABLE 1.1: Relative permittivity of selective solvents at T= 298 K and P= 1 atm.

phenomena in non-polar solvents such as dodecane and hexane, which are widely discussed in this thesis, behave similarly as in water but the range of interactions and the origin of electrical charges can be distinctly dissimilar. In the next subchapter, we will discuss methods to effectively increase the electrical charge of colloids in a non-polar solvent. When we have two or more (significantly) charged bodies in a dielectric solvent, the strength of interactions between these ion pair can be quantified using the characteristic length scale, known as the Bjerrum length λ_B

$$\lambda_B = \frac{e^2}{4\pi\epsilon_r\epsilon_o k_B T} \tag{1.2}$$

where e is the elementary charge, ϵ_r is the relative permittivity of the solvent, ϵ_o is the vacuum permittivity, k_B is the Boltzmann constant and T is temperature. If we take the values of relative permittivity in Table 1.1, the Bjerrum lengths in water and dodecane are 0.7 nm and 28 nm respectively. This means that ion pairs in dodecane are interacting at a much shorter range compared to in water. The Bjerrum length measures the ratio between the energy (attractive or repulsive) that drives the point of charges to a certain configuration to the randomizing effects of the thermal energy ($k_B T$).

It is obvious that the relative permittivity or dielectric constant of a solvent has an effect on the Bjerrum length. To make the explanation concise, let us take a look at water molecules; these consist of dipolar atoms of hydrogen and oxygen. When we have charged bodies in water, the interactions between these bodies are influenced by the charge ends (negative or positive pole) of the water molecules, making the net interaction between the point of charges perturbed. This will result in less probability for these ions to interact and combine to form ion pairs. Referring to the correlation of potential energy U with r is the distance between two charges and relative permittivity in equation 2, the interaction energy of point charges q_1 and q_2 is 40 times weaker in water than in dodecane, making charging is very likely to

occur in water. At a larger Bjerrum length scale (>10), the fluctuation due to thermal energy dominates the system, where the ion-ion coulombic interaction (Gouy-Chapman length) becomes less ideal and mean-field theory steps into the picture. Next, we will explain the methods on how to effectively induce charging of colloids in a non-polar system.

$$U(r) = \frac{q_1 q_2}{4\pi\epsilon_o\epsilon_r r} \tag{1.3}$$

1.3 The origin of charging in non-aqueous system

The degree of ion solvation measures how susceptible a colloid is to get charged by the solvent molecules and the solvation is enhanced by the polarity of the dissolving solvent. In non-polar solvents, charging of colloids seems impossible due to lack of polar ends of the solvent. The solvation energy can be described by the Born model and the Born energy U_B to solvate an ion with ion radius a_i can be expressed as,

$$U_B = \frac{e^2}{8\epsilon_r\epsilon_o a_i} \tag{1.4}$$

From equation 1.4, we can understand that a system with low dielectric solvent requires a substantial amount of energy to solvate an ion (vice versa) and U_B can be manipulated by altering the radius of the ion a_i. Rashin and coworkers reported on the dependence of the ionic radius on the enthalpy of ion solvation in water and found out that it is reciprocal (Rashin and Honig, 1985). From this, we expect that generating a charge in a non-polar system can be a challenge considering the system is pure, containing no free or excess ions. Moreover, to generate charge, we are not relying on the unknown trace impurities, but there are a number of methods which can be used to generate charge in the non-aqueous system.

1.3.1 Ionic Surfactants

Before we discuss the effect of charging induced by surfactant, let us briefly summarise what is a surfactant. Abbreviated from 'surface active agent', a surfactant is not a new topic in interfacial science and the study of surfactant has been established a number of decades ago. Surfactants are widely used to serve industries mainly in

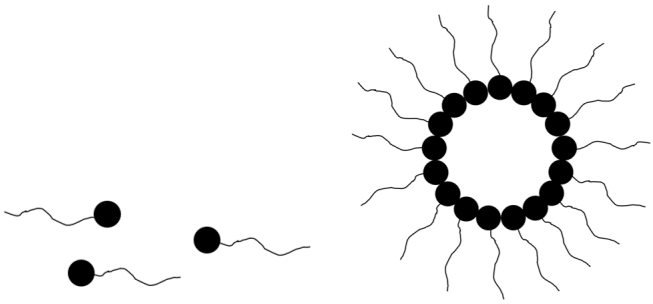

(A) Surfactant molecule below CMC (B) Reverse micelle formed above CMC

FIGURE 1.2: Schematic of individual surfactant molecule and reverse micelle formed in non-aqueous solvent

the production of detergents, soaps, dispersants and foam-based products. A surfactant is an amphiphile, which is a molecule that consists of two functional parts; the polar head and long chain (mostly) hydrocarbon tail. Each part is soluble in different polarity solvent, for instance, the long hydrocarbon tail dissolves in non-polar fluid (hydrophobic) and the polar head is soluble in a polar solvent such as water (hydrophilic) (Smith et al., 2013; Rana et al., 2017). Types of surfactants including ionic (cationic and anionic), non-ionic and zwitterionic, but in this thesis, we focus on ionic surfactanst (anionic), just to develop charging of colloids in a non-aqueous system. Most studies using surfactants are anchored on the effect of surfactant on the surface properties of the system such as contact angle and structural organization, but in our study, the effect of surfactant on the surface charge and the charging mechanisms are quantified and observed, as thoroughly discussed in Chapter 5.

The unique physicochemical properties of surfactants are that they form micelles in the fluid above a threshold concentration known as the critical micelle concentration (CMC) due to their amphiphilicity. Below CMC, the surfactant exists as individual molecules or monomers (Paria and Khilar, 2004). In water, the micelles formed with the polar heads extending in the bulk with the long chain tail aggregating at the centre of the micelle. This briefly explains the simple mechanism of washing clothes, where the polar head extends in the bulk water and the inert tail entraps dirt and oils at the centre. However, in a non-polar fluid, reverse micelles formed; the hydrocarbon tail extending freely in the bulk liquid and the polar head aggregating in the middle as illustrated in Figure 1.2. The polar head aggregating in the middle forms a core that is capable of storing an ion and the size of micelles formed depends on the radius of the ion trapped in the micelle core.

In this thesis, we use an anionic surfactant known as sodium dioctyl sulfosuccinate (AOT) as the molecular structure illustrated in Figure 1.3. Figure 1.4 shows the structure of AOT monomers form reverse micelle in tetrachloromethane (ϵ_r = 2.23) with anionic heads entrapping tracable water content at the micelle core with the micelle diameter of 3.5 nm (Deàk et al., 2004; Zakerhamidi et al., 2010). In

a non-polar system, the aggregation number and CMC are typically lower than the water-based system. Surfactant aggregation number n_{agg} is the average number of surfactant molecules per aggregate in a micelles and for spherical micelle, the number can be calculated using the expression,

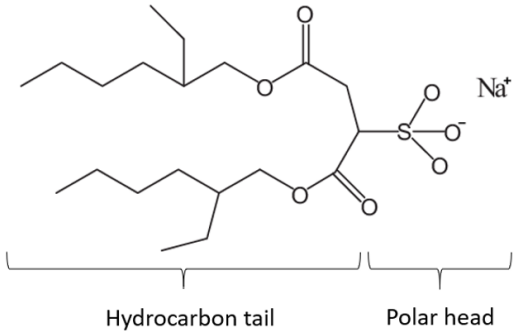

FIGURE 1.3: Molecular structure of AOT surfactant

$$n_{agg} = \frac{4\pi r_s^3}{3v_m} \tag{1.5}$$

where r_s is the surfactant radius and v_m is the volume of the micelle. Smith et al. reported that the n_{agg} and CMC of AOT in cyclohexane (ϵ_r = 2.3) are 23 at 0.21 mmol/kg and about 0.13 $\pm$ 0.08 mmol/kg respectively (Smith et al., 2013). The transition from the existence of individual surfactant molecules to the formation of micelles occurs much more gradually in a hydrocarbon solvent (CMC of AOT in water = 2.56 mmol/kg) due to lack of polar groups in the solvent. However, the tendency of the aggregation to form micelles is driven by the discrepancy of polarity between AOT head group and hydrocarbon solvent (Smith et al., 2013; Gorski and Ostanevich, 1990). The magnitude of charge generated is reported to be dependent on the micelle size. However, previous studies found that the magnitude of charge stabilization in non-aqueous solvents is influenced by the size of the polar head of the formed micelles, which can be altered through synthesizing the surfactant molecules. Parent et al. incorporated more polyamines group in the surfactant head and found out both micelle radius and overall charge magnitude was enhanced in a non-polar system (Parent et al., 2011).

The study of charging phenomena in non-aqueous systems has been established over a decade ago and yet there is still no definite concluding line drawn to identify the mechanism of charging in non-aqueous solvents via the addition of ionic surfactant. However, there are a number of techniques used to justify the phenomena of charge stabilization of non-polar colloids. Conductivity is a traditional and useful technique to identify the CMC of surfactant and also the magnitude of

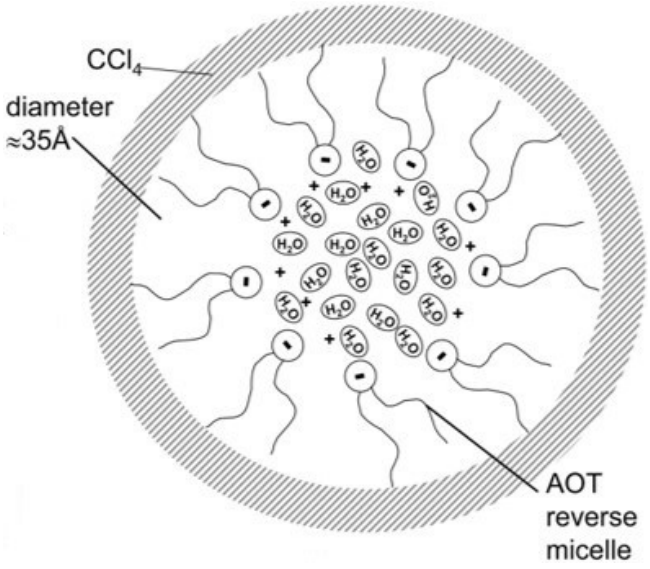

FIGURE 1.4: Reverse AOT micelle in tetrachloromethane with tracable water content in the micelle core (Deàk et al., 2004)

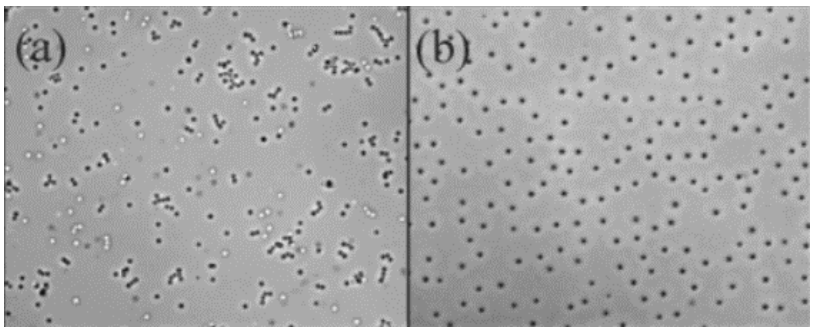

FIGURE 1.5: Optical micrograph of PMMA colloids in dodecane; (a) without AOT, and (b) with 12mM of AOT (Hsu, Dufresne, and Weitz, 2005a)

charging of a non-polar colloidal system. The conductivity of the system will normally increase with surfactant concentration and beyond the CMC region, the conductivity is dominated by the amount of charged micelles formed in the solution via charge disproportionation. It is a process where two electrically neutral micelles undergo a charge exchange process, yielding a pair of oppositely charged micelles. Hsu et al. exhibited a relevant work where AOT was used to enhance the electrostatic charging of PMMA colloids in a non-aqueous solvent. As presented in Figure 1.5, the PMMA colloids were electrostatically stabilized when reverse AOT micelles were added into the system and the observation is in a good agreement with the surface charge magnitude from electrokinetic and conductivity measurements (Hsu, Dufresne, and Weitz, 2005a). In Chapter 6, we will discuss the possible mechanism outlined for our AOT system in dodecane and hexane (Guo, Singh, and Behrens, 2009; Guo et al., 2013).

1.3.2 Polymerizable Ionic Liquid

Another common technique to develop surface charge is by synthesizing a polymerized ionic liquid (PIL). PIL is a polymeric compound that consists of ionic species anchored at monomer repeating unit, channelled through the main backbone. The polymerization of PIL normally performed via free radical reaction by linking the polymerizable site of the main polymer with cationic or anionic parts of the ionic liquid. PILs possess numerous advantages including the enhanced stability of carbon nanotubes and graphenes and also improved performance such as durability and flexibility of final products depending on applications (Kadokawa, 2013). Due to its ability to perform as conductive materials, PILs have the potential to be used as an electrolyte in batteries and fuel cells (Ohno, Yoshizawa, and Ogihara, 2004). In this project, we used PILs synthesized by a former member in our group, Mr Ghulam Hussein to generate charging in low-polarity solvents (Hussain, Robinson, and Bartlett, 2013). The synthesis route to polymerize PIL will be discussed in Chapter 2. PIL is referred to as IM-PMMA in this thesis. As discussed earlier in non-polar solvents ($\epsilon_r \sim 2$ in our case), the dissociation of charge is impossible or less probable compared to water.

When a colloidal particle containing ionizable groups on its surface is immersed in a low-polarity solvent, the ionizable surface group will dissociate, generating charges with an opposite sign of the surface charge (counterions). The surface of the colloid generated a net charge and the charge density is assumed to be uniform across the surface (Hussain, Robinson, and Bartlett, 2013; Valeriani et al., 2010). The distribution of ion and surface potential of PIL systems can be described using the Poisson-Boltzmann (PB) theory (Hussain, Robinson, and Bartlett, 2013). We will discuss PB theory in Chapter 1.5. For monovalent ions, the Poisson-Boltzmann theory can be considered when the dimensionless coupling constant $\xi_c = 2\pi\sigma_s\lambda_B^2 < 1$, where σ_s is the surface charge density. Our system with the particle radius at about 1 μm in low polar solvent (λ_B = 28 nm), the coupling constant $\sim$ 0.3.

Particle	a **/nm**	**Solvent**	ϵ_r	Z **/e**
PMMA	755	Dodecane	2.03	140
IM-PMMA	1265	Hexane	1.89	500
Titania (Holmberg et al., 2013)	30	Water	80	4000

TABLE 1.2: Comparison of colloidal systems in different solvent with varied magnitude of surface charge (measured from electrophoretic mobility in this thesis)

PILs have evidently developed the surface charge and potential of the particles and the magnitude of the effective charge is briefly compared in Table 1.2. We will also report the effect of IM-PMMA on the deposition pattern of an evaporating

colloidal system in Chapter 6.

1.4 Electrophoretic Mobility of Charged Colloids

For the relevance of sections 1.4 and 1.5, we start the discussion with the fundamental concept of the electric double layer (EDL), which will be continuously discussed in Chapter 1.5.

1.4.1 Electric Double Layer

Previously in this chapter, we introduced the significance of charge in a colloidal system and how charge can be enhanced or generated in non-aqueous systems. The distribution of ions on a charged surface has an important deal on the charged-stabilized colloidal system and significantly affects the electrokinetics properties of the system. Counter- and coions present in a bulk electrolytic solution are referred to as free ions. The distribution of free ions in the solution depends on the overall net charge (magnitude and sign) and electrostatic potential of the surface and subsequently affect the electrical double layer (EDL) (Everett, 2007; Masliyah and Bhattacharjee, 2006). From this, we can simply define the EDL as the atmosphere where ions are distributed on the surface or between two surfaces in a solution (Everett, 2007). In the 1850s, Helmholtz was the first to speculate on the arrangement of ions between two flat surfaces immersed in an electrolytic solution. The surface must hold a net charge and the interaction is electrostatic in nature. At the plate-solution interface, to achieve the equilibrium or electroneutrality, the counterions must be redistributed on the surface.

A layer of counterions is firmly bound on the charged surface and surrounding this layer, the vicinity where ions (counterions and coions) are mobile and more diffuse, and these layers of ions are normally referred as the double layer. These ions are interacting; oppositely-charged ions will attract each other and like-charged ions will repel, which result in the non-uniformity of the ion distribution. The arrangement and interactions between counterions and coions in the double layer have a large dependency on the surface charge, concentration of salt, electrolyte and any ion-dissociating species added into the system (Lyklema, 2005; Masliyah and Bhattacharjee, 2006). However, the Helmholtz model does not consider the thermodynamic and kinetic effects arising from the mobility of an ion in solution vicinity. Gouy in the 1910s developed a model by indicating the counterions are not rigidly held on the charged surface, instead, they tend to diffuse in the solution, making the entropy of system increase until the electrostatic attraction triggers the ions to be near on the charged surface. In other words, the arrangement of counterions on

the surface is dominated by the competition of electrostatic interaction and entropy and this affects the thickness of the entire double layer (Oldham, 2008; Schellman and Stigter, 1977). Gouy and Chapman then developed the model to estimate the ion distribution near the charged surface based on the Boltzmann distribution and the electrostatic potential with regards to the ion distribution in a dielectric medium can be expressed by Poisson's equation, as discussed in Chapter 1.5. The Gouy-Chapman model of EDL, however, is limited for a system with low-charged colloids as for our system.

1.4.2 Electrophoresis

Electrophoresis is an electrokinetic phenomenon where relative motion between two charged surfaces occurs in liquid (Masliyah and Bhattacharjee, 2006). Under the influence of an external electric field, the charged surface has the tendency to move in its preferred direction and the diffuse ions in the double layer tend to migrate in the opposite direction and the velocity causes a movement of the solvent. Nicholson and Carlisle in 1800 were the first to attempt an experiment on the electrokinetic phenomena, where they modified the decomposition of water by an electric current (Horwitz, 1939). Not long after, Reuss used quartz particles at the bottom of the U-tube containing water and discovered the water level at one arm (negative electrode) of the tube rose by about nine inches. This phenomenon is called as an electroosmosis; a type of electrokinetic phenomena distinct from electrophoresis, streaming potential and sedimentation potential, where the quartz powder acted as a so-called 'diaphragm' with small capillaries. Reuss then added a block of clay covered with sand into the water in tubes with applied electric field (Horwitz, 1939; Arulanandam and Li, 2000). He spotted that the clay particles migrated towards the positively-charged electrode, suggesting clay particles possess a negative net charge and this phenomenon is called as the electrophoresis (Horwitz, 1939; Swartzen-Allen and Matijevic, 1974). Electrophoresis is a very useful technique to separate the mixture of charged colloidal particles and macromolecules such as proteins (Masliyah and Bhattacharjee, 2006).

In electrophoresis, the relation between the potential and the number of charges is described by the Poisson equation and greatly influenced by the applied electrical potential, the diffusion force of the system and the bulk movement of charge, which is affected by the flow properties of the fluid. The solid surface is always pictured as a sphere, cylinder or a large flat plate while the liquid is assumed to be a Newtonian fluid, where the viscosity is independent of the shear rate. In addition, turbulence and non-linear flow effects are neglected (Vold, 1982). This brings us to the most important characteristic in electrophoresis, which is known as the surface of shear (Masliyah and Bhattacharjee, 2006). The surface of the shear or slipping plane is illustrated as a plane that lies within the stationary fluid vicinity, close

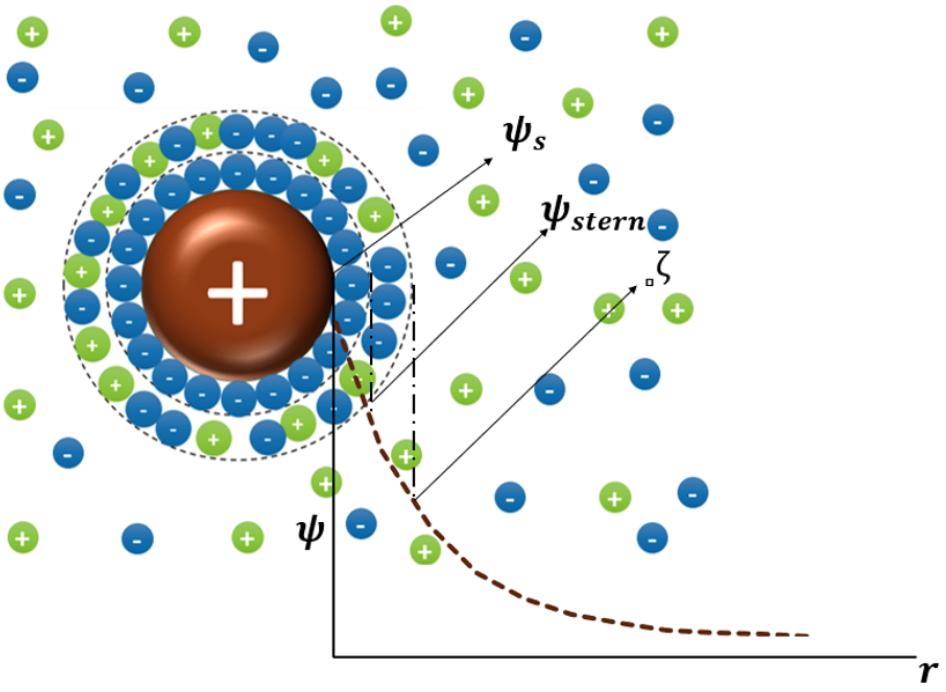

FIGURE 1.6: Potential difference with respect to distance from the charged surface

to the charged solid surface, just over the counterion layer. The particle and any ions within the shear plane are considered as a kinetic unit, which means under an influence of electric field, the particle will migrate carrying the plane and the effective charge is composed of the surface charge and the number of ions in this vicinity. The electrophoretic mobility is a measure of velocity under the applied electric field and it gives a measure of the net charge of the particle (Masliyah and Bhattacharjee, 2006; Stigter and Mysels, 1955). For non-aqueous systems, where the double layer thickness is assumed to be large, the mobility measurement is outlined by the H*ü*ckel approximation. The calculation of average potential at the shear plane can be performed by measuring the zeta potential ζ and can be expressed as:

$$\zeta = \frac{Ze}{4\pi\epsilon_r a} \tag{1.6}$$

where Z is the surface charge of the particle. Zeta potential is vital in determining the interaction energy between colloidal particles, and the stability of the dispersion (Li, 2004). It can be measured using the phase analysis light scattering (PALS) technique via electrophoretic mobility.

Briefly, PALS is measured using similar methods to laser Doppler electrophoresis. The method measures the frequency shift in the scattered light triggered by the movement of the particles under the influence of an electric field. The frequency shift Δf can be calculated using:

$$\Delta f = 2v\sin(\frac{\theta}{2}/\lambda) \tag{1.7}$$

where v is the particle velocity, θ is the scattering angle and λ is the laser wavelength. In PALS, the phase shift is measured, which is more accurate for low mobility (low charge), non-aqueous and viscous solvents (Miller, Schätzel, and Vincent, 1991). PALS was extensively used to measure the electrophoretic mobility for the work presented in this thesis.

1.4.3 Conductivity of Colloidal System

Conductivity K is an important measure to signify a system or material carries a substantial amount of free ions. Generally, conductivity can be defined as the ability of a system to convey electrical charge and it is reciprocal to the electric resistivity. The migration of ions and particles under an applied electric field in a colloidal suspension generate an electric current in the system. The conductivity of non-polar systems can be extremely small, because colloids in a non-polar solvent can hardly generate charges. As mentioned in Chapter 1.3, there are a number of charge-inducing agents which can be added to alter the electrostatics in a non-aqueous system and this has a large influence on the conductivity of non-polar fluids.

Measurement of conductivity has been widely used to estimate the micellisation of surfactants both in water and non-aqueous system. The increase of conductivity is expected when the concentration of ionic surfactant added into the solvent increased as the charged surfactant molecules move freely in the solution. Then when micelles formed and CMC of the system is achieved, the conductivity value increases at a lower gradient. The transition between these two gradients marks the value of CMC of the surfactant solution (Shanks and Franses, 1992; Pérez-Rodríguez et al., 1998). Shanks and coworker developed an accurate conductivity model to estimate the interionic interaction for a water-based micellar system, where the model used the Stokes-Einstein expression to explain the ion mobility (Shanks and Franses, 1992). From this, we know that the conductivity can be used to investigate the ion density in a colloidal system and how it affects the double layer and Debye length of charged colloids. In Chapter 5, we will discuss the effect of the conductivity of

AOT-laden colloidal system in dodecane on the number of charged species present in the system and most importantly, the Debye length.

1.5 Electrostatics of Colloids

As discussed in section 1.21, colloids in a dispersion possess a much higher free energy than the bulk thus the spontaneity to organize to a lower free energy state is high. A substantial amount of energy, known as the energy barrier is required to prevent the destabilisation of the colloidal dispersion. The paramount issue is that the stabilization of the colloids is governed by the conditions where the energy barrier is modified. The energy required to navigate the colloids over the energy barrier is driven by Brownian motion, resulting in random collisions between particles and the average translation energy of each particle is of the order of $\frac{3}{4}k_BT$, where k_B is the Boltzmann constant and T is absolute temperature. At room temperature, each particle possesses an energy of the order of 10^{-20} J due to Brownian motion. Provided that the free energy barrier is sufficiently high in relative with thermal energy k_BT, the colloids exist as a dispersion indefinitely (Everett, 2007; Lyklema, 2005). Interparticle interactions are the most vital measure of controlling the stability of colloidal dispersion. Colloidal stability is tunable by altering the strength of electrostatic repulsion and van der Waals (vdW) attraction between charged colloids as outlined by DLVO theory. DLVO indicates the potential energy between two interacting particles is the summation of attractive (U_A) and repulsive (U_R) energies and can be expressed as:

$$U_{DLVO} = U_A + U_R \tag{1.8}$$

1.5.1 DLVO: van der Waals Attraction

The van der Waals (vdW) force is possessed by all molecules without permanent dipoles and at the intermolecular level, the vdW potential energy can be expressed by (Israelachvili, 2011; Mitchell and Ninham, 1972),

$$U_A = -\frac{C}{R^6} \tag{1.9}$$

Meanwhile, for two interacting similar-sized microspheres, the attraction potential can be presented as,

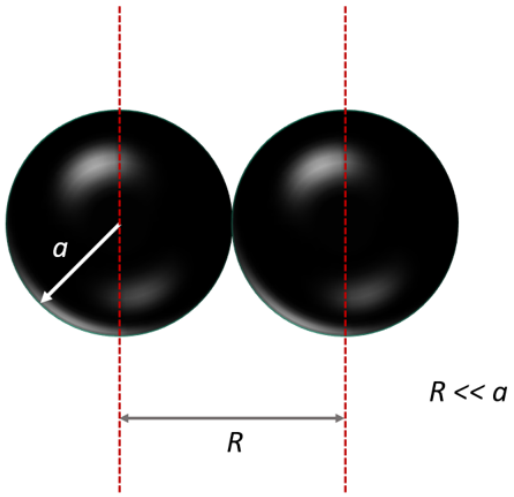

FIGURE 1.7: Presentation of two similar-sized microspheres

$$U_A = -\frac{aA_H}{12H} = -\frac{aA_H}{12(R-a)} \tag{1.10}$$

with $R \ll a$ and A_H is the Hamaker constant, H is the distance between interacting surfaces and R is the centre-to-centre separation between two spheres. Comparing the relation of the attractive potential in equation 1.8 ($U \propto R^{-6}$) and equation 1.10 ($U \propto (R-2a)^{-1}$), it shows that the potential between two microspheres falls much more slowly than the potential between two molecules or atom; reduction in a magnitude of potential energy occurs when two spheres are one magnitude apart while two molecules are six orders of magnitude apart) (Israelachvili, 2011; Mitchell and Ninham, 1972; Love, 1977).

For many bodies interacting in a medium, the Lifshitz approach of van der Waals forces is implied, where the atomic structure is ignored and the forces between large bodies are considered as continuous media; that is the Hamaker constant is derived by taking the bulk properties such as dielectric constant and refractive index into account. The approach was introduced by Evgeny Mikhailovich Lifshitz in 1954 as the consideration of the summation of total intermolecular forces cannot be simply summed up through pairwise additivity especially in a condensed system. The Hamaker constant A for a symmetric case now can be calculated using the expression (Israelachvili, 2011; Visser, 1972),

$$A_H = \frac{3}{4}k_BT\left(\frac{\epsilon_r^1 - \epsilon_r^2}{\epsilon_r^1 + \epsilon_r^2}\right)^2 + \frac{3h\nu_e}{16\sqrt{2}}\frac{(n_1^2 - n_2^2)^2}{(n_1^2 + n_2^2)^{3/2}} \tag{1.11}$$

where ϵ_r^1 is the dielectric constant of the colloidal particles, ϵ_r^2 is the dielectric constant of the dispersing medium, h is the Planck constant and ν_e is the mean electronic absorption frequency. The first term denoted the zero-frequency van der

Waals energy such as the Keesom and dipolar forces and the second term contributes the dispersion energy such as London dispersion forces. We calculate the Hamaker for our system; PMMA particles in dodecane with $v_e = 3 \times 10^{15}\ s^{-1}$, ϵ_r for PMMA and dodecane is 4.9 and 2.03 respectively, then we get $A_H = 1.8 \times 10^{-21}$ for our system. We calculate the attractive potential at T=300K using equation 1.10 with radius of PMMA of 755 nm, so the separation between two spheres must be less than 755nm, we get $U_A = 3 \times 10^{-22}$J. This proves that $U_A \ll 0.1\ k_BT$. The zero-frequency van der Waals energy in the first term of equation 1.11 is less than $\frac{3}{4}k_B$T, suggesting the interaction is purely entropic rather than coloumbic (Israelachvili, 2011).

1.5.2 DLVO: Electrostatic Repulsion

The distribution of electrostatic potential ψ for one-dimensional problem and ion density ρ_{ion}, based on the Gouy-Chapman analysis due to the presence of a flat charged surface in a dielectric fluid can be related by the Poisson equation with x the normal distance out of the charged surface (Masliyah and Bhattacharjee, 2006; Everett, 2007),

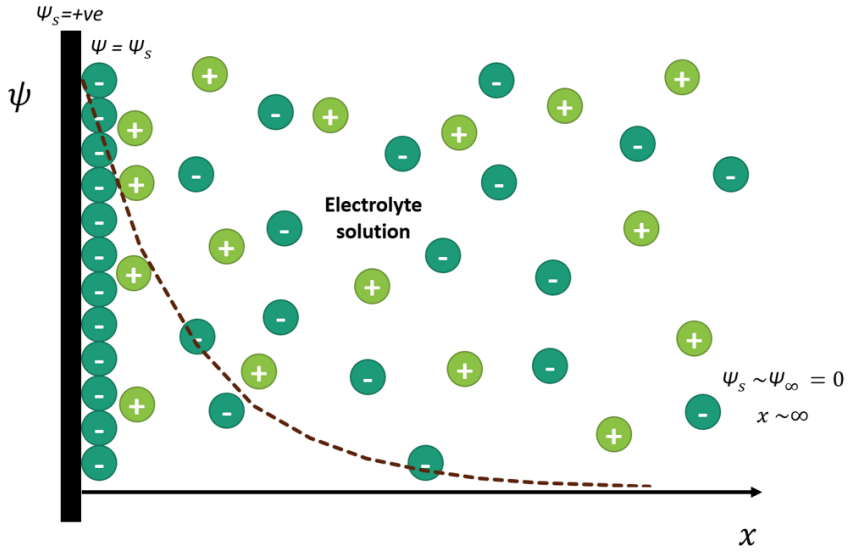

FIGURE 1.8: Representation of electrical double layer with distribution of ions and electrostatic potential ψ decaying with distance from the charged surface x

$$\frac{\delta^2\psi}{\delta x^2} = -\frac{\rho_{ion}}{\epsilon_o\epsilon_r} \tag{1.12}$$

The distribution of ions near the charged surface region is governed by the temperature of the system and energy $W = ze\psi$, required to bring the ion from a

distance away from the surfaces ($\psi = \psi_\infty = 0$) to the region where the electrostatic potential is equal to surface potential ψ_s provided by the Boltzmann equation (Israelachvili, 2011),

$$\rho \propto \exp(-\frac{W}{k_B T}) \tag{1.13}$$

$$\rho_{ion} = \rho_o \exp(-\frac{ze\psi}{k_B T}) \tag{1.14}$$

where ρ_o is the ion density in the bulk and z is the ion valency. Combining equations 1.12 and 1.14 yields the Poisson-Boltzmann equation,

$$\frac{\delta^2\psi}{\delta x^2} = -\frac{\rho_o}{\epsilon_o \epsilon_r} \exp(-\frac{ze\psi}{k_B T}) \tag{1.15}$$

We consider the electrolyte is a single dissociating species; the ions are monovalent (consist of single cation and anion, $z = z+ = z-$), the equation can be rewritten as,

$$\frac{\delta^2\psi}{\delta x^2} = -\frac{\rho_o}{\epsilon_o \epsilon_r} [\exp(-\frac{ze\psi}{k_B T} - \exp(\frac{ze\psi}{k_B T})] \tag{1.16}$$

or

$$\frac{\delta^2\psi}{\delta x^2} = 2\frac{\rho_o e}{\epsilon_o \epsilon_r} \sinh(\frac{ze\psi}{k_B T}) \tag{1.17}$$

The dimensionless potential Ψ can be defined as,

$$\Psi = \frac{ze\psi}{k_B T} \tag{1.18}$$

So, equation 1.17 can be rewritten as,

$$\frac{\delta^2\psi}{\delta x^2} = 2\frac{\rho_o e}{\epsilon_o \epsilon_r}\sinh(\Psi) \tag{1.19}$$

If the potential is sufficiently small where $\Psi \ll 1$ ($k_B T \gg ze\psi$), equation 1.19 can be linearised to,

$$\sinh(\Psi) \approx \Psi \tag{1.20}$$

and this yields,

$$\frac{\delta^2\psi}{\delta x^2} = \frac{2\rho_o e}{\epsilon_o \epsilon_r}(\Psi) \tag{1.21}$$

For a solution with a dilute 1:1 electrolyte, the Debye length, κ^{-1} from the Debye-H*ü*ckel approximation measures the thickness of the electric double layer and a characteristic length scale from a charged surface to a point where the electrostatic potential decaying from the true surface potential. In other chapters of the thesis, the Debye length is often referred as the screening length λ_s The Debye length can be expressed as:

$$\kappa^{-1} = \sqrt{\frac{\epsilon_r \epsilon_o k_B T}{2\rho_o e^2}} \tag{1.22}$$

For a low potential system, the term $ze\psi/k_B T$ is smaller than unity and the Poisson-Boltzmann relation in equation 1.21 can be rearranged to,

$$\frac{\delta^2\psi}{\delta x^2} = \frac{2\rho_o e}{\epsilon_o \epsilon_r}(\Psi) = \kappa^2\Psi \tag{1.23}$$

The linearisation of the Poisson-Boltzmann equation is referred to as the Debye-H*ü*ckel approximation with boundary conditions of $\psi = \psi_s$ at $x = 0$ and $\psi = 0$ as $x = \infty$, given by (Masliyah and Bhattacharjee, 2006),

$$\psi = \psi_s \exp(-\kappa x) \tag{1.24}$$

Equation 1.24 justifies that the electrostatic potential decays exponentially with the separation from the charged surface. The decay of the potential depends on the valency and electrolyte concentration in the system. Higher electrolyte concentration has more tendency to screen the electric potential to a larger extent (Masliyah and Bhattacharjee, 2006; Ohshima, 2006a). The Poisson-Boltzmann relation derived earlier is applicable only for a planar surface or curved surface (spherical) at the limit where $\kappa a \ll 1$. Otherwise, the Poisson Boltzmann equation for spherical surface must be considered,

$$\psi = \psi_s \exp(-\kappa(r-a))(\frac{a}{r}) \tag{1.25}$$

In the next subchapter, we will explain the role of DLVO theory on the interactions between two colloidal spheres.

1.5.3 Interaction between Colloidal Particles and Optical Tweezers

In non-polar solvents, when the concentration of ions in solution is significantly low or negligible, two charged particles interact like two point like ions, where the size is negligible, and the colloid has no effect on the counterions or ions in the double layer. The solvent is considered as a continuum, where the dielectric constant is similar throughout (Roij, 2000; Dahirel and Jardat, 2010). This is known as the mean-field theory. Realistically, when two charged particles in a solution approaching closer to each other, the main forces acting between them can be explained by the electrostatic double layer and van der Waals forces as outlined by DLVO theory discussed above and they interact based on the screened Coulomb interaction. We have mentioned in section 1.51 that the attraction due to van der Waals is irrelevant in our work and the tendency of particles to attract and aggregate can only be explained by the length scale interaction between them. The repulsion at a closer separation triggered between two charged particles, surrounded with a double layer mainly consists of counterions, caused by entropy rather than electrostatics (Israelachvili, 2011; Ohshima, 2006a). Upon dissociating from the surface, the counterions tend to be present in the bulk but the coulombic attraction between the surface keeps them near to the charged surface. In the diffuse double layer region, the counterions are osmotically repelling each other so as to increase their configurational entropy. When two surfaces approach each other, the counterions are forced back onto the surface, against their preferred equilibrium state, lowering their entropy, thus causing repulsion between two surfaces (Israelachvili, 2011).

The interaction between two charged microspheres with double layers can be simplified by using the linearised Debye-Hü ckel approximation of low potential. Consider two similar significantly-charged spheres separated by a distance r, immersed in a 1:1 electrolyte, the interaction potential can be expressed as (Ohshima, 2006a),

$$U(r) = \frac{1}{4\pi\epsilon_r\epsilon_o}\psi^2 a^2 \frac{\exp - \frac{r-2a}{a}}{r}\gamma \tag{1.26}$$

where γ is a term referring to the double layer interaction, depending on whether the particle possesses a constanst surface potential or surface charge. For a system where the Debye length is large with respect to the particle radius (diffuse double layer), $\kappa a \ll 1$, the electrostatic double layer potential can be expressed as,

$$U(r) = \frac{Z^2}{4\pi\epsilon_o\epsilon_r}\frac{\exp(-\kappa(r-2a))}{(1+\kappa a)^2 r} \tag{1.27}$$

where Z_1 and Z_2 are the magnitude particle charges with same radius a separated at a distance r.

DVLO theory explains the combination of energies driven in the colloidal system including van der Waals attraction, electrostatic repulsion, steric stabilization and other contributing forces. In practice, not all contributions are necessary for one system. Realistically, for our system, only the van der Waals and double layer terms are relevant. The overall DLVO plot is a plot of changes of energy with respect to the separation between colloids. When colloids are approaching each other, the energy reaches a shallow well, known as the secondary minimum. Particles are not at the lowest energy state at the secondary minimum. Generally, if flocculation happened, particles could form stable a dispersion again. The primary maximum acts as an energy barrier, which, particles have to exceed to aggregate. At this distance, the repulsion between particles results from overlapping of the double layer and repulsion due to osmotic pressure as discussed earlier in this chapter. The primary minimum is when the particles possess the lowest energy state. The trend of the overall DLVO plot is largely influenced by the ion concentration in the colloidal system. The energy barrier (primary maximum) becomes less apparent and the secondary minimum starts to appear with increasing ion concentration. When the energy barrier diminishes, the colloidal system is unstable and at that salt concentration, the point is known as the critical coagulation concentration (Everett, 2007; Verwey and Overbeek, 1948; Behrens and Borkovec, 2000).

Next, we discuss briefly the two important models determining the pair

interaction potential; constant surface charge (CSC) and constant surface potential (CSP). CSP is the most common model where the surface charge varies with separation between particles. The surface charge decreases as two particles come closer and eventually becomes zero when the particles are in contact. The CSP model has more accuracy with DLVO interactions where the surface charge has a large dependency on the separation between particles. In this thesis, we use AOT to alter the electrostatic interaction between PMMA particles. For this system, it is likely that the surface potential is independent of the concentration of AOT micelles added (Roberts et al., 2008). CSC is different model where the surface charge remains constant with particle separation, whilst the surface potential changes. This model is applicable to our highly-charged IM-PMMA system. In between these two extreme regimes, a model known as the charge regulation (CR) model, where both particle charge and potential varies to adapt the separation between particles, especially when both double layers interfere.

We now briefly introduce a useful method to measure the interaction between two colloidal particles, known as optical tweezing. Optical tweezers (or blinking optical tweezers, BOT) were invented by Arthur Ashkin in the 1970s to detect the optical scattering and gradient forces of microparticles (Ashkin, 1970) and is now widely used in the characterization of biological cells and motors and also viscoelastic properties of biopolymers. A focused laser beam is used to trap and manipulate the dielectric particles in three dimensions. The narrowest part of the beam contains the strongest electric field gradient. The particles are strongly attracted to this region and the trap must be strong enough to overcome the radiation pressure and other thermal forces (Grier, 1997). The distance between the particles can be manipulated to measure how much force they can withstand depending on the separation. Important physical and optical properties of both particles and solvents such as dielectric constant, refractive index, viscosity and diffusivity have to be taken into account in order to obtain compatibility in the system for the experiment. In this thesis, we regularly used the data analyzed by former and current members of the group namely, Dr Samuel Finlayson, Ms Franceska Waggett and Ms Charlotte Pugsley. Most BOT data are referred to compare the behaviour of colloids in the bulk in chapter 3, 4 and 5. To analyse the data, we use an expression for DLVO repulsive interactions in section 1.52, considering the magnitude of the charge of the pair is equal where the electrostatic energy can be written as,

$$U(r) = \frac{Z^2}{4\pi\epsilon_o\epsilon_r}\frac{\exp(-\kappa(r-2a))}{(1+\kappa a)^2 r} \tag{1.28}$$

$$F(r) = -\frac{dU}{dr} \tag{1.29}$$

$$F(r) = \frac{Z^2}{4\pi\epsilon_o\epsilon_r}\frac{\exp(-\kappa(r-2a))}{(1+\kappa a)^2}(\frac{1}{r^2}+\frac{\kappa}{r}) \tag{1.30}$$

The force-separation profile between a pair of particles is tabulated in the chapters mentioned above based on equation 1.30.

1.6 Thesis Outline

This thesis is composed of six chapters. The fundamental aim of the thesis is to explore the electrostatic charging and electrokinetics in non-aqueous solvents and its contribution to industrial applications such as inkjet printing. Throughout the thesis, charged colloidal particles are used and two types of species were used to alter the electrostatic behaviour. Images collected for this thesis were obtained using the confocal microscope. We gather observations from literature and experiment, then the cause and effect of such observations were analyzed based on theories and calculations.

Chapter 2 discusses the experimental techniques and materials used for the experiments. Brief synthesis procedures of the particles and materials are described in this chapter.

Chapter 3 describes the underlying theories of the attraction and abnormality in Debye length when an organic electrolyte was added into the PMMA/ dodecane colloidal system. This arose from an unusual observation where we spotted the aggregation and organization of colloids in dodecane. The conductivity was measured to analyze the density of ions with respect to electrolyte concentration. Force measurement was made using the blinking optical tweezer (BOT) to compare the interactions between two interacting colloids. The experimental force measurement data was collected by Miss Franceska Waggett (Waggett, 2019).

Chapter 4 introduces the concept of ionic liquids and the effect on its concentration towards the organization of colloidal particles in non-polar solvents. Conductivity measurements were performed to identify the density of ions in the system. The model study of this chapter is based on Chapter 3.

Chapter 5 discuss the deposition patterns of evaporating colloidal droplets and focuses on the effect of evaporation kinetics. We used two different types of non-solvents and the deposition patterns are compared based on thermodynamic properties of the solvents. The concept of Peclet number and solvent evaporation velocity are introduced in this chapter. Finally, we tailored our system with a previous

theoretical study, where the contact line friction of the droplet is largely influenced, by the concentration of AOT added into our system.

Chapter 6 is a follow-on from Chapter 5. We investigate the role of electrostatics of colloids in the bulk solvent on the deposition patterns of evaporating non-polar colloidal droplets. The effect of particle charging on the deposition patterns is discussed. The effective particle charge is analysed using electrophoretic mobility data.

Chapter 7 concludes all chapters with a correlation made to explain the effects of electrostatic interactions between colloids and the evaporation kinetics on the evaporation application.

Chapter 2

Materials and Methods

Chapter 2 mainly discusses the experimental procedures and materials used for all works presented in this thesis. Detailed procedures on results analysis using software packages and specific instruments used will be discussed in the result chapters.

2.1 Colloidal Particles

2.1.1 The Synthesis of Poly (methyl methacrylate)

Poly(methyl methacrylate) (PMMA) particles were used throughout the project and will be discussed in this thesis. PMMA particles were stabilized with poly(12-hydroxystearic acid) (PHSA) as a stabilizing layer surrounding the PMMA particles as illustrated in Figure 2.1 mainly to eliminate aggregation induced by van der Waals forces. A fluorescent dye, DilC18 was used to label the particles in order to be observed under a fluorescent confocal microscope.

The PMMA was synthesized by Dr. Andrew Campbell using the one-pot free radical polymerization reaction outlined by Antl et al. (Antl et al., 1986). The monomers, methyl methacrylate and methacrylic acid were initially added into a

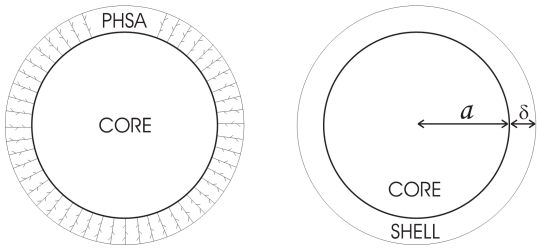

FIGURE 2.1: Illustration of the PMMA colloid with a stabilizing PHSA layer, a = 775 nm and δ =10 nm (Finlayson, 2016a)

mixture of hexane and dodecane, to polymerize with the free radical initiator, azobisisobutyronitrile (AIBN). Then the PHSA stabilizer and chain transfer agent, octanethiol were added into the hexane and dodecane-based mixture. The mixture was then heated at about 80 ^{o}C for two hours until the mixture turns opalescent and well-dispersed. A locking agent, diethanolamine was added to ensure the PHSA stabilizing layer is properly attached on the particles surface and the reaction was left overnight at approximately at 120 ^{o}C. The fluorescent dye DilC18 was then incorporated for observation under the confocal microscope.

The particles were then centrifuged using a high-speed preparative centrifuge at 5000 rpm for 10 minutes. The supernatant was replaced with the dried solvent and the centrifuging process was repeated until the conductivity of the supernatant reached the conductivity of the pure solvent ($\approx$ 3 pScm^{-1}). The washed particles were dried in a vacuum oven at 80 ^{o}C overnight until the solvent has fully evaporated. The dispersion of dried PMMA particles then were made in desired solvents.

2.1.2 The Synthesis of Poly-ionic Liquid particles

The ionic monomer particles (referred as IM-PMMA throughout this thesis) were synthesized by replacing the methacrylic acid with an ionic monomer. The monomer was initially synthesized by Hussain et al. and Sanchez et al (Hussain, Robinson, and Bartlett, 2013). The ionic liquid precursors were first prepared by an ion exchange reaction. The quarternary ammonium bromide salt was dissolved in methanol and added to a methanolic solution containing sodium tetrakis (3,5-bis (trifluoromethyl) phenyl) borate. The mixture was then evaporated until the solution vanished and the white precipitate was rinsed with diethyl ether and recrystallized from acetone. The product was then dried in vacuum oven. The ionic liquid monomers were prepared using a three-step synthesis procedure. The full synthesis reaction can be traced from Hussain et al (Hussain, Robinson, and Bartlett, 2013). Finally, the polymerization process was carried out using an initiator, monomers, a stabilizer and a chain transfer agent in a hexane and dodecane mixture. The proportion of ionic liquid monomer was varied and in this thesis, we used [ILM-C_{12}][TFPhB]. For this system, the concentration of IL monomer added was 4 wt. % with the overall particle radius of 1255 nm (600 nm of the IM2 cation and 655 nm of the TFPhB anion) as the molecular structure depicted in Figure 2.2. The fluorescent dye DilC18 was then incorporated for observation under the confocal microscope.

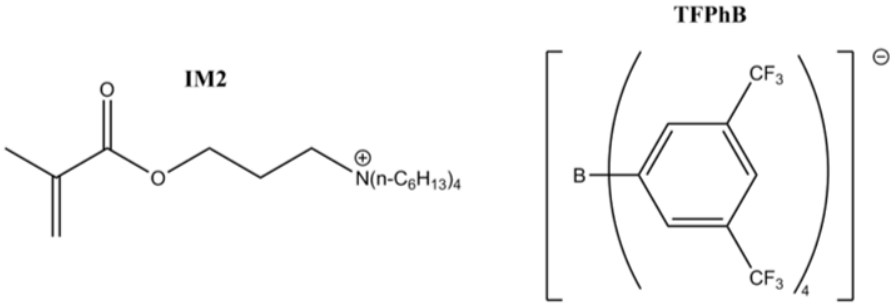

FIGURE 2.2: Molecular structure of [ILM-C_{12}][TFPhB] (Hussain, Robinson, and Bartlett, 2013)

2.2 Purification of dioctyl sodium sulfosuccinate (AOT)

AOT (molecular struture depicted in Figure 1.3) was purchased from Merck and used as a charge inducer in the non-aqueous system. AOT was first purified to remove excess impurities from synthesis and manufacturing. AOT was dissolved in methanol until the formation of white precipitate is seen, and then it was filtered off. The excess methanol was then removed and AOT was dried in vacuum oven for 48 hours.

2.3 The Synthesis of Tetradodecylammonium tetrakis (3,5-bis (trifluoromethyl) phenyl) borate (TDAT) electrolyte

An equimolar amount of tetradodecylammonium bromide and sodium tetrakis (3,5-bis (trifluoromethyl) phenyl) borate were dissolved in methanol and then combined. The mixture was stirred until no precipitate formed. The methanol was then evaporated until the oily brownish liquid formed with NaBr particulates sedimented at the bottom of the beaker. The mixture was redissolved with diethyl ether and then the solvent was evaporated. The product was washed with distilled water for three times to remove NaBr. The organic layer was then transferred into a beaker and the excess solvent was evaporated. The product was recrystallized with hexane for two to three times until a pure electrolyte obtained. The electrolyte was confirmed from 1H and 19F NMR spectrum and an elemental analysis result. The calculated elemental analysis for $C_{80}H_{112}BF_{24}N$: C, 61.81 %; H, 7.3 %; N, 0.9 %. Found: C, 62.61 %; H, 7.27 %; N, 1.1 %. NMR analysis: H NMR (400 MHz, $CDCl_3$) 0.89 (9H), 1.26 (76H), 3.01 (8H), 7.32 (8H), 7.54 (4H), 7.65 (8H). F NMR (377 MHz, $CDCl_3$) -61.1. The molecular structure of TDAT electrolyte is depicted in Fig 2.3.

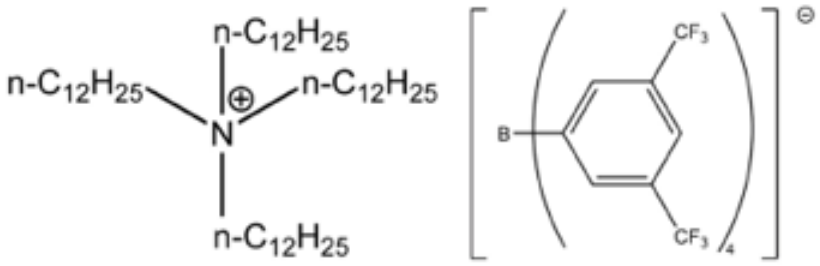

FIGURE 2.3: Molecular structure of TDAT electrolyte (Finlayson, 2016a)

2.4 Confocal Microscopy

A Zeiss LSM 510 confocal microscope was used to image the behaviour of the colloidal particles in suspensions. Confocal microscopy is based on a dynamic focus-detection technique together with a closed-loop feedback system and it illuminates and images the sample one point at one time through a pinhole. A Helium-Neon (HeNe) laser with a wavelength of 632.8 nm was used as a light source, passed through a semi-silvered mirror, focused by high a numerical aperture objective lens to a diffraction-limited spot at the focal plane. The displacement of the objective lens determines the vertical dimension of the surface topography if the light spot is focused on a surface by adjusting the objective lens vertically during the scanning process. The focal plane is adjusted and the intensity of detected light received by the photodetector. The samples were prepared in a 100 μm thick capillary tube, laying horizontally flat on a glass microscope slide. Occasionally, the particle spacers, Spheromers 20 (Silica particles with the diameter of 20 μm) were used to reduce the effective working distance between the focal plane and the focus lens to mimic the conventional capillary tube (narrowest spacing = 100 μm). The Spheromers were added into the stocks at the amount that is sufficient to hold the microscope glass coverslips (Area = 22mm x 22mm), to support the weight of the glass slip as the stocks were sandwiched in between two glass slips. The scanned images were analyzed using the Java-based image processing program, FIJI/ ImageJ.

2.4.1 Confocal Microcopy Imaging and Particle Size Analysis

All result chapters in this thesis contain images mapped using the confocal microscope. Images were analyzed using the free software, ImageJ or FIJI (Schindelin et al., 2012; Schneider, Rasband, and Eliceiri, 2012). The background noises from the image were removed prior to the image processing. Then the sharpness and smoothness of the image were modified since image analysis is performed on an image with

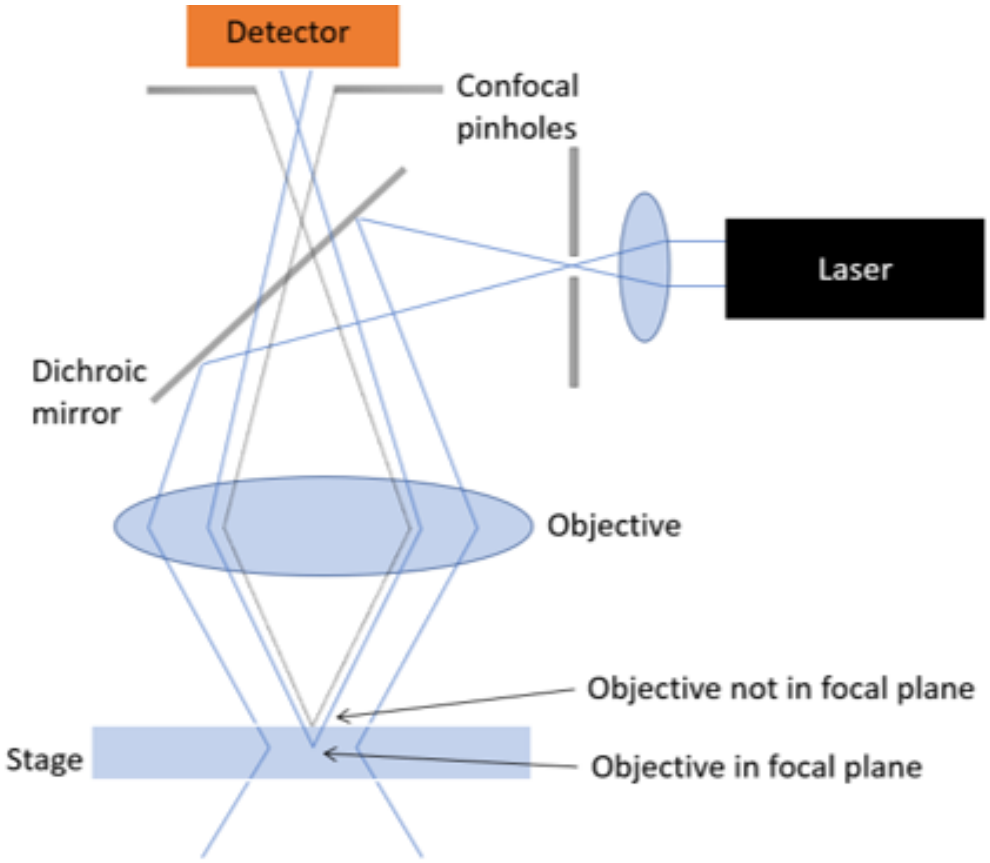

FIGURE 2.4: Illustration of the confocal microscope

high contrast and dark background. During the image sharpening, the noise can be possibly revealed as this is more noticeable with images of noisy background, so there needs to be a balance between obtaining a sharper and smoother image depending on the quality of the raw image. If needed, a filter is applied to the images, but this hinders the clarity and sharpness of the image.

In Chapters 3 and 4, we present the analysis of images using confocal microscopy and ImageJ. We present the average particle or cluster size in each system. This was performed initially by using the 'Analyze' command in the software. Prior to analyzing the images, the threshold of the images must be set up by considering the circularity and expected minimum and maximum particle size (usually set from '0 to infinity'). This step can be manipulative as the brightness and intensity of the image has to be altered before measuring the particle size. We simply outline the settings to acquire the known size of the particle (1.55 μm) to sustain the reliability of the analysis. The desired measurement unit can be set up by converting the value with the base image measurement, which is in pixels. The raw data reveal the particle size based on the circularity set up prior to the analysis. A histogram can be generated to obtain the area distribution of the fluorescent measured and an overlay produced maps out the location of the measured entity in the image.

2.5 Blinking Optical Tweezers (BOT)

Prior to the experiment, samples were siphoned into a rectangular borosilicate capillary tube, purchased from CM Scientific with an internal dimension of 0.1 × 2 mm. The capillary was then sealed at both ends on a microscope glass substrate using Norland optical adhesives, and subsequently the glue was cured with a UV lamp. The sample then was placed upside down on the microscope stage.

The blinking optical tweezer (BOT) data used in this thesis are courtesy of Ms Franceska Waggett, Dr Samuel Finlayson (Finlayson, 2016b) and Ms Charlotte Pugsley. The overall instrument design was based on the methods outlined by Martin-Badosa and coworkers, and assembled by Dr Ian Williams (Martín-Badosa et al., 2007). The unit was set up on top of a gas floatable optical table and consist of a 5W 1064nm Nd:YAG laser (IPG Photonics) with an inverted bright-field microscope (Axiovert 200, Carl-Zeiss).

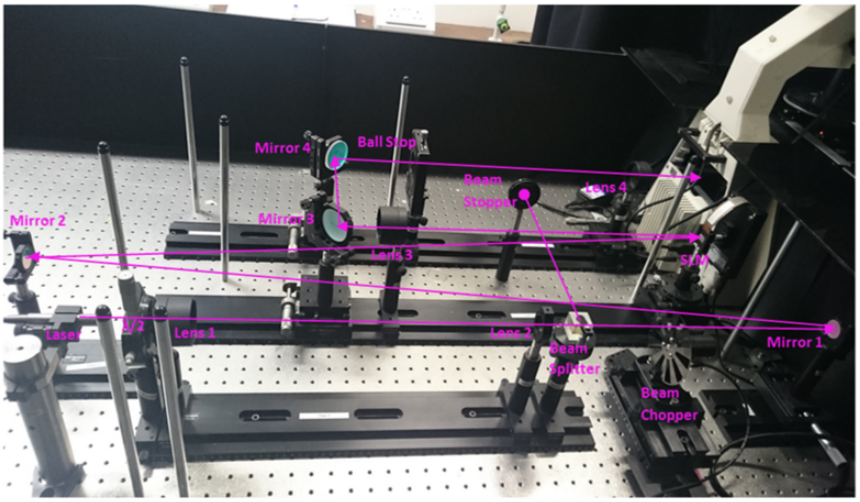

FIGURE 2.5: BOT optical setup (Waggett, 2019)

Figure 2.5 illustrates the laser beam path in the optical setup. Initially, the laser generated from the source passes through the half-wave plate ($\lambda/2$) and the beam splitter to vertically polarized the laser. To increase the beam width, the laser beam passes through the Lens 1 and Lens 2 to overfill the spatial light modulator (SLM). The beam chopper functions to periodically turn the laser on and off, with a disc rotating at 20 Hz, resulting in a continuously oscillating laser on and off for 25 ms each cycle. The beam stopper collects the unused beam from the beam splitter. The tracking data are collected when the laser is off and identified by an in-built detector in the chopper. The laser beam is reflected by mirrors 1 and 2, onto the SLM. Next, the light is passed through lenses 3 and 4 to expand the beam width once again, in order to obtain a width wider than the objective aperture.

The laser beam is used to track the particles and the beam splitting allows

the tracking to be done on multiple particles at once. When the laser is off, particles are exposed to the thermal Brownian fluctuations and images are taken using a high-speed camera at 500 fps, allowing the particles trajectories to be measured by the particle displacement over time. The data are combined and analyzed to generate the particle velocity, diffusion and force profiles. Detailed procedures and data generation from the experiment can be extracted from (Finlayson, 2016b; Waggett, 2019).

2.6 Phase Analysis Light Scattering (PALS)

The electrophoretic mobility of the colloidal dispersion was measured using a Malvern Zetasizer Nano Z instrument, operating a 4 mW laser at a wavelength of 633 nm. The stock solution was prepared with the accordance of the particle volume fraction and then transferred into 3.5 mm (two-polished windows) square glass cuvette (Hellma). The measurement was made using a Malvern dip cell for non-aqueous solvent at a driving voltage between 20 and 140 V.

2.7 Dynamic Light Scattering (DLS)

A Malvern Zetasziser Nano S operating at a wavelength of 532 nm was used to determine the hydrodynamic particle diameter and average particle/clusters size of the non-aqueous colloidal system. The solvent was first diluted and filtered to remove dust and impurities before adding it with the sample. The samples then were placed into square 3.5 mm glass cuvettes with four-polished windows (Hellma) and inserted into the instrument with the incident laser set up at 90^o. The count rate recorded was observed at a scattering intensity of about 100kcps, indicating the concentration of the sample.

2.8 Conductivity Measurement

The conductivity measurement was performed at 25^0C, using the Scientifica conductivity meter model 627, with an operating frequency of 15 Hz. A cylindrical concentric stainless steel probe was immersed in the solution and the reading was recorded once the meter reached a consistent value. The probe was rinsed thoroughly with solvent until the reading reads the conductivity value of the solvent (for dodecane, > 3 pS/cm) before starting to measure the conductivity of the solution again.

2.9 Surface Tension Measurement

Surface interfacial tension between the solvent and air with added surfactant or salt was measured using a Kruss K100 Force Tensiometer, using the pull-off Wilhelmy plate method at 25^{o}C. A roughened platinum plate was brought towards the solvent surface at a force of 0.1 mN and the interfacial force value was recorded through a force sensor attached to the tensiometer. The surface tension measurement was performed to confirm the formation of a micelle-like structure of an electrolyte..

2.10 Solvent Purification

Dodecane, hexane, tetrachloroethylene and mixed-isomer decahydronaphthalene (decalin) were the main solvents used in the project. They were purchased from Acros, Fischer and Aldrich and placed over 4 Å$\sim$ 10 mesh molecular sieves for at least 24 hours to remove excess water prior to usage. The conductivity of each solvent was measured prior to use and compared with values from literature to preserve the purity of the solvent.

Chapter 3

Electrolyte-Induced Attraction

This is a first result chapter which discusses the interparticle interaction between PMMA colloids, modified by the addition of an electrolyte. Experimental results in this chapter are produced from a project collaborated with Franceska Waggett [1]*. Colloidal systems used in this particular work were made up in a number of non-aqueous solvents with a range of dielectric constants to prove on discussed theories. The key results are the inflation of the screening length and particle attraction triggered by the electrolyte concentration. Justifications of the observed results and analysis will be discussed supported with preliminary experimental findings. Some disproving theories will also be discussed as a number of experiments were attempted to prove the underlying causes of the mentioned key results.*

3.1 Introduction

The interactions between colloidal particles in a dispersion medium is largely influenced by the bulk properties of the overall system. Attractive (and repulsive) interactions between colloidal particles measure the stability of the system, in which sometimes, the organization and structuring of colloids are favoured by industries, depending on applications such as imaging and mapping (Khan, Saeed, and Khan, 2017). Fundamentally, the stability of a colloidal system can be explained by classical DLVO theory, which measures the balance between electrostatic repulsion and van der Waals attraction as mentioned in Chapter 1. In non-polar solvents, where the charging phenomenon is unlikely and the van der Waals interaction can be less dominant or negligible, where the colloids are surrounded by a stabilizing layer. Generating a charge-stabilized colloidal system can be achieved by altering the electrostatic interactions via numerous methods, such as adding surfactants, electrolytes and charge-bearing additives (Sen et al., 2012; Kobayashi et al., 2005; Belloni and Spalla, 1997). However in some systems, the surface charge is not affected by these additives, but the particle attractions can be generated (Finlayson, 2016a; Smith et

[1] Work contributions for this chapter: (FW) Blinking Optical Tweezers data. (MS) Confocal microscopy imaging and conductivity measurements

al., 2017). Finlayson and Smith initiated this experiment when an organic electrolyte was added into sterically-stabilized PMMA colloids in dodecane, and attractions between PMMA colloids were spotted. It is known that the addition of electrolytes or salts in a charge-stabilized colloidal system significantly affects the screening length due to the number of ions dissociated in the solvent and colloidal clusters formed due to the domination of the attractive term. However, the causes of cluster and aggregate formation in uncharged non-polar colloidal systems due to these additives is unexplanined and possibly not electrostatic in origin, considering the PMMA core is sterically-stabilized by a PHSA layer.

In this chapter, we present an analysis of the formation of colloidal aggregation and solve possible origins of this phenomenon. We also reveal the unusual trend of the screening length at high TDAT concentrations and compare the aggregation behaviour with the deposition pattern of an evaporating colloidal droplets.

3.2 Experimental

PMMA colloids were synthesized by Dr Andrew Campbell using the synthesis procedure outlined in Chapter 2. The volume fraction ϕ of PMMA $\sim 10^{-4}$ was used throughout this experiment. The concentrations of TDAT were varied from 40 μM to 750 μM. The stock solutions were made using centrifuged PMMA (refer Chapter 2) in dodecane. In a later series, we used a mixture of tetrachloroethylene, TCE and mixed-isomer Decalins to alter the dielectric constant of the carrying solvent and the overall physical properties as tabulated in Table 3.1 below. Dodecane was purchased from Alfa Aesar, and both TCE and Decalins were purchased from Merck. All solvents were dried prior to use to eliminate residual water content.

System	ϕ **TCE**	ϕ **Decalins**	ρ, **g/mL**	**Refractive Index**
Dodecane	-	-	0.750	1.421
TCE20	0.2	0.8	1.041	1.477
TCE30	0.3	0.7	1.114	1.481
TCE50	50	50	1.265	1.488

TABLE 3.1: Physical and optical properties of solvents used

The conductivity of the stock solution was measured using the conductivity meter model 627 Scientifica. The same stock solutions were used to image particle attraction and, cluster and aggregate formation using confocal microscopy, and to measure the force-separation profile using blinking optical tweezers (BOT). Finally, the stock solution was dispensed using a microsyringe to make a spherical cap droplet on a hydrophobically-coated glass substrate for the evaporation experiment.

Further details on the evaporation kinetics of colloidal droplets will be discussed in Chapter 5.

3.3 Particle Attraction

3.3.1 Optical Observation and Turbidity

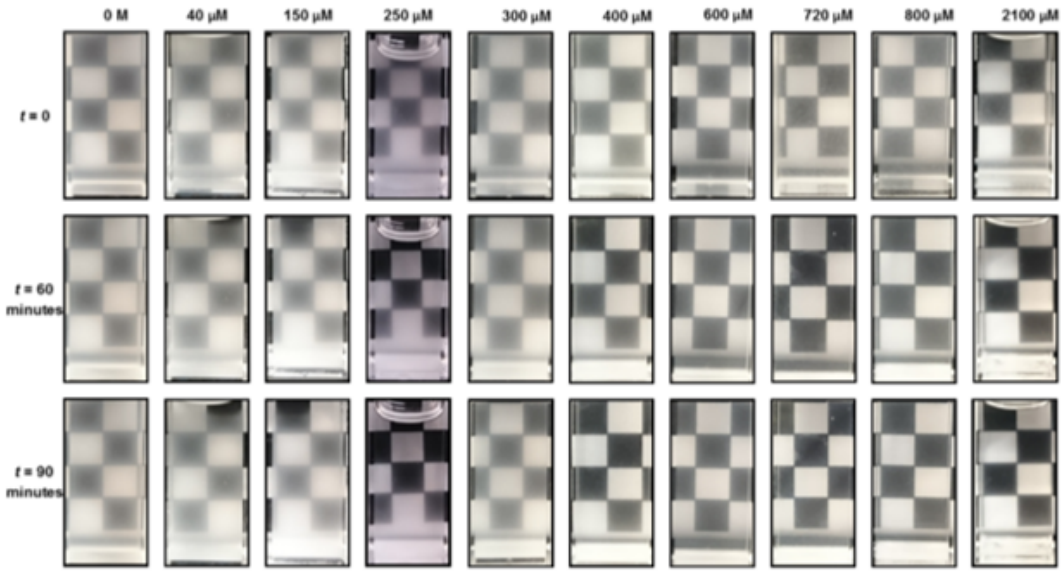

FIGURE 3.1: Preliminary optical observation on the sedimentation time of PMMA in dodecane with varied TDAT concentration

Figure 3.1 shows the overall sedimentation time of the PMMA/dodecane colloidal system with increasing concentration of TDAT. The sedimentation time provides us with an initial idea on the dependency of PMMA aggregation with TDAT concentration. Optically, the turbidity of the solution decreases with TDAT concentration and a clear solution is achieved at a shorter time in systems with higher TDAT concentrations. TDAT was added at a very high concentration (>720 μM) only to optically observed the turbidty of the solution. No reliable measurements can be made at this regime as the particles aggregation formed immediately after the dispersion was prepared. The solubility limit of TDAT electrolyte at room temperature is $\sim$ 1mM, so an external dispersing energy such as heating, was required to make solutions beyond this regime.

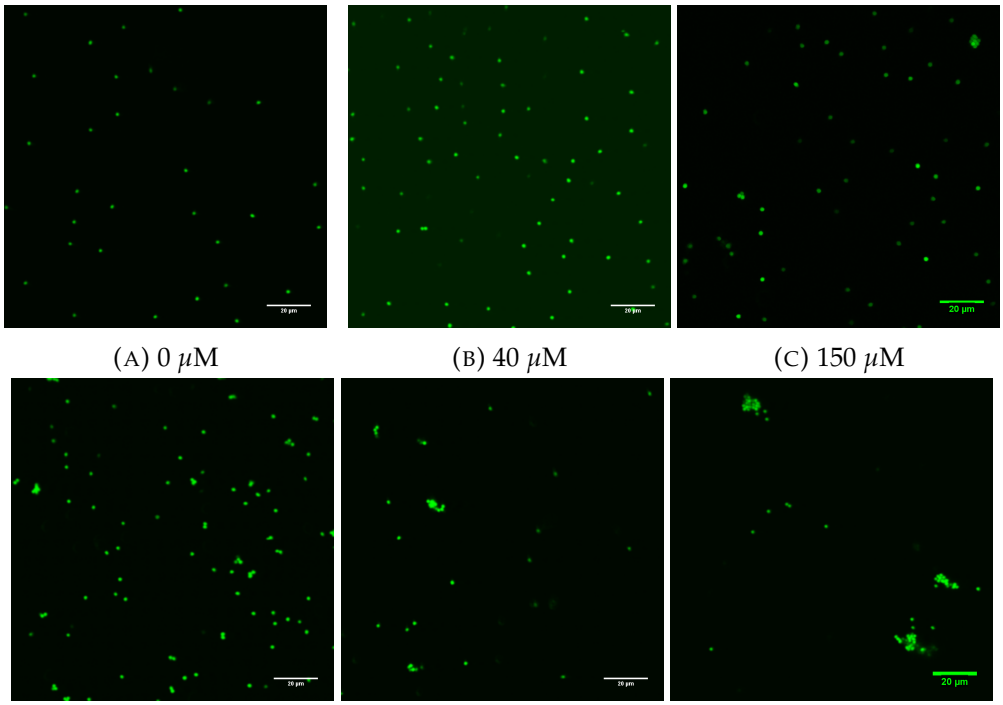

(A) 0 μM (B) 40 μM (C) 150 μM

(D) 250 μM (E) 350 μM (F) 450 μM

FIGURE 3.2: Formation of clusters and aggregates of PMMA colloids in dodecane varied with TDAT electrolyte concentration

3.3.2 Confocal Microscopy Images and Analysis

The variation of TDAT electrolyte concentration induced attractions between colloidal particles in dodecane. This section shows the dependency of cluster and aggregate formation with the concentration of TDAT electrolyte.

Figure 3.2 illustrates the evolution of PMMA clusters and aggregations formed in dodecane with increasing TDAT concentration. The cluster formation becomes apparent at [TDAT] $\geqslant$ 150 μM. Without any TDAT, the particles are evenly distributed in the bulk solution and a number of doublets and triplets start forming when TDAT was added at 40 μM.

Figure 3.3 portrays a higher magnification of clusters and aggregates images (126x) compared to Figure 3.2.The formation of small clusters was initially spotted with the average number of particle in a cluster $N_{ave} \leqslant 4$ at TDAT concentration $\leqslant$ 40 μM. As the concentration of TDAT was increased up to 350 μM, $N_{ave} \leqslant 100$ and large aggregates formed with $N_{ave} \geqslant 1000$ at TDAT concentration $\geqslant$ 450 μM. At TDAT concentration $\geqslant$ 550 μM, particles in dodecane were hardly existed as single particles as aggregations formed immediately after the dispersion prepared. This

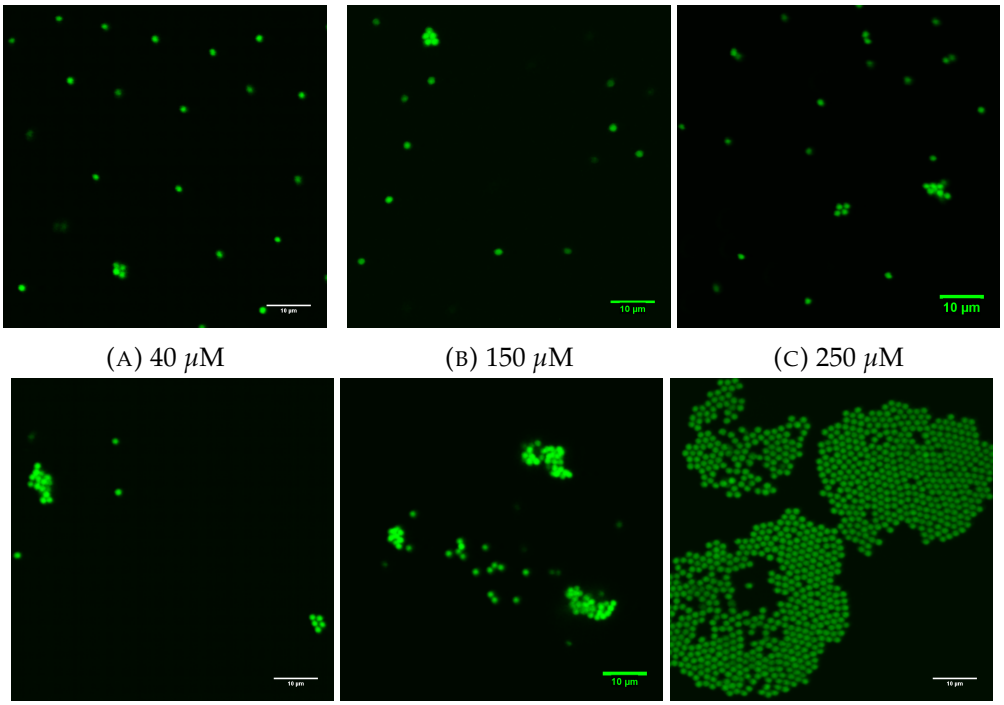

(A) 40 μM (B) 150 μM (C) 250 μM

(D) 350 μM (E) 450 μM (F) 550 μM

FIGURE 3.3: Formation of clusters and aggregates of PMMA colloids in dodecane varied with TDAT electrolyte concentration

can be quantitatively illustrated in Figures 3.4 and 3.5. Figure 3.6 shows the dependency of the average cluster and aggregate size with the TDAT concentration. Below 40 μM, the particles exist as singlets and the cluster start forming at [TDAT] $\geqslant$ 50 μM and the onset for formation of larger clusters or aggregation is when TDAT was added at about $\geqslant$ 350 μM.

3.3.3 Force Measurement and Particle Charge

The force $F(r)$ profile with respect to separation between two PMMA colloids r can be measured using blinking optical tweezers (BOT). The resulting plot in Figure 3.7 can be expressed from equation:

$$F(r) = \frac{Z^2}{4\pi\epsilon_o\epsilon_r}\frac{\exp(-\kappa(r-2a))}{(1+\kappa a)^2}\left(\frac{1}{r^2}+\frac{\kappa}{r}\right) \tag{3.1}$$

with Z is the particle charge, e is the elementary charge, κ is the inverse screening length, a is the colloid radius, ϵ_r is the relative permittivity of solvent and

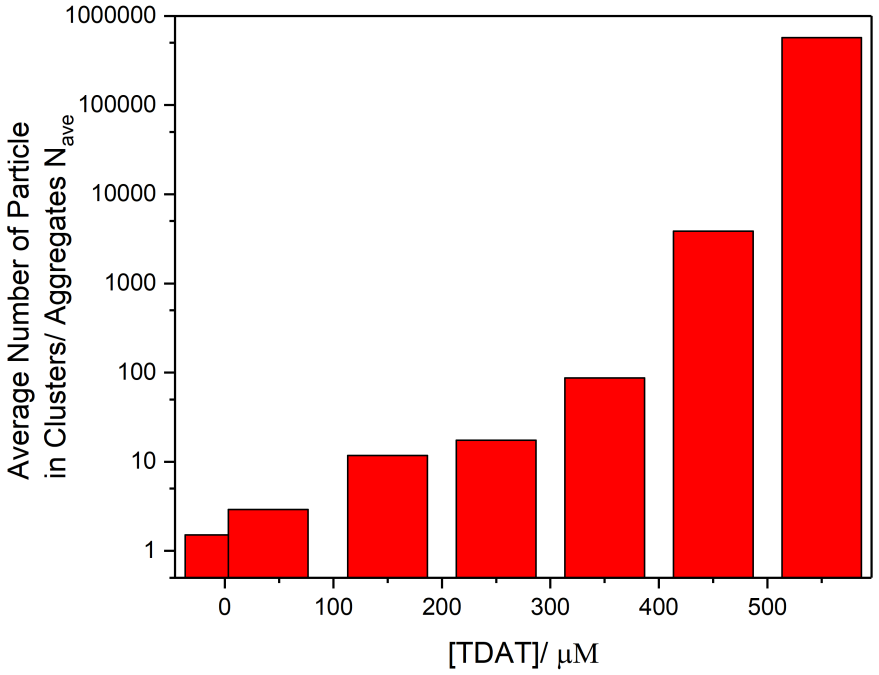

FIGURE 3.4: Average number of PMMA particle per cluster and aggregate N_{ave} in dodecane with respect to TDAT concentration

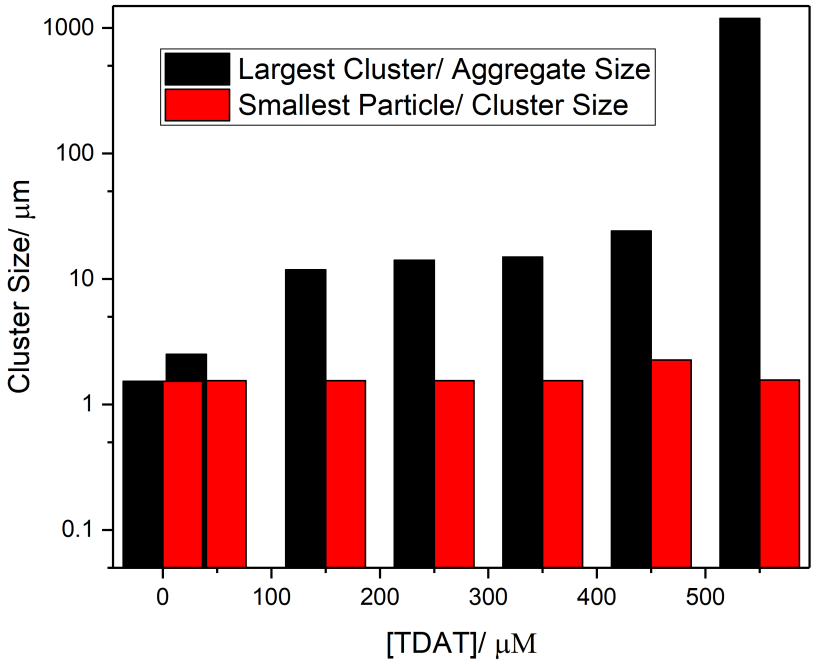

FIGURE 3.5: Comparison between average smallest and largest cluster size varied with TDAT concentration

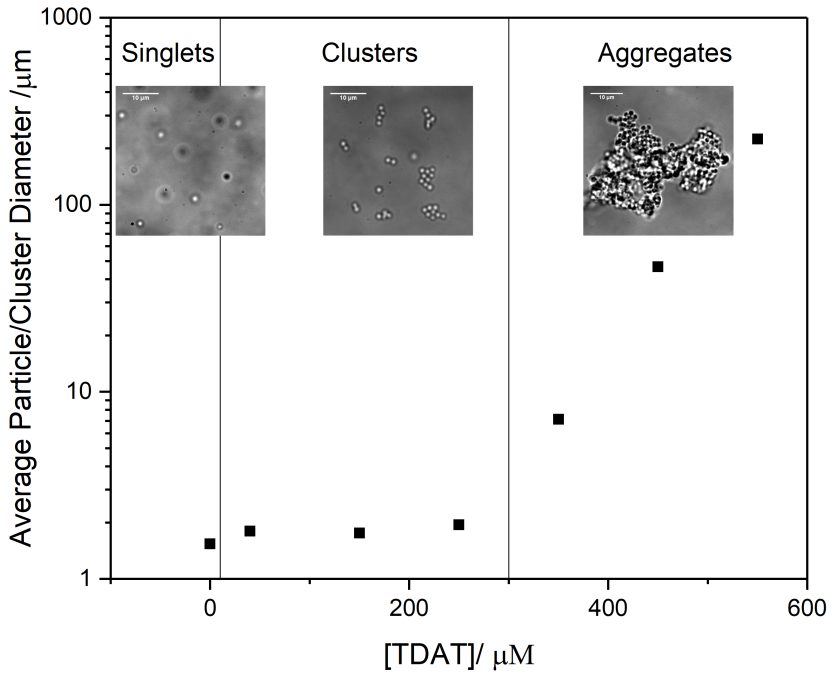

FIGURE 3.6: Comparison between average smallest and largest cluster size varied with TDAT concentration

ϵ_o is relative permittivity of vacuum. The force plot in Figure 3.7 is in a good agreement with the images of cluster and aggregate formation illustrated in Figure 3.3 and the phase transition in Figure 3.6. The range of electrostatic interaction has obviously undergoes a transition from long-range to a shorter range with increasing TDAT concentration. To quantify the effective particle charge Z_{eff} or $Z\lambda_B/a$, equation 3.1 can be rearranged to,

$$r^2F(r) = \frac{Z^2}{4\pi\epsilon_o\epsilon_r}\frac{\exp(-\kappa(r-2a))}{(1+\kappa a)^2}(1+\kappa r) \tag{3.2}$$

The plot of $r^2F(r)$ with respect to separation between particles gives the magnitude of charge Z with κ^{-1} is the screening length. The reduced charge is considered when the electrostatic screening is closed to the particle surface, derived from the reduced zeta potential yielding,

$$\zeta_{red} = \frac{e\zeta}{k_BT} \tag{3.3}$$

$$Z_{red} = \frac{Ze}{4\pi\epsilon R}\frac{e}{k_B T} = \frac{Z\lambda_B}{a} = Z_{eff} \tag{3.4}$$

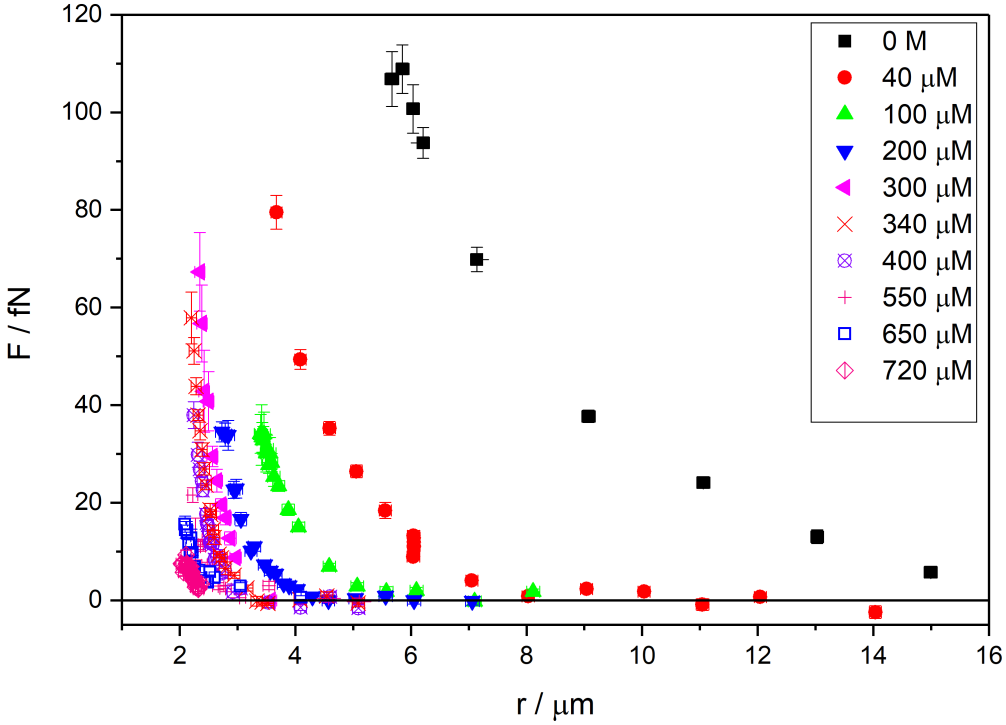

FIGURE 3.7: Force-separation profile between two PMMA colloids varied with TDAT concentration

The effective particle charge $Z\lambda_B/a$ on the other hand shows a non-monotonic dependence on the TDAT concentration. From Figure 3.8, the $Z\lambda_B/a$ declined with TDAT concentration initially at [TDAT] $\leqslant$ 100 μM, then a constant increase at 200 μM $\leqslant$ [TDAT] $\leqslant$ 450 μM and finally collapsed when TDAT was added more than 450 μM. Figure 3.9 shows the dependence of $Z\lambda_B/a$ on the TDAT concentration, calculated from electrophoretic mobility μ_e with solvent viscosity η, measured using PALS from the correlation,

$$Z_{eff} = Z\lambda_B/a = \frac{6\pi\eta\mu_e}{e}.\lambda_B \tag{3.5}$$

From Figures 3.8 and 3.9, it is obvious that the two methods of measuring the effective charge do not show an agreement especially at [TDAT] $\geqslant$ 150 μM. At this point, as mentioned earlier, the cluster formation becomes more apparent as

N_{ave} increases. Large cluster and aggregate formation results in an inaccurate electrophoretic mobility data as the cluster and aggregate tends to settle at the bottom of the sample cuvette, thus the frequency of scattered light detected from the particle movement in PALS can be unimportant.

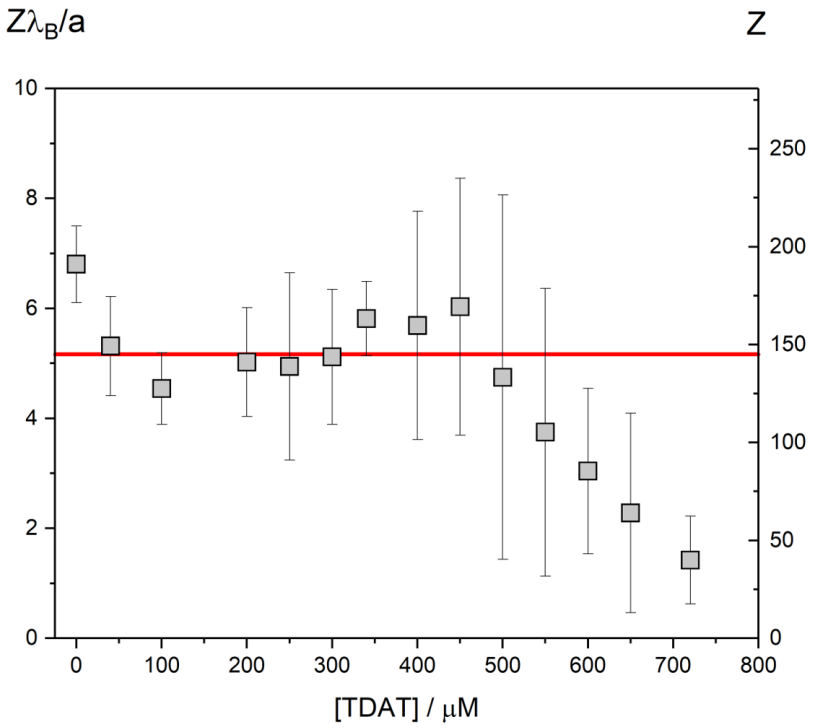

FIGURE 3.8: Effective particle charge of PMMA colloids fitted from force-separation profile using blinking optical tweezers (BOT) with respect to TDAT concentration

3.4 Screening Length

3.4.1 Conductivity and Ion Density

In solvents (of any dielectric constant), ions exist as charged spheres as the electrostatic force between two unlike ions results in attraction, forming a neutral ion pair. Any ion pairs with mutual potential energy, the interaction is given by Coulomb's law. When two individual unlike ions approach each other to contact, a certain amount of energy is required to separate them and if the energy is smaller than the kinetic energy of the solvent molecules, the ion pair will dissociate due to thermal agitation and vice versa. In electrolytic aqueous solution, the ions are mostly

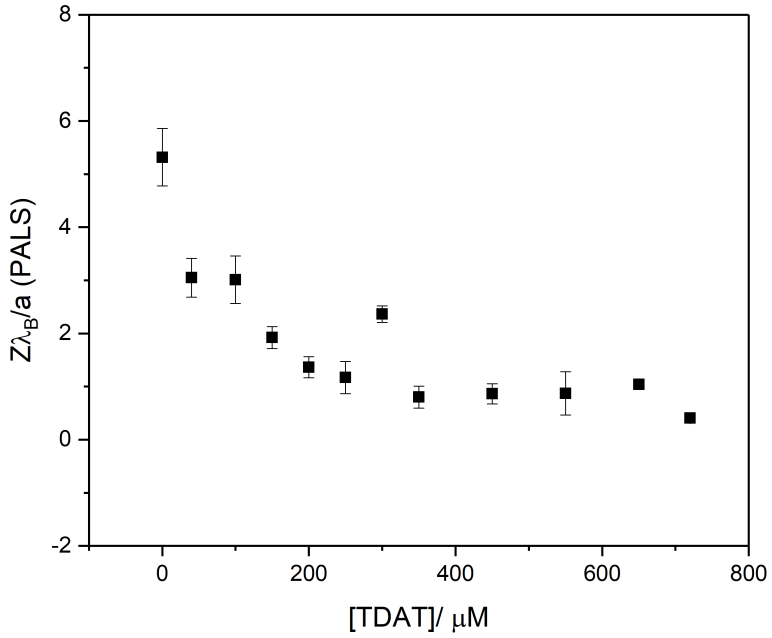

FIGURE 3.9: Effective particle charge of PMMA colloids measured using phase analysis light scattering (PALS) technique with respect to TDAT concentration

completely dissociated especially when the radii of the electrolyte $\geqslant$ 35 nm. Constrastingly, in low dielectric solvents, the Coulomb energy is too high for the recombination to occur, so the ions tend to exist as individual ions in solution (Kraus and Fuoss, 1933; Fuoss and Kraus, 1933b). Fuoss and Kraus outlined four distinct regions in conductivity against electrolyte concentration plot. When the concentration of electrolyte is zero, the conductivity decreases, then the value reach a minimum value. This is due to the electrolyte added existing as an ion neutral pair at a very low electrolyte concentration. The inflection point comes after where the ion concentration starts to build up and the ion pairs starts to dissociate. Finally the conductivity value increases rapidly with electrolyte concentration due to the abundant amount of free ions in solution (Kraus and Fuoss, 1933).

For solvent with low dielectric constant $\epsilon_r \leqslant 2$, the minimum point of conductivity appears at the region where the ion concentration is very dilute. Due to the existence of individual ions at low electrolyte concentration, the typical trend for conductivity-[electrolyte] plot as mentioned by Fuoss and Kraus can be invalid. We present the conductivity data for dodecane solution with TDAT electrolyte in Figure 3.10 to identify the correlation of specific conductivity K and ion density ρ_{ion} from expression,

$$K = (\frac{\rho_+}{N_A})\Lambda_+ + (\frac{\rho_-}{N_A})\Lambda_- + K_o \tag{3.6}$$

$$\rho_{ion} = \rho_+ + \rho_- \tag{3.7}$$

where ρ_+ is the number density of cations and ρ_- is the number density of anions, K_o is the conductivity of pure solvent and Λ_+ and Λ_- is the molar conductivity of cations and anions respectively. The total molar conductivity is the sum contribution of each ion, $\Lambda_o = \Lambda_+ + \Lambda_-$ and can be calculated using $\Lambda_{+-} = e^2 N_A / 6\pi\eta r_{+-}$ with η and r_{+-} is the solvent viscosity and cation/anion radius. The values of r_{+-} for TDAT are 0.585 and 0.44 nm (Hussain, Robinson, and Bartlett, 2013). To quantify equation 3.6, we assume the the cations A^+ and anions B^- mixture are dilute as the bound ion pairs dissociate into,

$$\text{A-B pair} \overset{k}{\rightleftharpoons} A^+ + B^- \tag{3.8}$$

The fraction of dissociated ion pair into free ions can be identified from α with dissociation constant J,

$$\alpha = \frac{1}{2J\rho_s}(\sqrt{1 + 4J\rho_s}) - 1 \tag{3.9}$$

with ρ_s is the total number density of salt. The fraction of dissociated cations or anions is $\rho_{+-} = \alpha\rho_s$ with number of ion pair $\rho_{IP} = (1 - \alpha)\rho_s$. The molar salt concentration is $c_s = \rho_s / N_A$ and when all ion pairs are fully dissociated, the maximum ion concentration is $2c_s$. So $\rho_s = (\rho_+ + \rho_-)/2 + \rho_{IP}$. Figure 3.11 illustrates the dependency of number ion density with [TDAT], which results in the trend of specific conductivity and the Debye length in Figures 3.10 and 3.12 respectively.

The trend of conductivity plot with TDAT concentration in Figure 3.10 explains the formation of triple ions at high TDAT concentrations. The conductivity K increases sharply at high TDAT concentrations after a gradual increase beyond the minimum point, where $K \propto [\text{TDAT}]^n$ and $n >> 0.5$. At high TDAT concentrations, the formation of triple ions is driven by the organization of complex ions cluster and this is predominantly observed in low dielectric solvents as the available Coulombic forces comtrol the ions clustering (Fuoss and Kraus, 1933a). The equilibrium between free ions and neutral dipoles can be written as:

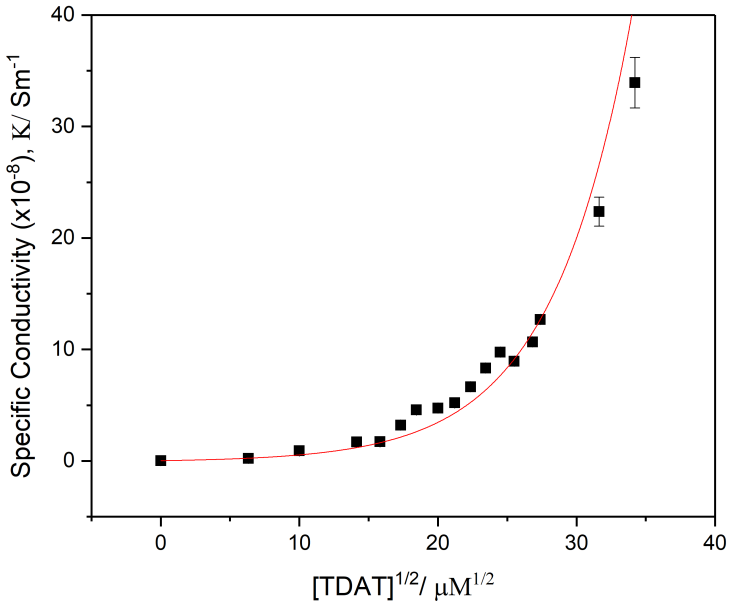

FIGURE 3.10: Dependency of specific conductivity with TDAT concentration

$$AB + A^+ \rightleftharpoons A_2B^+ \tag{3.10}$$

$$AB + B^- \rightleftharpoons AB_2^- \tag{3.11}$$

However, the fraction of arrangement of the complex triple ion formation, either (+-+) or (-+-) is still uncertain and can be too complex for us to justify at this stage. The Debye length is calculated using equation 3.12 with λ_B is the Bjerrum length,

$$\lambda_D = \frac{1}{\sqrt{4\pi\lambda_B\rho_{ion}}} \tag{3.12}$$

From Figure 3.12, it is obvious that the Debye length decreased monotonically with TDAT concentration as the number of ions in solution increases with TDAT concentration as depicted in Figure 3.11. This proves that ion concentration has inhibit screening of electrostatic interaction between colloids and this agrees with Debye-H*ü*ckel theory. However, at high TDAT or ion concentrations, the true

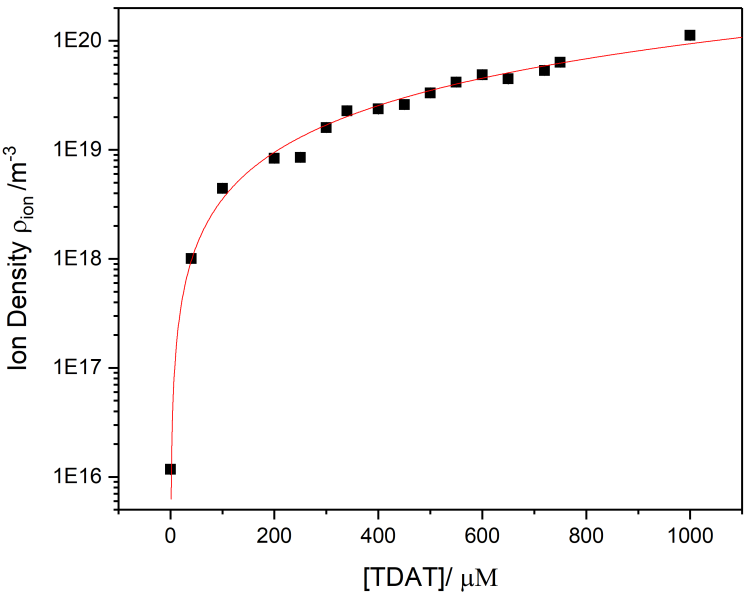

FIGURE 3.11: Ion density changes with TDAT concentration

screening length κ^{-1} deviates with the theoretical Debye length λ_D and obviously disagree with the classical Debye-H*ü*ckel theory (Waggett, Shafiq, and Bartlett, 2018).

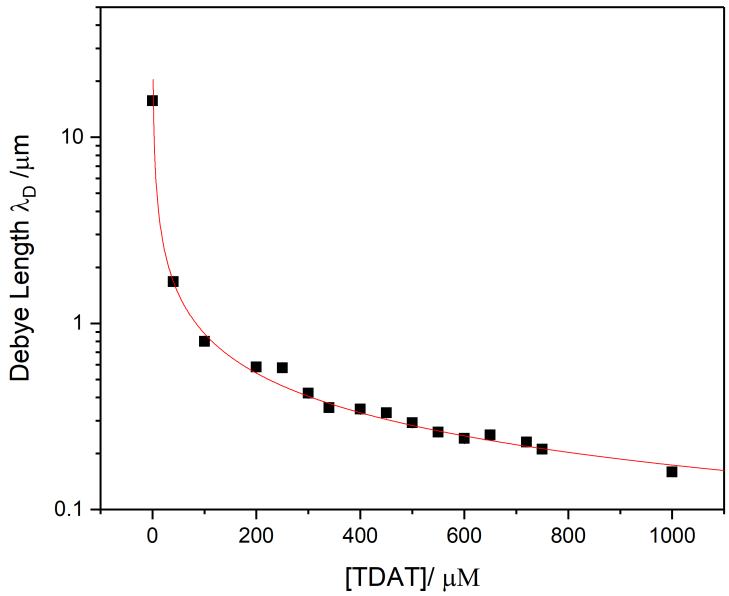

FIGURE 3.12: The Debye length calculated from conductivity and ion density changes with TDAT concentration

3.4.2 Blinking Optical Tweezers

Fundamentally, the Debye and screening lengths are two terms refer to the characteristic length from the surface charge to the point where the electrostatic potential decaying from the true (surface) potential. These two terms also measure the thickness of electric double layer of a (charged) surface and the strength of electrostatic screening. To differentiate these two terms in our work, we refer the Debye length λ_D as the theoretical screening length measured from conductivity and the screening length κ^{-1} is the measured (true) screening length fitted from $r^2F(r)$ plot using equation 3.2 resulted from the measurement of forces between two particles using BOT.

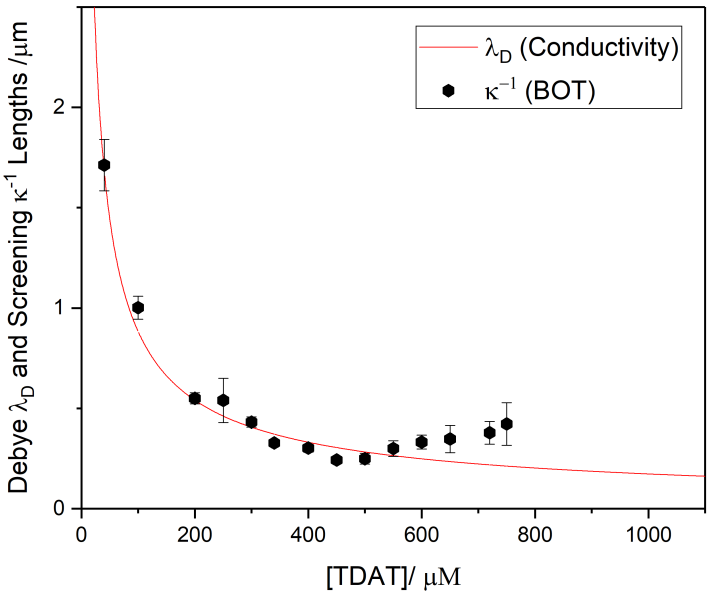

FIGURE 3.13: The disagreement between Debye and screening lengths at [TDAT] $\geqslant$ 450 μM

Figure 3.13 portrays the comparison of calculated Debye length λ_D and measured screening length κ^{-1} and the divergence is obvious at high TDAT concentrations. The unusual non-monotonic trend of the screening length is likely due to the reduced surface separation between colloids below κ^{-1}. This is mainly because of the screening length was fitted over the similar scaled separations for all TDAT concentrations ($2/\kappa \leqslant h \leqslant 4/\kappa$) (Waggett, Shafiq, and Bartlett, 2018). κ^{-1} appears to be correlated with the point where the charge regulation starts to appear and consequently the collapse of the surface charge. The increase of κ^{-1} at above 450 μM is due to the decrease of surface charge, resulting weakened force as depicted in Figure 3.14, presenting a slower decay (larger κ^{-1}). Increasing TDAT concentration enhances the dependence of the surface charge on the distance between surfaces,

resulting in a non-monotonic trend of the Debye length.

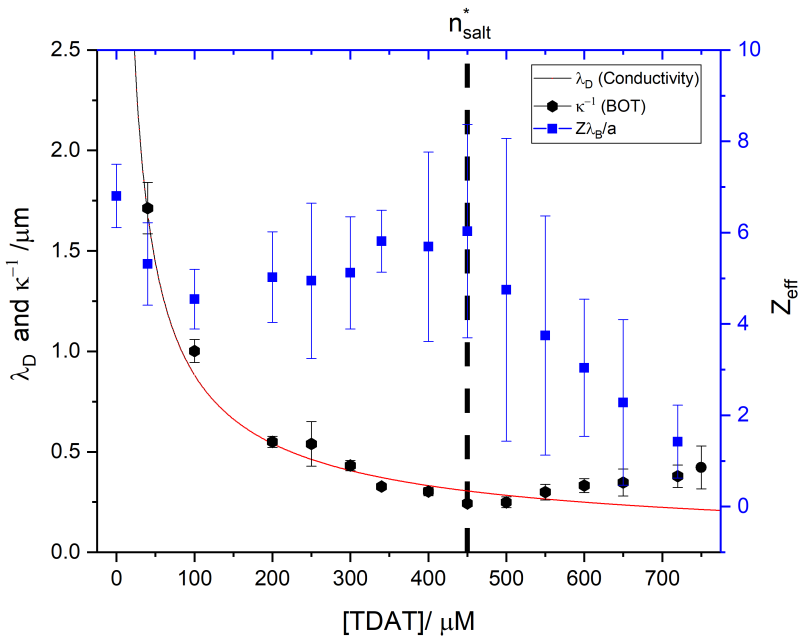

FIGURE 3.14: Combined plots of Debye, screening lengths and effective charge varied with TDAT concentration

Figure 3.14 shows combined plots of Debye, screening lengths and effective particle charge (λ_D, κ^{-1} and Z_{eff}) changes with TDAT concentration. At the critical salt concentration $n^*_{salt} \sim 450\ \mu$M, the measured screening is the lowest, and increasing TDAT concentration beyond this point length breaks the classical monotonic behaviour. This is also the onset point where Z_{eff} collapses to nearly zero charge at [TDAT] $\geqslant 700\ \mu$M. Beyond n^*_{salt}, the ions are compacted between each other in solution, thus the entropy of counterion solvation is inadequate to dissociate from the surface, resulting in discharging process (Waggett, Shafiq, and Bartlett, 2018). From this plot, below n^*_{salt}, the system is behaving like a constant surface charge (CSC) system, where the effective charge is mostly unaffected by TDAT concentration and increasing [TDAT] $\geq n^*_{salt}$, the particle surface is no longer treated as CSC system.

3.5 Discussion

Figures 3.2 and 3.3 show that the attraction between colloids induced by the addition of TDAT electrolyte in PMMA/dodecane system and the aggregate formation depend on TDAT concentration. Importantly, Figure 3.13 illustrates the unusual

non-monotonic trend of the measured screening length κ^{-1} with TDAT concentration and the dependency of effective charge on the TDAT concentration. These important experimental key results reveal clues on the possible origins and underlying theories of these phenomena.

In non-aqueous colloidal systems, the charge distribution on the particle surface is not uniform throughout. As mentioned earlier, TDAT-containing PMMA/ dodecane systems have a constant surface charge system (CSC) at [TDAT] $\leqslant$ 450 μM where the charge is independent of TDAT concentration and beyond [TDAT] $\sim$ 450 μM, the charge decreases with [TDAT] and CSC boundary condition is no longer valid. This shows that this system behaves as a charge regulation (CR) model where the surface charge changes adapting to the surrounding ions near the particle surface. The CR model was derived for aqueous biocolloidal systems where the surface charge varies with the ionization of surface groups; the acid-base equilibria (Bowen and Williams, 1996). The interactions in the double layer between charged surfaces of a CR model are dissimilar from CSC surfaces. In a non-aqueous system, the degree of dissociation of surface groups is weak or negligible and the released counterions concentration depends on the surrounding environment near the surface vicinity (or between interacting surfaces) such as the number of ions and colloid volume fraction which correspond to the electrostatic potential as a function of separation distance between charged surfaces (Hallett et al., 2018). This results in the non-uniformity of the surface charge density and, repulsion between surfaces arises from the osmotic pressure driven by an overlapping of counterions in the double layer when two surfaces approaching each other becomes ineffective (Hallett et al., 2018; Ninham and Parsegian, 1971). The CR model was also widely studied in an aqueous systems and similar findings reported (Borkovec and Behrens, 2008). For a system with a simple CSC model, the surface charge does not vary erratically as the surfaces approach, but for a system with the CR limit, the electrostatic repulsion is effectively reduced, hence collapsing the surface charge. Another simple model known as the constant surface potential (CSP) limit, where the surface charge changes to maintain a fixed surface potential, happens when there is a surface adsorption of either or both counterions or/and coions (Hallett et al., 2018; Finlayson, 2016a; Roberts et al., 2008). This model is seen in non-polar colloidal systems and will be discussed in Chapter 6.

The non-uniformity of charge distribution on a weakly charged-surface drives the change in charge symmetry on the contacting area; when two similarly charged surfaces approach each other, at distances $R \sim a$, one part of the surface forms a temporary charge sign with another part forming a charge with an opposite sign, or simply temporary dipoles. This happens at high ion concentrations (TDAT

$\geqslant$ 450 μM), where ions in the solution (and near surface) influence the charge distribution on the colloid surface. In this case, the colloids are considered as having Janus particles behaviour. Janus particles are particles with asymmetric surfaces and the most common one being spherical particles with different hydrophobicity of each hemisphere. The formation of so-called charge 'patches' on each hemisphere of colloids electrostatically interacts in a Coulombic manner, where like charges repel and opposite charges attract. Hieronimus and coworkers outlined the interaction model of Janus particles and they differentiate both hemisphere into a 'north-pole' n and a 'south-pole' s, divided equally with an equator as presented in Figure 3.15. If the north pole and south pole are both arranged antiparalelly, the sum interaction of their equators is repulsive, similarly with nn and ss interactions as shown in Figure 3.16. The strength of attractive interaction is weaker with $sn >$ anti-equator $> ss >$ equator configurations. The attraction formed between these Janus particles are due to the total sum of interaction between two contrast poles (Hieronimus, Raschke, and Heuer, 2016).

FIGURE 3.15: Presentation of dipole-like formation due to non-uniform charge distribution on the surface

The short-ranged attraction between these patchy hard spheres can be expressed by the Yukawa potential with dipoles $d1$ and $d2$,

$$U(r_{d1d2}) = \frac{Z_{d1}Z_{d2}}{4\pi\epsilon r_{d1d2}} exp(-\kappa r_{d1d2}) \tag{3.13}$$

Hieronimus et al. also mentioned that the system with lower screening length tends to form aggregates of closed-packed structures and the less closely packed structures were observed in system with higher screening lengths. Aggregates formed due to the arrangement of sn dipoles are best pictured in the arrangement of four particles as depicted in Figure 3.17. The arrangement of these particles depends on the screening length of the system, with an inverse proportional relation between screening length and dipole moment $|\mu|$; system with large screening length has the lowest dipole moment, approaching to zero ($\kappa \propto |\mu|$).

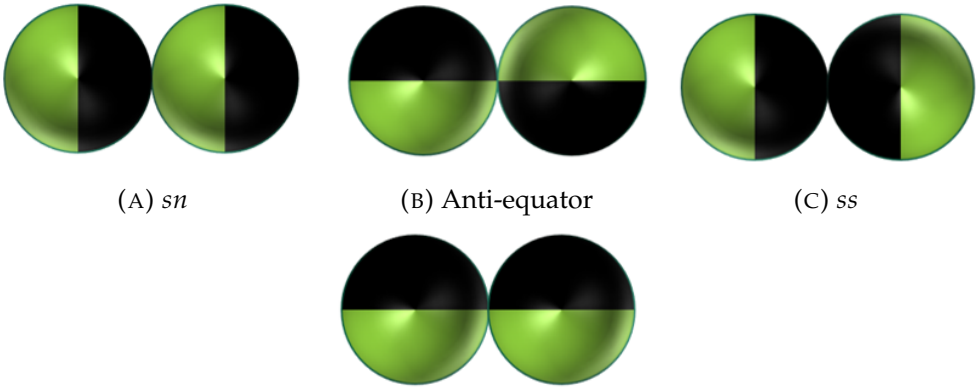

(A) *sn* (B) Anti-equator (C) *ss*

(D) Equator

FIGURE 3.16: Configurations of Janus particles-induced dipoles (Hieronimus, Raschke, and Heuer, 2016)

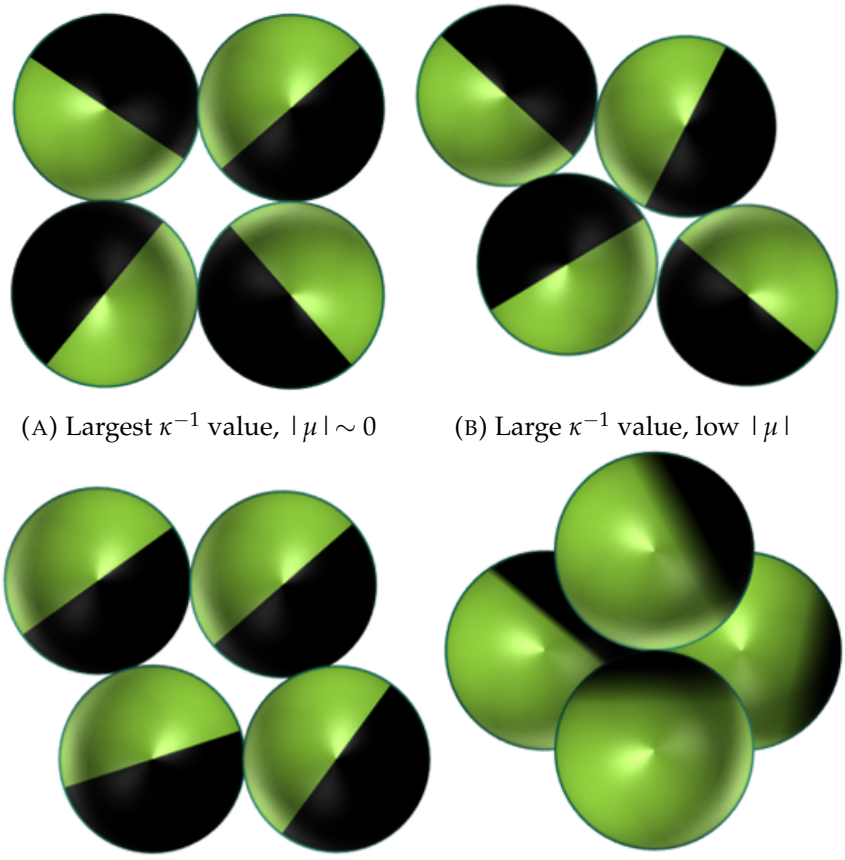

(A) Largest κ^{-1} value, $|\mu| \sim 0$ (B) Large κ^{-1} value, low $|\mu|$

(C) Intermediate κ^{-1} value, high $|\mu|$ (D) Small κ^{-1} value, highest $|\mu|$

FIGURE 3.17: Dependency of the screening length on the arrangement of Janus particles-induced dipoles (Hieronimus, Raschke, and Heuer, 2016)

As an initial experimental work to prove the formation of Janus particle-like in our system, we applied an electric field on the chain formed as a result of particles attraction. The chain was observed to rotate 90^o when an electric field was applied. The rotation was imaged using the bright-field microscope and presented

in Figure 3.18.

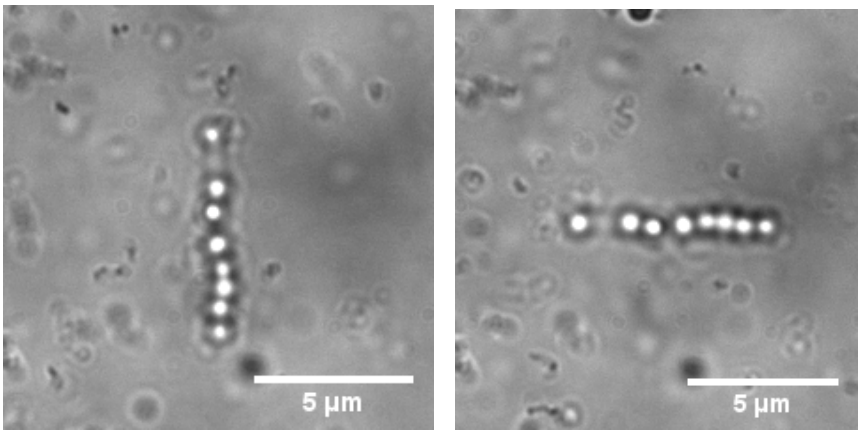

(A) No electric field applied (B) With an applied electric field

FIGURE 3.18: Chain formed due to particle attraction rotates at 90^o with an applied electric field

3.6 Disproving Theories and Other Systems

3.6.1 Bjerrum Pairs

The Bjerrum length $\lambda_B = e^2/4\pi\epsilon k_B T$ plays an important role to qualify whether a system is considered as an ionic solution or otherwise. If the Bjerrum length is comparable to the lattice spacing of the salt or electrolyte where the dissociation is favourable and the solution is considered as ionic such as NaCl solution. Oppositely charged free ions in solution can possibly recombine into dipoles which is known as Bjerrum pairs and these dipoles influence the behaviour of ionic solutions (Adar, Markovich, and Andelman, 2017).

Bjerrum dipoles have a dominant effect on the screening length. As the dipoles form, the concentration of free mobile ions in solution is reduced and the permittivity of the solvent is affected, $\kappa^{-1} \propto (\epsilon/\rho_{ion})^{1/2}$. This is why we postulate that the unusual non-monotonic behaviour of screening length of electrolytic dodecane solution as illustrated in Figure 3.13 is due to the formation of Bjerrum dipoles. Theoretically, at lower TDAT concentrations, the cations and anions exist as individual ions and as TDAT concentration was increased more that 450 μM, the addition of more ions will induce the association of oppositely-charged ions into dipoles. These dipoles do not affect the screening length as free ions do as they are uncharged. This hypothesis is accurate with literature where the surface-force experiment was conducted to investigate the screening length of ionic solution Smith, Lee, and Perkin, 2016. However, the ion concentration in our system continues to increase as depicted

in Figure 3.11 despite the measured screening length increasing at [TDAT] $\geqslant 450\ \mu$M as shown in Figure 3.13.

The Bjerrum pairs theory further justifies the experimental and theoretical aspects we observed in PMMA/dodecane with TDAT electrolyte system. The cluster and aggregate formation due to particles attraction was initially assumed to originate from depletion of the Bjerrum dipoles on the particle surface. Allahyarov et al. observed a similar attraction due to non-DLVO forces. The dipoles formed of oppositely-charged ions, fluctuate in the solvent and are less likely to correlate near the system boundary, therefore being depleted from the particle surfaces (Allahyarov et al., 2007). The mechanism is similar to the depletion interaction between colloidal surfaces, thus overcoming the electostatic repulsion. The formation of Bjerrum dipoles drastically reduces the permittivity of the solvent by increasing the Coulomb coupling between these ions. The Coulomb coupling can be quantified by $\Gamma = e^2/\epsilon r_{ion} k_B T$. High value of Γ implies that the counter and co-ions have a higher tendency to form dipoles. This pairing will lead to a critical point in the restricted primitive model (RPM) and an external force such as Casimir forces will possibly drive two colloids to attract each other, pushing these colloids close to criticality (Allahyarov et al., 2007). The critical effective temperature $T^* = 1/\Gamma$ for the RPM model is 0.05 and we calculated the value for our system, $T^* < 0.05$, so the formation of Bjerrum pairs as the origin of particle attractions is unlikely for our system (Hynninen, Dijkstra, and Panagiotopoulos, 2005).

3.6.2 Other System: Charged Particles

Figure 3.19 presents the effective charge of three different colloids in dodecane with varied TDAT concentration. The purpose of this comparison is to justify the effect of the magnitude of charge and particle properties on the dependency of TDAT concentration and the unusual trend of the screening length. The properties of colloids used for the comparison are presented in Table 3.2.

Colloid	**Diameter, $d \pm 0.05$, μm**	**Dye**
PMMA (AC12)	1.29	$DiIC_{18}$
PMMA (AC11)	1.55	-
IM6-PMMA	2.53	-

TABLE 3.2: Properties of different types of colloids

The effective charge generally does not depend on the TDAT concentration despite the magnitude of charge. IM6-PMMA particles were synthesized by Hussain et al. to generate colloid charging in non-polar solvent. We observed the discharging phenomena of PMMA (AC12) colloids when TDAT was added at more than 450 μM as explained previously. However, the effective charge of IM6-PMMA particles remains unchanged even at much higher concentration of TDAT. This initiated the idea that highly charged surfaces require more electrolyte to induce surface charge instability. However, we did not observe the charge instability regime for IM6-PMMA system. The screening length for IM6-PMMA colloids does not portray any unusual trend even at much higher TDAT concentrations ($\geqslant$ 900 μM) and κ^{-1} obeys the Debye-H*ü*ckel theory ($\kappa^{-1} \sim 1/\sqrt{\rho_{ion}}$) as depicted in Figure 3.20. On the other hand, PMMA (AC11) has a similar charge magnitude with PMMA (AC12) and we found that there was no significant difference between these two. We used AC11 to investigate the effect for particle size and dye used on the electrostatic properties, especially at very low electrolyte concentration.

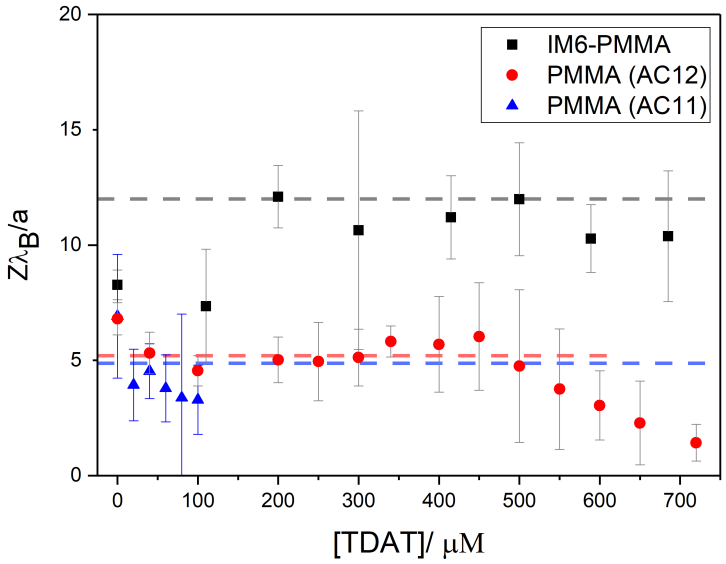

FIGURE 3.19: The comparison of effective charge of three different colloids in dodecane varied with TDAT concentration

Figure 3.21 shows the cluster formation in IM6-PMMA dodecane system with varied concentration of TDAT. Compared to Figures 3.2 and 3.3, the cluster and aggregate formation occurred at much lower TDAT concentration in PMMA(AC12) system. This proves that more electrolyte and ion concentration required to form larger aggregates in IM6-PMMA system in order to overcome the higher magnitude of electrostatic repulsion between the colloids.

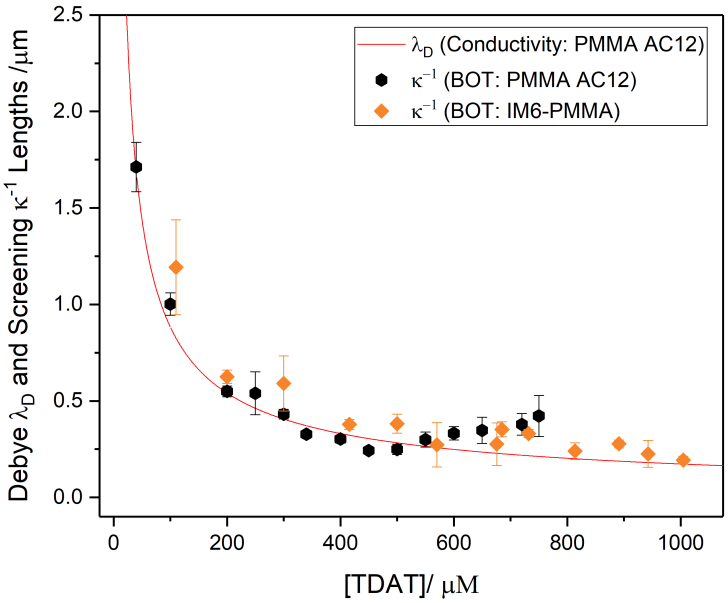

FIGURE 3.20: The screening length comparison of two different colloidal system varied with TDAT concentration

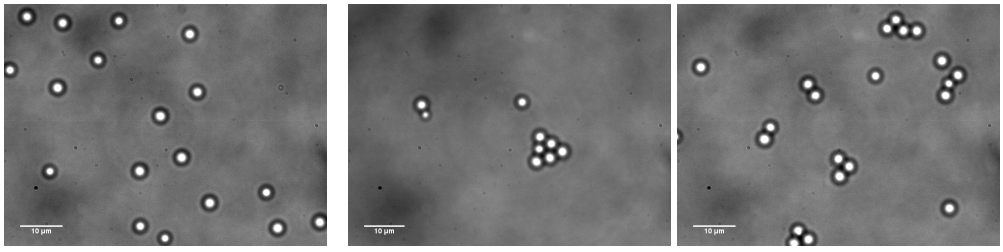

(A) 100 μM (B) 400 μM (C) 600 μM

FIGURE 3.21: Images of clusters and aggregates of IM6-PMMA colloids in dodecane varied with TDAT concentration

3.6.3 Other System: Dielectric-Matched Solvents

We used a combination of two solvents; tetrachloroethlyene (TCE) and mixed-isomer decalins to compare the aggregation behaviour of PMMA colloids induced by TDAT electrolyte. The volume fractions of TCE-Decalins system were varied to alter the dielectric constant of mixed-solvents. We predicted the attraction formed in dodecane was due to the polarization effect arises from dielectric mismatched between PMMA and dodecane. The dielectric constant of the resulting solvents were calculated using the Clausius-Mossotti Relation,

$$\frac{\epsilon_r - 1}{\epsilon_r + 2} \cdot \frac{M_w}{\rho} = \frac{4\pi N_A \alpha'}{3} \tag{3.14}$$

with ϵ_r is the dielectric constant of the resulting solvent, M_w is the molecular weight of resulting solvent, ρ is the density of mixed solvent N_A is the Avogrado's constant and α_p is the solvent polarizability.

Vol. Frac. TCE-Decalins	ϵ_r	λ_B, **nm**
0.2-0.8	2.236	25.0
0.3-0.7	2.269	24.7
0.5-0.5	2.338	23.9

TABLE 3.3: Physical Properties of TCE-Decalins system

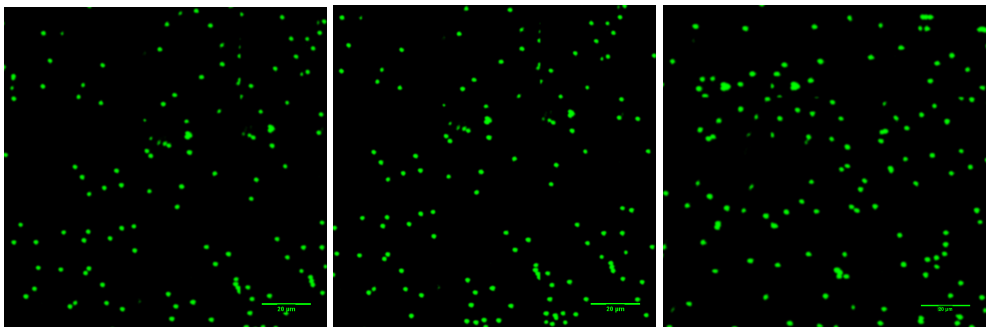

(A) 200 μM (B) 340 μM (C) 500 μM

FIGURE 3.22: Images of clusters and aggregates of PMMA colloids in TCE-Decalins 0.2-0.8 varied with TDAT concentration

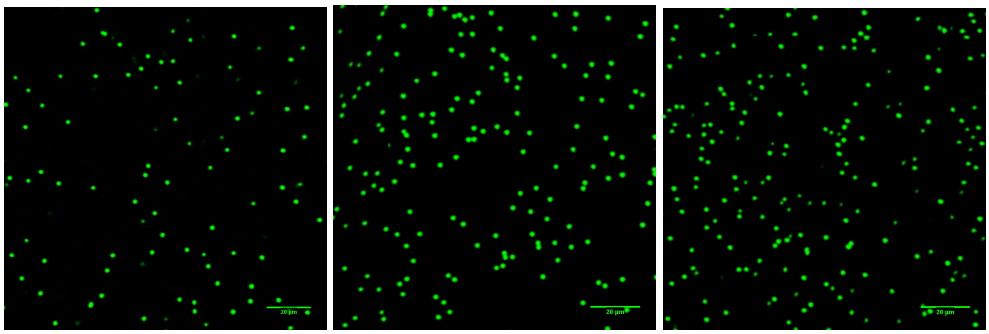

(A) 200 μM (B) 340 μM (C) 500 μM

FIGURE 3.23: Images of clusters and aggregates of PMMA colloids in TCE-Decalins 0.3-0.7 varied with TDAT concentration

The formation of large clusters or aggregates induced by TDAT electrolyte are not obviously spotted in TCE-Decalins system as presented in Figures 3.22-3.24. For TCE50 system from, the colloids seem to disperse throughout the bulk solution as we can hardly capture many colloids at one plane during the confocal microscopy imaging scanning. These observations agree with the quantitative analysis for the systems. Figure 3.25 compares the average particle diameter formed in dodecane

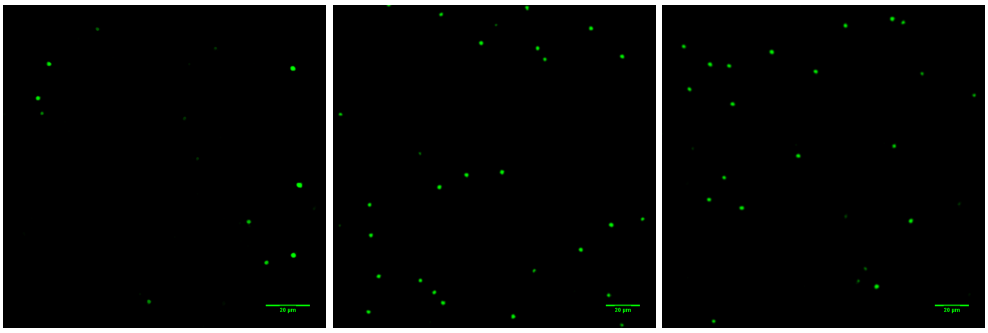

(A) 200 μM (B) 340 μM (C) 500 μM

FIGURE 3.24: Images of clusters and aggregates of PMMA colloids in TCE-Decalins 0.5-0.5 varied with TDAT concentration

and TCE-Decalins systems. Large aggregates formed in dodecane at [TDAT] $\geqslant$ 350 μM, while the onset for aggregates formation reduces with increasing volume fraction of TCE as the base solvent and the base dielectric constant of the system. We can see that at much higher TDAT concentration (up to 1.5 mM), which beyond the solubility limit of TDAT in dodecane at room temperature, the PMMA colloids in the TCE50 system were still exist as single particles, hardly forming doublets or clusters. The conductivity and Debye length plots for TCE-Decalins system are interrelated as presented in Figures 3.26 and 3.27 respectively.

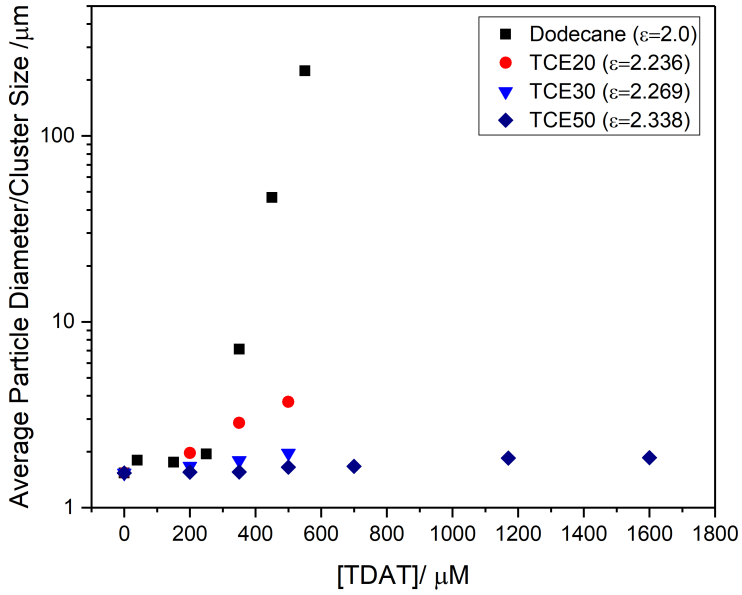

FIGURE 3.25: Average diameter of particle/clusters/aggregates of PMMA in TCE-Decalins varied with TDAT concentration

The preliminary experimental findings for these systems provide us with

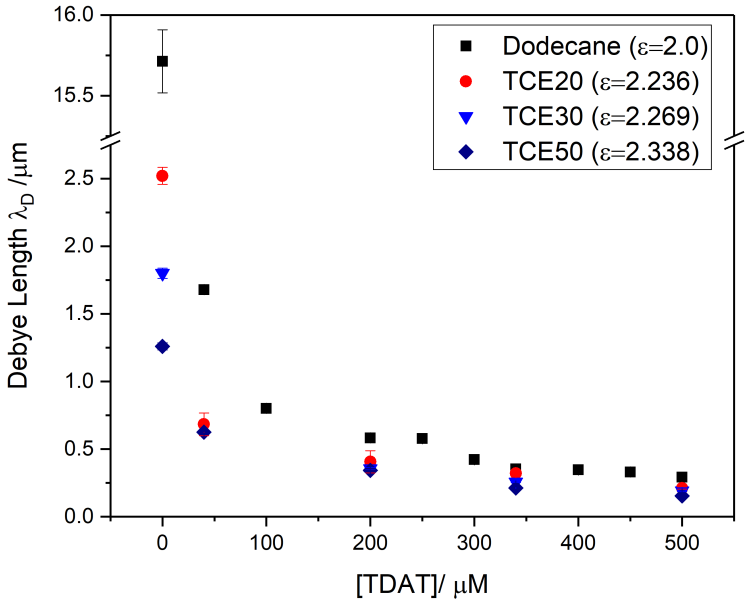

FIGURE 3.26: Conductivity of PMMA in various solvents system varied with TDAT concentration

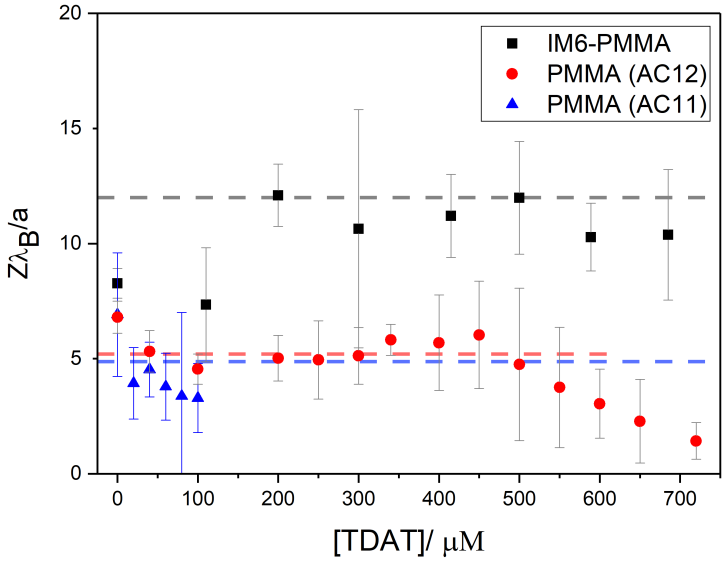

FIGURE 3.27: Debye Length of PMMA in various solvents system varied with TDAT concentration

an initial hypothesis of the effect of dielectric constant of the aggregation of particles. A significant difference of dielectrics property between colloids and solvent induced polarization charges on the surfaces of the solutes. The dielectric constant for dodecane is 2 and PMMA is about 4.9 (Thomas, Ravindran, and Varma, 2012). Altering the volume fraction of the solvent will reduce the tendency of dielectrics

mismatched between PMMA and the solvent. In a theoretical study performed by Luijten and Barrros, the self-assembly of colloids can be modified from dielectric interaction and a string-like particle chain is formed due to dielectric interactions of many bodies, justfying this interaction that does not only bind colloidal pair (Barros and Luijten, 2014). Given the reduced dielectric constant known as $\bar{\epsilon} = \epsilon_c/\epsilon_m$ where ϵ_c is the dielectric constant of colloid and ϵ_m is the dielectric constant of dispersing medium. If $\bar{\epsilon} < 1$, the dielectric effect is repulsive and $\bar{\epsilon} > 1$, the induced bound charge on the surface has the opposite sign (image charge or mirror charge) as of the surface, thus attraction is seen (Barros and Luijten, 2014; Lindell, 1992). For $\bar{\epsilon} < 1$, where the particle is more polarizable than the solvent, the solvent acts as the capacitance, accumulating charge on the interface and the particle acts as a conductor, meaning the Coulombic interaction between these particles are dependant on the amount of charge stored at the interface (Dong, 2009).

3.7 Summary

The main key points for this experiment are the particle attraction and inflation of screening length κ^{-1} observed induced by TDAT electrolyte at high concentrations and how these affect the deposition patterns of evaporating colloidal droplets. Increasing TDAT concentration effectively enhance the particle attraction, where large clusters and aggregates were observed. Quantitatively, the average number of particle formed in one aggregate is $N_{ave} \sim 1000$ at [TDAT] $\geqslant 450$ μM and the value increases up to 2-3 order of magnitude with increasing [TDAT] up to ~ 600 μM. From the force measurement between two PMMA colloids, it is found that the long-range interaction becomes much shorter range with increasing [TDAT] and this explains the formation of large PMMA aggregates in dodecane. Calculated from the force measurement, the effective charge of the system shows that the instability of charge with TDAT concentration, where a tiny charge reduction with [TDAT] initially observed and regained at intermediate [TDAT]. Basically, the effective charge is unaffected by the [TDAT] at below 450 μM, suggesting the system has a constant surface charge (CSC) model. However, beyond 450 μM, the charge collapsed to nearly the point of zero charges at [TDAT] ~ 720 μM. This suggests that the PMMA colloids system with TDAT electrolyte adapts a charge regulation (CR) model.

Meanwhile, the measured screening length from BOT κ^{-1} and theoretical Debye length λ_D from the measured conductivity values show a disagreement at [TDAT] > 450 μM, which deviated from the classical Debye-Hückel theory. We discussed a number of possible theories underlying these observations such as the fluctuations of Bjerrum dipole pairs and density and dielectric-matching issues, but none of these limits matches our finding. We also outlined the Kirkwood-Schumaker

charge fluctuation interaction and strong coupling interaction but these were not discussed in this Chapter, instead, we will provide a brief summary in Chapter 6, where we will discuss these possible interactions affecting the deposition patterns of the evaporation colloidal droplets.

We have preliminarily studied the formation of Janus-like particles where temporary dipoles form on the charge colloidal surface, arising from non-uniform charge distribution and charge regulation model of this system. This phenomenon fundamentally agrees with our current findings as we have applied an electric field to observe the rotation of particle chain induced by formation of dipoles.

Chapter 4

Interactions between Charged Colloids Dispersed in Ionic Liquids

This chapter reports on a fundamental study of colloidal particles in an ionic liquid solution. Initially, the colloidal system used in this chapter was a follow-up study from the electrolytic system discussed in Chapter 3. As we will reveal the main results of the work, namely the colloidal stabilization and screening length, the experimental findings are not comparable and contrastingly different with the electrolytic colloidal system.

4.1 Introduction

Solvents are generally subdivided into three main categories. The first is molecular solvents; made up of neutral molecules such as hydrocarbon-based solvents, heptane and hexane. Secondly, the partially ionized or polar solvents; where large dipole moments induced by the large difference in electronegativity of the atoms in a molecule such as water. The third category known as the completely ionized solvent is referred as ionic liquids (Wellens, 2014; Freemantle, 2010). Ionic liquids (ILs) are salts which present are liquid at temperature below 100 ^{o}C (referred as a room temperature ionic liquid, RTIL) and also commonly known as tunable solvents. Typically, ILs are fluids with abundant free ions. ILs usually consist of organic cations and inorganic anions, and possess outstanding properties including inflammability, negligible vapour pressure and high thermal stability, therefore ILs do not evaporate under normal conditions (Freemantle, 2010; Gebbie et al., 2013). ILs are generally referred as a 'tunable solvents' as the properties of the ionic liquid can be engineered through the variety of aromatic and aliphatic cationic and anionic substituents to tailor specific applications. The selection of cations has an impact on the stability of the ILs whilst anion is normally defined by the functionality of the molten salt (Harada

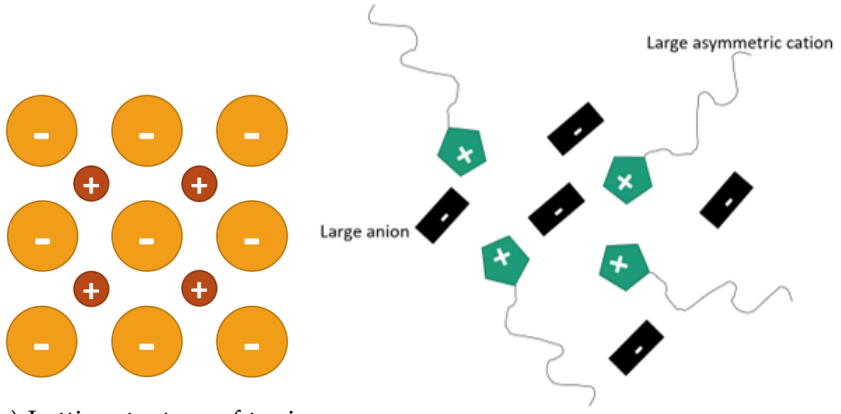

(A) Lattice stucture of typical inorganic

(B) Domain configuration of ionic liquid

FIGURE 4.1: Organization of ions in inorganic salt and ionic liquid

et al., 2018). ILs are in demand in a variety of applications including the role of electrolyte in batteries, solar cells and fuel cells also as lubricants and heat-transfer fluids (Freemantle, 2010; Gebbie et al., 2013; Wang et al., 2004; Zhang, Wu, and Mu, 2017). ILs also are mainly used to replace many conventional materials due to their potential to enhance catalytic reactions and to reduce associated risk and hazard due to the volatility and high flammability of organic compounds.

Interesting properties and versatility of ILs are mainly due to their properties, which lie in between the crystalline solid and liquid. Their liquid crystalline behaviour originates from the formation of domains; consist of coulombic and van der Waals layers. In the coulombic layer (hydrophilic domain), the ionic head groups interact with the counterions while the vdW layers are built from antiparallel stacking of alkyl chains (hydrophobic domain) (Binnemans, 2005; Kölle and Dronskowski, 2004). Due to the formation of these domains, ILs are asymmetric and relatively large than any other conventional salt as schematically presented in Figure 4.1. Furthermore, the strength of electrostatic interaction determines the important properties of the ILs as mentioned earlier. ILs have polyatomic ions with the atomic radii approximately 5 to 10 times larger than the conventional monoatomic salt such as Li^+ and K^+ (Gebbie et al., 2017). Due to the large size of IL ions, the centre-to-centre separation between cations and anions is relatively large as well, lowering the strength of electrostatic interactions of the hydrophilic domains. The hydrophobic domain, which is composed of long alkyl chains in both cations and anions results in a significant configurational and conformational entropy in ionic liquids. These characteristics contribute to the low melting point and glass transition temperature T_g of ionic liquids (Gebbie et al., 2017; Yamamuro et al., 2006).

As ILs are mainly composed of ions, they possess a very high ionic strength, with the conductivity approximately nine oreder of magnitude higher than a conventional organic liquid ($\sim 10^{-12}$ Scm^{-1}). The theoretical free ions abundance in

ion liquid gain interest and attention from colloidal scientists to investigate the behaviour of colloidal systems in an ionic liquid. The unique properties of the ILs, mainly related to the interactions of colloidal particles such as viscosity and ionic conductivity, give a number of alternative to explore the stabilization of colloidal systems in ionic liquids. The large amount of free ions in ionic liquid fundamentally affects the thickness of the electric double layer (EDL) and screens electrostatics between charged colloids according to the classical Derjaguin, Verwey, Landau and Overbeek (DLVO) theory, thus having a short Debye length (Gebbie et al., 2013; Gebbie et al., 2017; Masliyah and Bhattacharjee, 2006). Many studies on the electrostatic interactions in ionic liquid consider simple DLVO theory but the concentrated amount of ions in ionic liquid does not featured in most conventional (organic and aqueous) solvents, thus the explanation on the electrostatic interactions and screening of the IL system can be complex. However, in a recent study investigating the force between mica surfaces in a pure ionic liquid system, the AFM reveals that the long-ranged interactions between mica surfaces are electrostatic in origin implying that the ionic liquid behaves similarly to dilute (1:1) electrolytic solution, indicating that the Debye length of the IL system is on the order of the ionic radii (Gebbie et al., 2013). This justifies that the electrostatic force between charged colloids in an ionic liquid is not a unique feature of the system, although the argument remains the subject of debate and the origin of long-ranged forces is still puzzling.

Electrostatic stabilization of colloids in an ionic liquid can be difficult due to the presence of a large amount of ions in solution. Therefore an extensive study was performed on the colloidal cluster and domain formation in an ionic liquid solution. Based on classical DLVO theory, the destabilization of colloidal system is driven by the van der Waals (vdW) attraction and the electrostatic screening effect induced in an ionic liquid solution is large and electrostatics is not able to counterbalance the vdW force. However in our system, the PMMA particles are surrounded by a 10 nm polyhydroxystearic acid (PHSA) layer. As widely used, the PHSA layer entropically repel the particles from aggregating when they come into contact, thus stabilizing the system. The stabilization of colloids is not only limited by electrostatic means but also via solvation and steric stabilization. The solvation stabilization can be considered as an alternative mechanism of colloidal stabilization for ionic liquid systems as the structuring of ionic liquids between two colloids results in the repulsive solvation force due to the disruption of ordering structure in a confinement (Perkin, 2012; Ueno and Watanabe, 2011).

In this chapter, we discuss the effect of the ionic liquid on the long range interaction between poly(methyl methacrylate) (PMMA) particles, where the Debye screening length is small and the number of ions present in bulk system are large. Further study is needed to explain the influence of ionic liquid on the surface charge of the PMMA particles, where the cations and anions structure near the charged surface. Corresponding to the electrostatic screening effect in an ionic liquid solution,

we will discuss on the effect of ionic liquid on the colloidal clustering and aggregation. The underlying issues addressed in this chapter can be compared with our findings in the electrolytic non-aqueous system discussed in Chapter 3.

4.2 Experimental

PMMA colloids were synthesized by Dr. Andrew Campbell using the synthesis procedure outlined in Chapter 2. The volume fraction ϕ of PMMA $\sim 10^{-4}$ was used throughout this experiment. Dodecane was used as the main carrying solvent and an ionic liquid, trihexyl(tetradecyl)phosphonium bis-2,4,4-(tri methylpentyl)phosphinate (referred as Cyphos IL-104 or IL) was gradually added to relatively increase the ion concentration of the colloidal system. IL was added at concentrations of 0.5 wt.% up to 75 wt.%. Due to the limitations of experimental equipment and accuracy resulting from high the viscosity of the IL, we were unable to carry out the experiment in 100 wt.% of IL. The viscosity of the systems containing a mixture of dodecane and IL is tabulated in Table 4.1.

Dodecane, wt.%	**Cyphos IL-104, wt.%**	ρ, **g/mL**	η, **mPa.s**	ϵ
100	-	0.75	1.36	2
95	5	0.755	2.45	2.51
90	10	0.76	4	2.99
85	15	0.765	6.1	3.59
75	25	0.775	12.3	4.32
50	50	0.8	43	6.37
25	75	0.825	104	8.5

TABLE 4.1: Physical properties of the base solvents

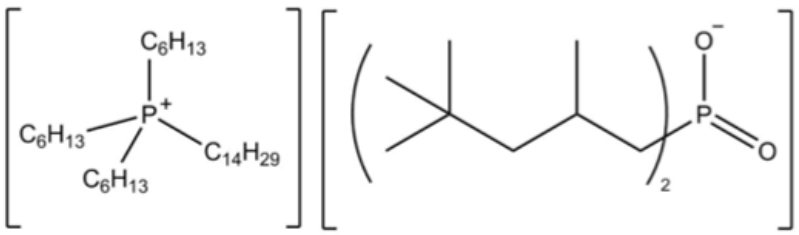

FIGURE 4.2: Molecular structure of Cyphos IL-104

Dodecane was purchased from Alfa Aesar, and Cyphos IL-104 was purchased from Merck. All solvents were dried prior usage to eliminate residual water content. The conductivity of each system was measured using conductivity meter

Scientifica model 627 and the colloidal behaviour in the bulk was observed using the confocal microscope. The effective particle charge was calculated from measured electrophoretic mobility using phase analysis light scattering (PALS) outlined in Chapter 2.

4.3 Particle Attraction: Turbidity and Confocal Microscopy Imaging

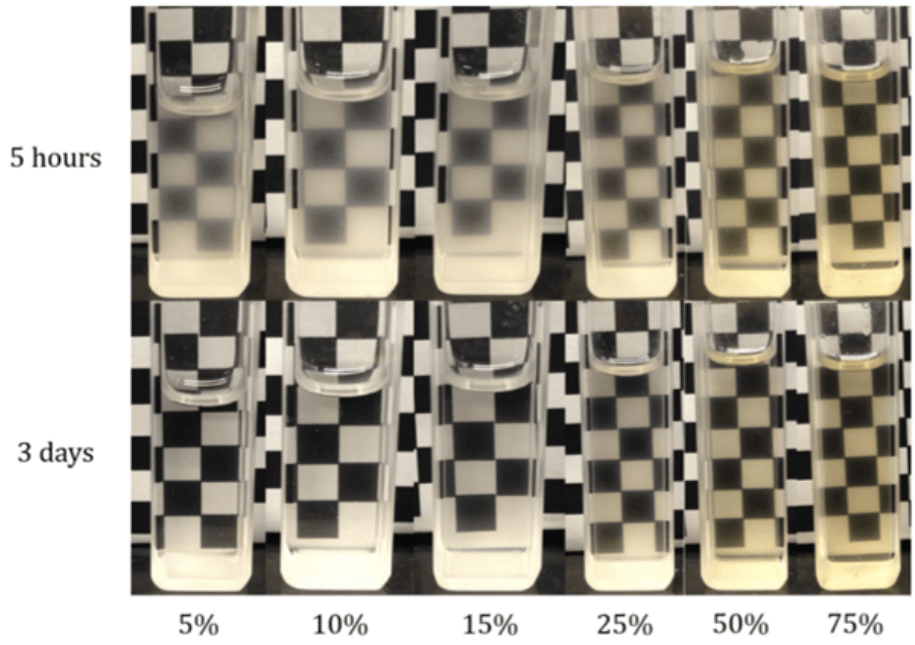

FIGURE 4.3: Optical turbidity of PMMA/dodecane-IL solution with increasing weight fraction of Cyphos IL-104

Figure 4.3 shows the turbidity of PMMA/dodecane/IL solutionS with increasing weight fraction of Cyphos IL-104, changes with time. The turbidity of the solution preliminarily indicates the stability of PMMA particles in IL solution. The solution became less turbid with time and much quickly with increasing concentration of Cyphos IL-104. This indicates that PMMA particles destabilize with increasing IL concentration. However, with increasing Cyphos IL-104 content, the solution becomes brownish and more viscous due to the nature of the IL. Figure 4.4 illustrates the behaviour of PMMA particles in dodecane and Cyphos IL-104 with increasing concentration of IL. The formation of clusters and aggregates was obviously spotted even though IL was added at a very low concentration $\sim$ 0.5 wt.% and the size and number of clusters and aggregates become more apparent with increasing concentartion of IL. However, the size of aggregates formed in PMMA/dodecane-IL solution is not comparable with the PMMA/dodecane system with TDAT electrolyte as discussed in Chapter 3.

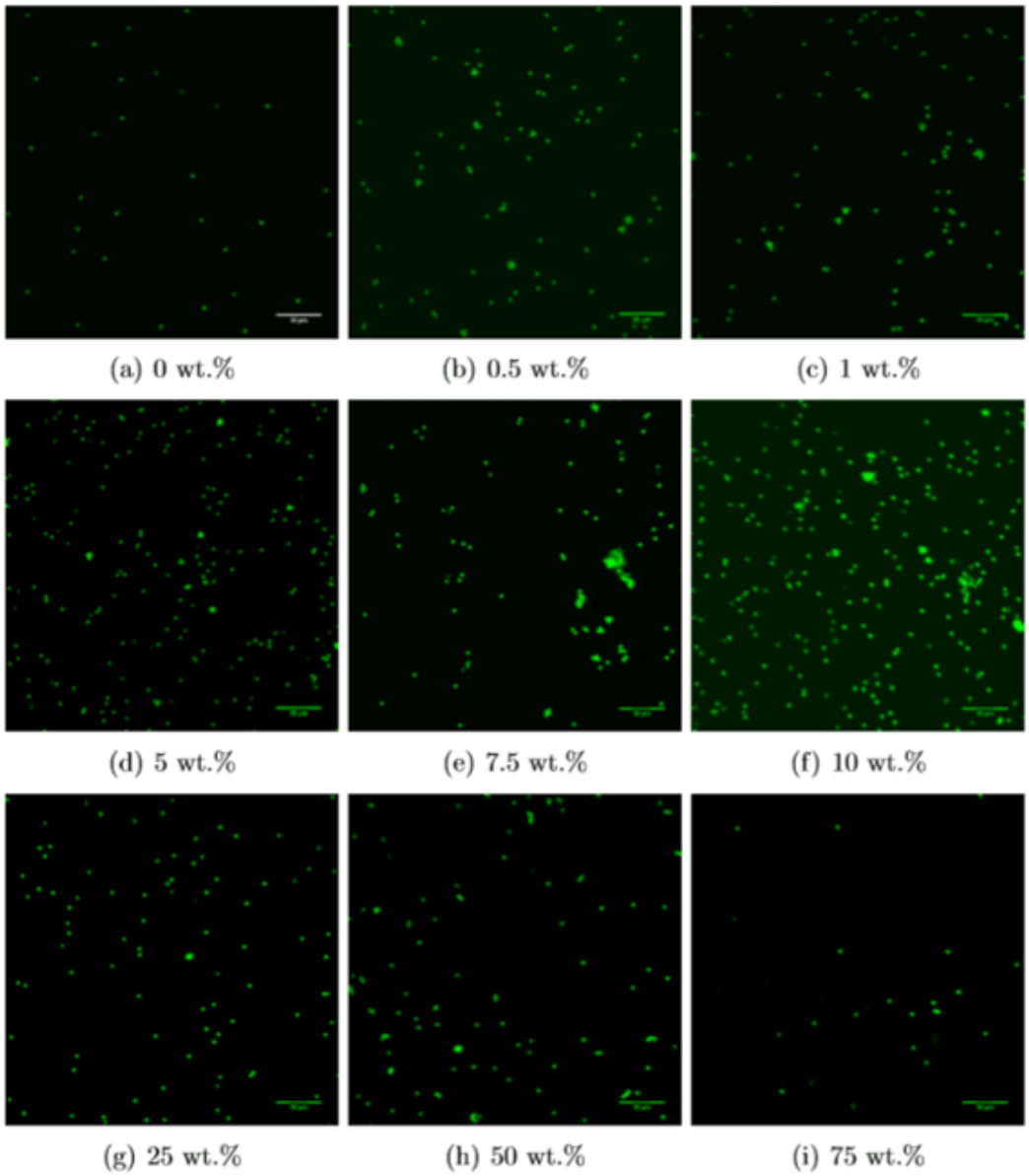

FIGURE 4.4: Formation of clusters and aggregates of PMMA colloids in dodecane varied with Cyphos IL-104 concentration

Referring to Figure 4.4, without any IL, PMMA particles exist as single particles, evenly distributed throughout the solvent. Increasing the concentration of Cyphos IL-104, only at 0.5 wt. % triggered the formation of clusters of PMMA particles. This suggests that IL induced an attraction between PMMA colloids and, the clustering and aggregation were more prone to occur with increasing Cyphos IL-104 concentration, where the largest aggregates observed in the IL solutions with 7.5-10 wt. % of Cyphos IL-104. However, when the Cyphos IL-104 concentration was further increased, the clustering and aggregation of PMMA colloids were lessly observed. Instead, the particles exist as singlets and doublets in IL solution with 75 wt. % of Cyphos IL-104, suggesting colloidal stabilization was achieved. Figure 4.6

quantitatively justifies the average cluster and aggregate size of PMMA in IL solution with increasing Cyphos IL-104 concentration. The average size increases with Cyphos IL-104 concentration initially and reached the maximum value at [Cyphos IL-104] $\sim$ 10 wt. %. The average size decreases with IL concentration after this point and plateaued when Cyphos IL-104 was added at up to 75 wt. %. This agrees with the images captured using the confocal microscope presented in Figure 4.4. The largest average size of the aggregate formed in IL solution is not comparable to the TDAT-electrolytic dodecane system (Chapter 3), where at highest TDAT concentration, the average number of particles in an aggregate is $\sim$ 100000 while the largest average cluster size for IL solution was $\sim$ 6 μm, equivalent to only $\sim$ 4 PMMA particles clustered together.

In a simple electrolytic aqueous system, particle aggregation is driven by the van der Waals interaction and the screening of double layer forces induce fast aggregation. The particle aggregation rate of IL-based solution is slowed down due to the enhanced viscosity of the based solvent. This mechanism is referred as viscous stabilization.

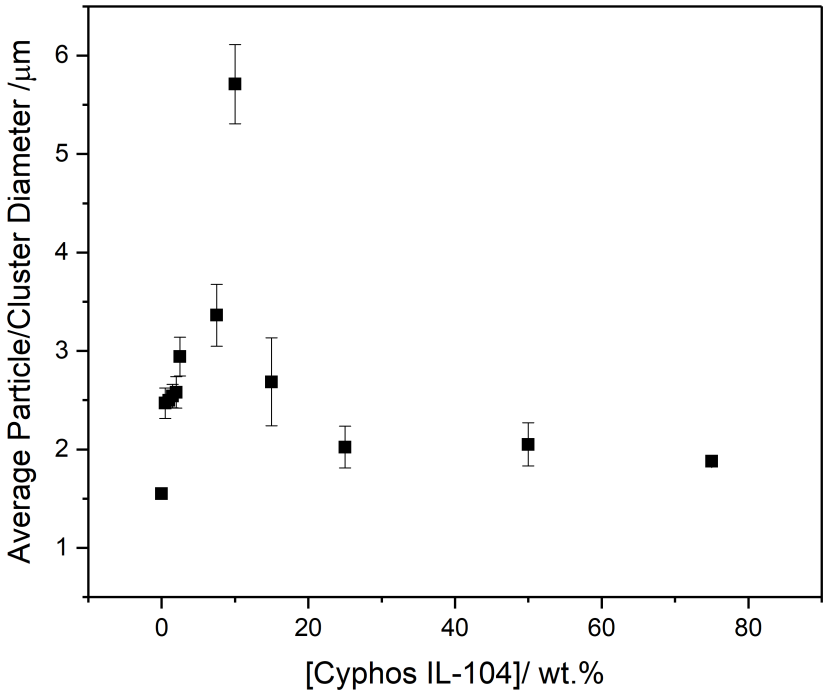

FIGURE 4.5: Average size of particle/clusters/aggregates of PMMA in dodecane varied with Cyphos IL-104 concentration

Theoretically, for [Cyphos IL-104] $>$ 10 wt. %, the calculated Debye length falls within the Smoluchowski approach ($\kappa a >> 1$). For the case of fast aggregation, which is normally valid in aqueous system, the diffusing colloids adhere among

each other rather than interacting between each other on each encounter (Russel et al., 1991). The rate coefficient k_s for fast aggregation or diffusion-controlled reaction kinetics is given by (Elimelech, Gregory, and Jia, 2013),

$$k_s = 16\pi Dr = \frac{8k_BT}{3\eta} \tag{4.1}$$

where D is the diffusion coefficient of aggregating particles ($D = k_BT/6\pi\eta a$). The value of k_s for water is 1.23 x 10^{-17} m^3s^{-1} at T= 298.15 K and η = 0.89cP. We calculate the value of k_s for our IL solution within $\kappa a >> 1$, for 15 wt. % of Cyphos IL-104, the k_s is 1.79 x 10^{-18} m^3s^{-1} and the value decreases with Cyphos IL-104 concentration with k_s = 1.05 x 10^{-19} m^3s^{-1} at [Cyphos IL-104] = 75 wt. %. This suggests that the clustering and aggregation of PMMA observed at [Cyphos IL-104] $<$ 10 wt. % originated from the ion clustering on the particle surface and colloidal stabilization achieved at [Cyphos IL-104] $>$ 10 wt. % was primarily due to the viscous stabilization (Szilagyi et al., 2014).

At low [IL] regime, the classical DLVO theory can be used to describe the interaction of colloidal particles where the electrostatic interactions were screened with increasing ion concentration in the system. At higher [IL] regime, from our calculation, the $\kappa a >> 1$ and colloidal stability is achieved. The aggregation rate decreases gradually as the viscosity of the based solvent increases and the diffusion of the aggregating particle is controlled by the viscosity of the system, thus lowering the aggregation kinetics.

4.4 The Electrostatic Screening Effect in Ionic Liquid Solution

The ionic liquid is a fluid of free ions but from the recent study and findings we gathered from our experiment, the ionic liquid behaves like a dilute electrolyte. The calculated Debye length for the pure ionic liquid or most concentrated IL solution is $\lambda_D \sim 10$ nm, which corresponds to a low concentration of free charges. Most recent studies reported that the majority of cations and anions exist as ion pairs (dipoles), thus yielding less true free ions in solution. Lee at al. (2014) suggested that the ion pair dissociation constant k must be large and the equilibrium constant can be estimated by (Lee et al., 2014),

$$k = \exp\left[\frac{\Delta E_d}{\epsilon_t k_B T}\right] \tag{4.2}$$

where ΔE_d is the dissociation energy of the ion pair and ϵ_t is the true dielectric constant. The dissociation energy can be calculated using $\Delta E_d = (E_{cation} + E_{anion}) - E_{ionpair}$ and the estimated value for ΔE_d for an Imidazolium-based ionic liquids is 300-400 kJmol^{-1} (Hunt, Gould, and Kirchner, 2007). Comparing the value of k with the dissociation constant of conventional salt in water, the k of ion-pair in ionic liquid is larger by at least one order of magnitude than any typical salt in water. However the estimation is valid when the concentration of free ions is very low as it is implied that the thermal energy dominating the interaction energy of between bound ions on the surface with the free ions in the bulk (Hill, 1949).

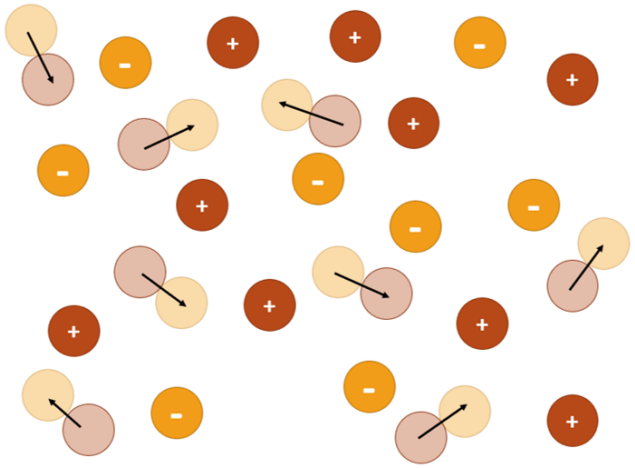

FIGURE 4.6: Schematic of ionic liquid system consisting of free ions and bound ion pairs (dipoles)

Lee and coworkers described that the interactions between ions in an ionic liquid solution screened by other free mobile charges in the bulk and the true dielectric constant of the solvent. Simultaneously, the dipoles formed in the solution correlating each other and the interaction is screened by other dipoles and free ions in the solution (Lee et al., 2014). The chemical equilibrium between free ions and pair dipoles can be written as:

$$\text{cation} + \text{anion} \rightleftharpoons \text{cation-anion} \tag{4.3}$$

and the law of mass action yields the equilibrium constant,

$$k = \frac{\rho_{dipole}}{\rho_+ \rho_-} = 2\frac{(1-\alpha)}{\rho_t \alpha^2} \tag{4.4}$$

where ρ_{dipole}, ρ_+, ρ_+ and ρ_t are the number density of dipoles, cation, anion and total species (dipoles and free ions) respectively. The fraction of dissociated cation and anion is known as α and $\alpha << 1$ for dilute electrolytes. The interaction

between colloids in ionic liquid is based on the linearized Poisson-Boltzmann theory as discussed in Chapter 1. The formation of dipoles effectively influence the dielectric constant of the base solvent as the sea of dipoles is considered as a dipolar fluid in bulk. The fluid contains polarizable species with dipole moment $|\mu|$ and the interactions between these dipoles are screened by the present mobile free charges (Lee et al., 2014; Schröer, 2001). The screening of electrostatics between surfaces in an ionic fluid by mobile free ions can be calculated using the expression,

$$\lambda_D = \frac{1}{\sqrt{4\pi\lambda_B(\rho_+ + \rho_-)}} \tag{4.5}$$

and the Bjerrum length λ_B is the characteristic length scale that measures the interaction between two point of charges with respect to the thermal energy k_BT, can be expressed as,

$$\lambda_B = \frac{e^2}{4\pi\epsilon\epsilon_o k_B T} \tag{4.6}$$

To quantify the number density of free ions in solution, we measured the conductivity of the IL solution. Figure 4.7 shows the dependency of conductivity K of ionic liquid solution on the concentration of Cyphos IL-104. It is shown that the conductivity increases with Cyphos IL-104 concentration. The conductivity increases by approximately five orders of magnitude when the IL concentration was increased from 10 to 25 wt.%. The magnitude of ion density in solution can be directly calculated from measured conductivity using the expressions 4.7 and 4.8,

$$K = (\frac{\rho_+}{N_A})\Lambda_+ + (\frac{\rho_-}{N_A})\Lambda_- + K_o \tag{4.7}$$

$$\rho_+ + \rho_- = \rho_{ion} \tag{4.8}$$

From equation 4.7, $K \propto \rho_{ion}$ and Figure 4.8 illustrates the dependency of ion density of the IL solution with Cyphos IL-104 concentration. High conductivity values of IL solution in Figure 4.7 can be directly correlated with the large number of ions present in IL solution, as IL is primarily composed of ions, thus increasing IL concentration will enhance the ion density in the solution. At room temperature, the ILs are expected to yield effective free ions at concentrations of 50-80 % of the total ion density (Tokuda et al., 2006). In theory, IL can be a good conductor but the conductivity is only comparable to an electrolytic non-aqueous solution, which is much lower than aqueous systems. So the ion density in an ionic liquid solution is still below the aqueous system due to ion pairings in the solvent, which results

in enhanced ion size and reduced mobility (Papancea, Patachia, and Porzsolt, 2015). The conductivity of purified water is $\sim 5\ \mu\text{Sm}^{-1}$ (Light et al., 2005) and from our data, for IL solution with [Cyphos IL-104] < 10 wt. %, the conductivity values were lower than conductivity of purified water but beyond this point, the conductivity increased and surpassed the conductivity of pure water, having $\sim 0.52\ \text{mSm}^{-1}$ at 75 wt. % of Cyphos IL-104. The conductivity of an electrolytic aqueous KOH (35 wt.%) solution at room temperature is $K \sim 0.5\ \text{mSm}^{-1}$ and this suggests that at [Cyphos IL-104] > 10 wt. %, the ion density in IL solution is similar to an electrolytic aqueous solution (Allebrod et al., 2012; Yushkevich, Maksimova, and Bullan, 1967).

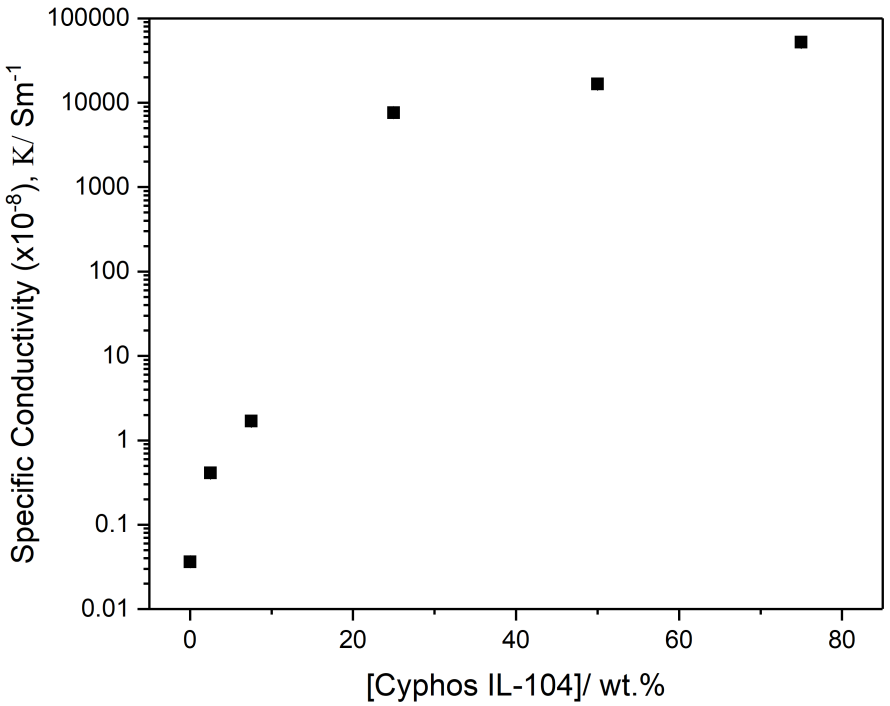

FIGURE 4.7: Conductivity of ionic liquid solution changes with Cyphos IL-104 concentration

The Debye length of ionic solution changes with Cyphos IL-104 concentration is presented in Figure 4.9. It shows that the electrostatic interaction between PMMA colloids was heavily screened when IL was added into the PMMA/dodecane solution. The expected monotonic exponential decay of the Debye length of ionic solution justifies the vast number density of ions in the solution with increasing IL concentration ($\lambda_D \propto (\sqrt{\rho_{ion}})^{-1}$).

Figure 4.10 compares the Debye length (calculated from conductivity) and

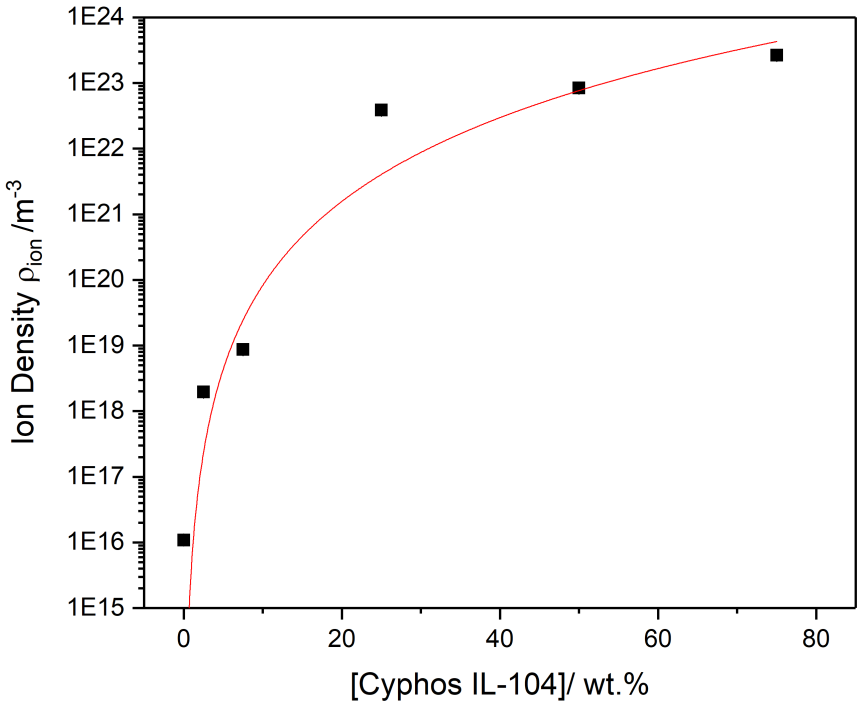

FIGURE 4.8: Ion density of ionic liquid solution changes with Cyphos IL-104 concentration

the screening length (measured from BOT) of the IL solution with varied Cyphos IL-104 concentration. We were unable to measure the screening length at high IL concentrations using the blinking optical tweezers due to experimental restrictions resulted from the viscosity of the system. Comparing these two characteristic lengths, both values agree with the classical Debye-H*ü*ckel theory. Gebbie and coworkers performed an investigation on electrostatics of ionic liquids and reported the similar behaviour. They suggested that the screening of electrostatic interactions between colloids in an ionic liquid solution resulted from the thickness of the double (stern and diffuse) layers, where most dissociated ions in ionic liquid occupy within these layers (Gebbie et al., 2013). Referring back to Figure 4.4 where we observed the clustering of PMMA in IL solution, this is mainly due to the effective short range interactions between the surfaces induced by ion structuring on the surface (Gebbie et al., 2013). However, the colloidal stabilization is achieved for the systems with very high Cyphos IL-104 concentrations as depicted in Figure 4.4. This observation opposes classical DLVO theory as an increment of ion concentration in a solution will effectively screen the electrostatic interactions between colloids (Gebbie et al., 2013; Szilagyi et al., 2014).

The changes in dielectric constants (base and true) of the system largely influenced the Bjerrum length, which corresponds to the Debye length of the ionic

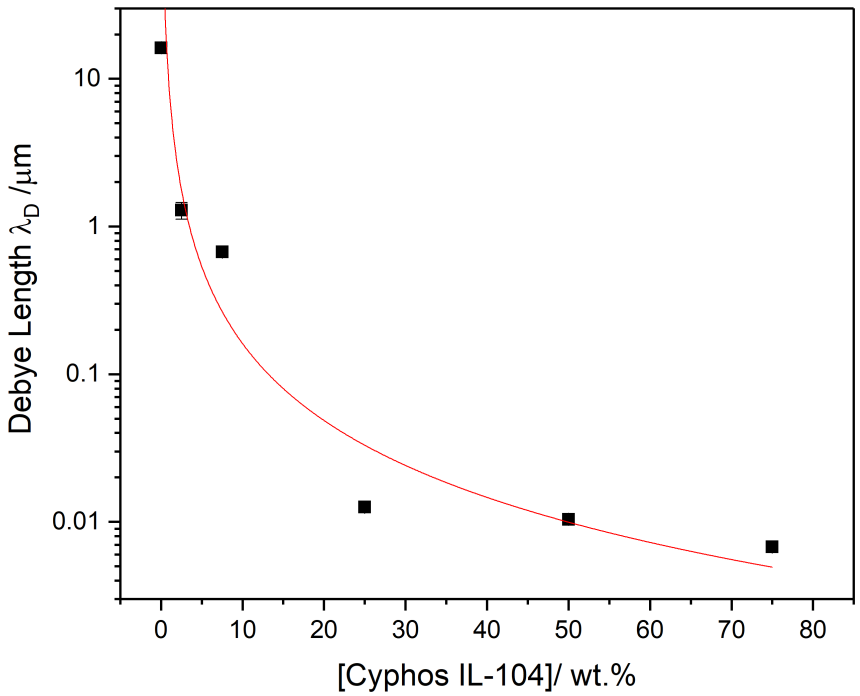

FIGURE 4.9: Debye length of ionic liquid solution changes with Cyphos IL-104 concentration

liquid solution ($\lambda_D \sim \sqrt{\epsilon_t}$). The dielectric constant of the ionic solutions presented in Table 6.1 were calculated using the Clausius-Mosetti equation (base dielectric constant), which only considers the polarizability of the molecules but not the fraction of ion pairs to the individual free ions in solution. Considering the mean-field treatment of interaction between dipoles and linearized Poisson-Boltzmann approximation, the true dielectric constant ϵ_{true} changes with the fraction of associated ion pair forming dipoles can be calculated using (Lee et al., 2014; Schröer, 2001; Masliyah and Bhattacharjee, 2006),

$$\epsilon_t = \frac{(1-\alpha)\rho_T|\mu|^2}{18\epsilon_o k_B T} \tag{4.9}$$

Lee and coworkers revealed that at $\kappa a >> 1$, $\alpha \sim 2/3$, means only $1/3$ of the free ions form dipoles and the Debye length is relatively small, which agrees with our finding. The Coulomb interactions are basically long-ranged, but the presence of free ions effectively screens the interactions (Lee et al., 2014).

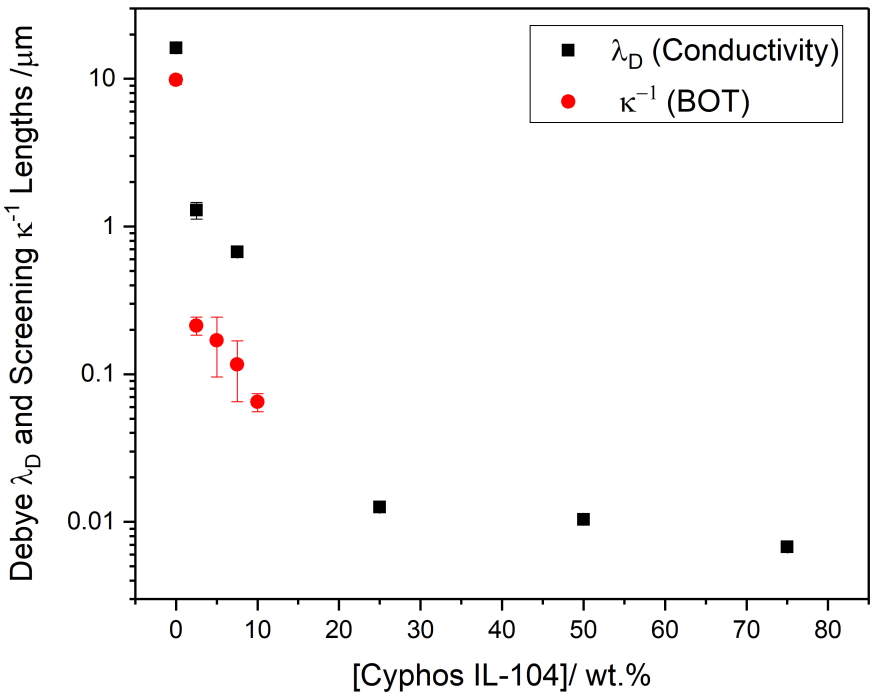

FIGURE 4.10: Combined plots of Debye and screening lengths varied with Cyphos IL-104 concentration

4.5 Summary

From our experimental results, the immense increase in ion density of the ionic liquid solution is seen and is predominantly caused by the dissociation of ions in solution. The ions screened the electrostatic interactions between PMMA colloids. Due to experimental limitations, we were unable to measure the screening length κ^{-1} of the IL system at high Cyphos IL-104 concentrations, so our screening length data κ^{-1} are limited to the low [IL] regime. There is no discrepancy of the measured screening length κ^{-1} and theoretical Debye length λ_D values, contrary to the electrolytic dodecane system in Chapter 3. For our system and some systems studied recently (Lee et al., 2014; Gebbie et al., 2013), the electrostatic screening effect due to the IL is mostly similar to dilute electrolyte solutions, where the classical Debye-H*ü*ckel approximation can be applied. Besides the presence of mobile free ions in solution, dipoles are possibly existed in the IL solution and the interactions between these formed dipoles are screened by the mobile ions. The background (calculated) dielectric constant essentially increased with the [Cyphos IL-104] due to an increase in polarizability of the molecules. Recent studies suggest that the formation of dipoles gives rise to the true dielectric constant, which considers the mean-field treatment and PB approximation into account.

The particle attraction was initially generated at low concentrations of Cyphos IL-104 and a stable dispersion was observed at much higher [Cyphos IL-104]. This was initially unexpected due to the large particle clusters and aggregates formed in the electrolytic dodecane system (Chapter 3). The high viscosity of the IL fundamentally reduces the particle aggregation kinetics and the colloidal stabilization is achieved.

Chapter 5

Evaporation Kinetics of Non-Polar Colloidal Droplet

This chapter introduces one practical application of a colloidal dispersion, which is the evaporation of droplets. Firstly, we introduce the fundamental concept of an evaporation process and the procedures to analyze and address the non-uniformity of the deposition pattern of an evaporating colloidal non-aqueous droplet, which is known as 'the density of the ring or particle density at the edge'. Then, we will discuss the evaporation kinetics and important terms concerning the evaporation process such as the Peclet number and the droplet model used for this work. The effect of a surfactant on the evaporation kinetics, and the contact line mobility is discussed later in this chapter.

5.1 Introduction

Evaporation can be simply defined as a transition state from liquid to gas or vapour. For instance, evaporation of a water droplet on a solid surface requires a certain amount of energy to convert the liquid into water vapour and the process can be enhanced with increasing temperature, surface area and lowering pressure. The degree of evaporation of a liquid can be easily measured from its vapour pressure. The volatility of a liquid can be denoted by its vapour pressure value, where indicates the high tendency of solvents molecules to escape, undergoing a phase transition. (Bertrand et al., 1977). The thermodynamic properties and vapour pressure values for some commercial solvents are presented in Table 5.1. The evaporation of a liquid is a process where heat is transferred from the atmosphere to the drop surface by convection and conduction and the vapour is generated from the surface to the atmosphere by convection and diffusion. The balance between convection and diffusion of an evaporating liquid can be quantified using the Peclet number Pe. A more detailed discussion about Pe will be discussed in subsection 5.3.1.

	Water	**Dodecane**	**Hexane**
c_p/ J/Kmol	74.5	376	195.33
ΔH_v/ kJ/mol	40.65	61.52	28.85
$\alpha_D \times 10^{-7}/m^2 s^{-1}$	1.46	4.96	9.37
P_v /kPa	3.169	0.00212	20.492

TABLE 5.1: The molar heat capacity c_p, Enthalpy of Vapourization ΔH_v, Thermal Diffusivity α_D and Vapour Pressure P_v of water (Ambrose and Lawrenson, 1972), dodecane (Rydberg, 2004; Daubert, 1989) and hexane (Majer, Svoboda, and Kehiaian, 1985; Martin and Youings, 1980) at T= 295.15 K and P= 1 atm.

First, let us start with the evaporation of water. The hydrogen bond that holds water molecules together is disrupted by heat via an increase of kinetic energy between water molecules, then releasing the water molecules into the air as water vapour (Nagata, Usui, and Bonn, 2015). It is well understood that the evaporation of a liquid is highly dependent on the temperature, humidity and air velocity (Hisatake, Tanaka, and Aizawa, 1993). Comparing the vapour pressure data of water and two hydrocarbon solvents used in this work in Table 5.1, it is obvious that the degree of evaporation increases in the following order, dodecane $<$ water $<$ hexane, at the same temperature, atmospheric pressure and air velocity. However, the molecules of these solvents are held together by different intermolecular forces. As discussed before, the strongest force exist between water molecules is the hydrogen bond, formed due to the polarity between hydrogen and oxygen atoms (Huyskens, Luck, and Zeegers-Huyskens, 2012; Israelachvili, 2011). This is not seen in hydrocarbons due to less or negligible degree of polarity between the atoms in the molecules. Molecules in alkanes are held together by weak London dispersion force, and the strength of this force depends on the molecular polarizability, which is a function of the atomic polarizability and the number of atoms in the alkane backbone chain (Mavroyannis and Stephen, 1962; Israelachvili, 2011). A higher number of the backbone chain results in a higher boiling point of the overall molecules, as what we can see from the value for hexane and dodecane in Table 5.1.

In our work, we used two contrasting hydrocarbons, hexane and dodecane. The thermal diffusivity α_D of hexane is about two times higher than the value for dodecane. Thermal diffusivity measures the rate of heat transfer from the hot part to the colder part of the system (Cameron and Bull, 1962; Salazar, 2003). In a homogeneous and isotropic medium, considering there is no heat generated inside the system, the relation between the thermal diffusivity α_D and the rate of heat transfer $\delta T/\delta t$ can be expressed as (Salazar, 2003),

$$\alpha_D . \frac{\delta^2 T}{\delta x^2} = \frac{\delta T}{\delta t} \tag{5.1}$$

Imagine a spherical droplet of a hydrocarbon liquid on a glass substrate as depicted in Figure 5.1, heat transfer occurs from the surrounding environment to the surface curvature of the droplet and eventually to the surface of the glass substrate through the liquid droplet. The temperature gradient in the liquid droplet varies, where the region near to the solid substrate (region 1) is the coldest region, and the temperature of the liquid in that region is closest to the temperature of the substrate and liquid molecules near to the surface curvature of the drop (region 5) is the warmest, with the highest kinetic energy.

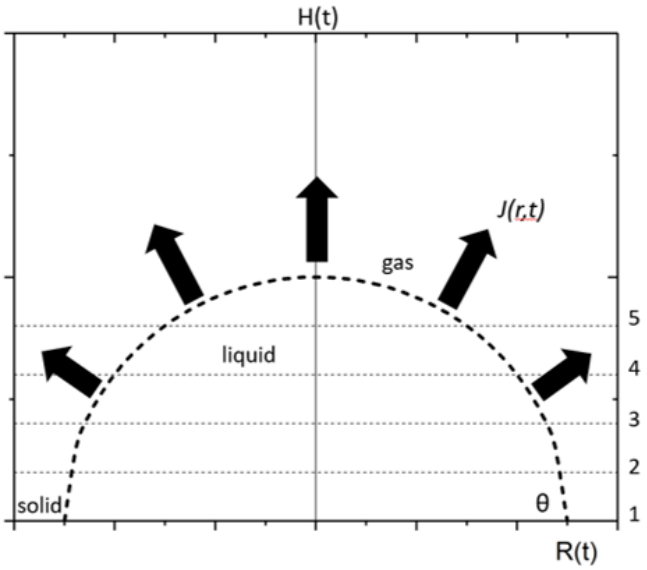

FIGURE 5.1: Physical schematic of a liquid droplet on a horizontal solid surface

The rate of diffusion of thermal energy is larger in hexane than dodecane, hence the thermal equilibrium of hexane system is achieved much quicker than in dodecane, once the solvent has fully evaporated (Rydberg, 2004; Majer, Svoboda, and Kehiaian, 1985). The temperature difference between region 5 to region 1 (Figure 5.1) is much more in hexane than in dodecane. Added to that, the enthalpy of vapourization of the hexane is lower than dodecane, which explains why hexane only needs a small amount of energy per mole in order to overcome the intermolecular interactions between hexane liquid to undergo the phase transition, hence evaporation is much quicker than dodecane. At standard room temperature and pressure, the temperature changes on the vertical plane are created by the temperature profile of the surroundings and the diffusion rate of the hydrocarbon molecules (Bahadori, Nwaoha, and Clark, 2013; Zhang, Wu, and Mu, 2017). Another important thermodynamic property to measure the evaporation behaviour of a liquid is the thermal expansion coefficient α_a. The thermal expansion is a volume change

(or expansion) in a fluid with a response from a thermal stress built within the system ($\alpha_a = (1/V)(dV/dt)_P$). The thermal expansion depends on the intermolecular interactions; kinetic energy of the fluid molecules (Hepler, 1969). Both thermal expansion coefficient and specific volume decay exponentially with increasing alkane chain length and the values asymptoting at carbon length, N=36, and N=20 respectively. From their data, the thermal expansion of hexane is about 50% higher than dodecane, suggesting the fast evaporation velocity of hexane (Huang, Simon, and McKenna, 2005).

In our work, we focused on the evaporation process of a non-aqueous droplet containing colloidal particles. Evaporation of a colloidal droplet is a vital process due to its important industrial applications such as coating, inkjet printing and layering processes (Deegan et al., 1997; Kavehpour, Ovryn, and McKinley, 2002). Evaporation patterns of droplets suspended with colloidal particles on solid surfaces have always been an interesting observation. One of those interesting deposition patterns is the well-known 'coffee-ring' stain, where the deposit formed a ring-like structure at the periphery of the droplet. The 'coffee-ring' phenomenon is predominantly caused by the pinning of three-phase contact line at the droplet edge (Deegan et al., 1997; Hu and Larson, 2006a; Anyfantakis and Baigl, 2015). The capillary flow induces the migration of the particles in the droplet, reaching the contact line and being pinned, formed a ring-like structure. Generally, there are several factors influencing the drying pattern of an evaporating droplet, including the surrounding temperature and pressure, particle mobility, and interactions between deposited materials with the substrate.

Deegan and coworkers were the first to measure quantitatively the deposition of drying particle-laden droplets. The so-called 'coffee-ring' pattern formed due to the growth of evaporative flow in radial position and when the flow front reaches the contact line, the outward radial flux is induced by the differential evaporation rates across the drop as presented in Figure 5.2 (Deegan et al., 1997). The 'coffee-ring' is a stain pattern formed after evaporation of a liquid suspended with non-volatile solutes, where the residue is concentrated at the periphery of the droplet (Mampallil and Eral, 2018). The evaporation rate at the pinned edge is observed to be higher than the bulk (Figure 5.4) and the radial flux constantly transports more particles to the edge and the process will continue until all solvent is evaporated and most particles deposited at the edge, forming a fine ring-like pattern. Since then, the suppression of the 'coffee-ring' effect has been a common interest among researchers, manipulating various factors including contact angle, particles shape, and interfacial and flowing properties (Yunker et al., 2011a; Hendarto, 2013; Scriven and Sternling, 1960; Prabhu, Fernades, and Kumar, 2009; Zhao, Blunt, and Yao, 2010).

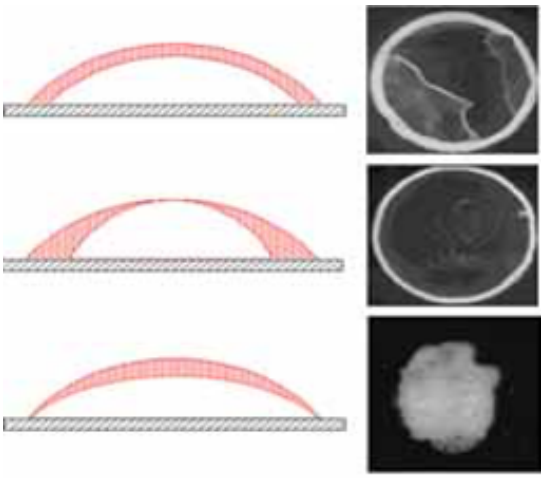

FIGURE 5.2: The pinning of the contact line draws particle towards the droplet edge, forming the 'coffee-ring' pattern (middle) and the uniform deposition pattern formed when the contact line is unpinned at the edge (bottom) (Deegan et al., 1997).

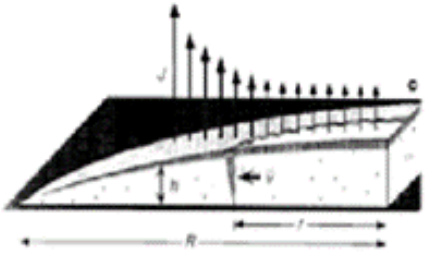

FIGURE 5.3: Non-uniform evaporation flux across the droplet radius (Deegan et al., 1997).

5.1.1 Suppressing the 'Coffee-Ring' Effect

A general manipulating approach to suppress the coffee ring is by creating an opposing flow to the radial capillary flow. The Marangoni effect is a phenomenon when a surface tension gradient exists in a system. It is a well-known concept of the Marangoni flow opposing the capillary flow, where the capillary effect arises when the flow of a fluid is driven by a capillary force in a meniscus or a confined channel (Cai and Zhang Newby, 2008; Washburn, 1921). In a colloidal droplet, the surface tension gradient is generated when there is a temperature gradient in the droplet. The region near to the glass substrate tends to cool down at a faster rate compared to the region near to the droplet curved surface. The development in the surface tension results in a thermocapillary shear stress at the interface which directs a surface flow from the region of low surface tension (high temperature/ curved surface) to the high surface tension (low temperature/ bulk) region (Hu and Larson, 2006b).

A recirculating flow generated from one point in the droplet of strong Marangoni flow, redistributing the colloids back to the droplet centre, consequently avoiding the contact line, hence a uniform deposition pattern is achieved (Hu and Larson, 2006b;

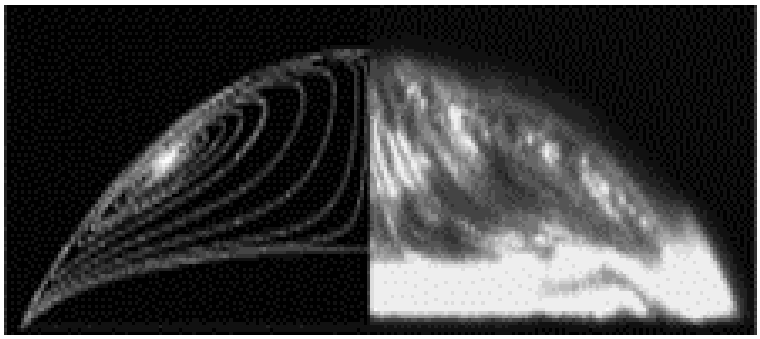

FIGURE 5.4: Marangoni vortex driven by a surface tension gradient in an octane droplet (Hu and Larson, 2006b).

Still, Yunker, and Yodh, 2012; Yunker et al., 2011b). The Marangoni flow also can be promoted by incorporating surfactants in non-aqueous droplets. Due to the nature of surfactants occupying the liquid-air interface, this creates a surface tension gradient and strong Marangoni flow in the droplet (Still, Yunker, and Yodh, 2012; Nguyen and Stebe, 2002). This effect is also pronounced in an aqueous droplet, where impurities and surface active agents present in the system (Hu and Larson, 2006b).

Wetting properties are one of the major factors contributing to the formation of a coffee-ring pattern. Contact angle measures the wetting behaviour of a liquid on a solid substrate, which is defined by the intersection between the liquid-solid interface and liquid-vapour interface (Good, 1992; Yuan and Lee, 2013). Larger contact angles ($> 90^o$) resulted from an unfavourable interface between two phases, and in contrast, a contact angle less than 90^o indicates favourable wetting (Erbil, McHale, and Newton, 2002). Li and coworkers, worked on the suppression of the coffee-ring effect by contact angle hysteresis (CAH). CAH is known as the difference between advancing and receding contact angles and can be controlled by the type of solid substrate used (Eral and Oh, 2013). On hydrophilic substrates like polycarbonate and mica, where CAH is relatively weak due to the affinity of the aqueous droplet and the substrate, a concentrated deposition pattern was spotted when surface inactive solutes were added in the droplet. The receding contact angle is more prone to occur on a hydrophilic substrate and the gradual contact line withdrawal inhibits the accumulation of particle at the droplet edge (Li, Sheng, and Tsao, 2013). In contrast, hydrophobic substrates with strong CAH such as graphite, the evaporated droplet tends to form a ring-like pattern. Contact line is persistently pinned on the surface because the receding contact angle is difficult to reach and as the evaporation takes place, the solutes reach their saturated solubility and precipitate out forming a ring-like deposition pattern before the contact line begins to withdraw (Li, Sheng, and Tsao, 2013).

The particle shape has a significant effect on the deposition pattern of an

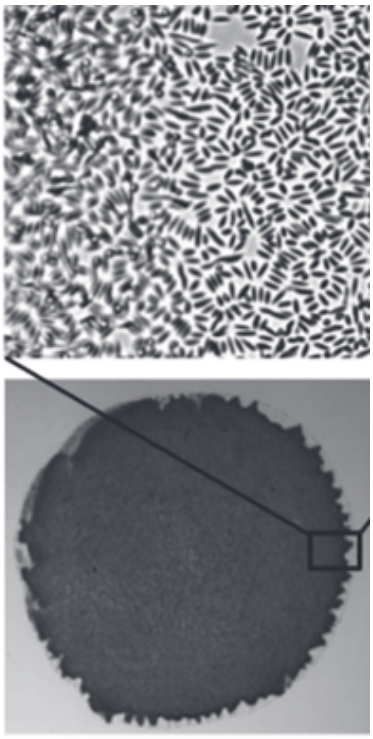

FIGURE 5.5: Loose-packed domain formed between the ellipsoids (top) yield a uniform deposition pattern (bottom) (Yunker et al., 2011b).

evaporating colloidal droplet. It was evidently proven that ellipsoidal particles resulted in a more uniform deposition pattern compared to spherical particles counterpart. Strong capillary interactions were enhanced when an anisotropy of the ellipsoids deforms the interface. Then, the ellipsoids were transported to the air-water interface and strong long-ranged interparticle attractions between the ellipsoids lead to the formation of loosely-packed structures near the interface. These loosely-packed structures prevent the suspended particles at any region in the bulk drop from reaching the droplet, thus suppressing the coffee-ring effect as presented in Figure 5.5 (Yunker et al., 2011b).

In an attempt to suppress the coffee-ring pattern formation, Cui and coworkers investigated the addition of hydro-soluble polymer additives in the SiO_2 microcolloids system. The pinned contact line is one of many crucial factors of the formation of the coffee-ring pattern. The polymer additives triggered the depinning of the contact line, resulting from the viscosity of the solution. As the viscosity of the system increases, the resistance of the outward radial flow is enhanced, making fewer particles transported to the droplet edge and eventually accumulated at the periphery, hence forming a uniform deposition pattern as illustrated in Figure 5.6 (Cui et al., 2012).

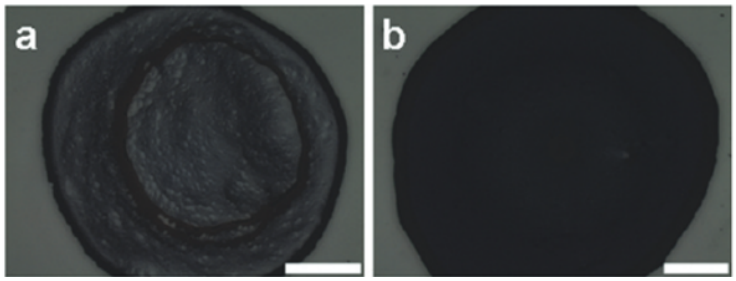

FIGURE 5.6: Uniform deposition pattern as a result of contact line depinning due to the viscosity of polymer-based microcolloidal system (Cui et al., 2012).

5.1.2 Importance of Droplet Evaporation in Industries

The inkjet printing process is not only limited to the printing on large or flat surfaces but also has been demonstrated on small parts and electrical components for labelling and branding purposes (Soltman and Subramanian, 2008; Zhang et al., 2012; Molesa et al., 2003). Due to its demanding technique, the utilization and optimization of producing a uniform morphology of colloidal inks on surfaces are crucial. Colloid scientists have been working on modifying the interactions between colloids and altering the physical properties of the colloidal system to cater to a smooth process, that can be useful for industries (Cui et al., 2012; Hu and Larson, 2006b; Yunker et al., 2011b; Bhardwaj et al., 2010). Meanwhile, from the technical aspect, the improvement of the printer nozzle, print head speed and jetting pressure are also in a developing stage (De Gans, Duineveld, and Schubert, 2004; Derby, 2010). Figure 5.7 demonstrates the non-uniformity of inkjet printed deposit which is not favourable in industries.

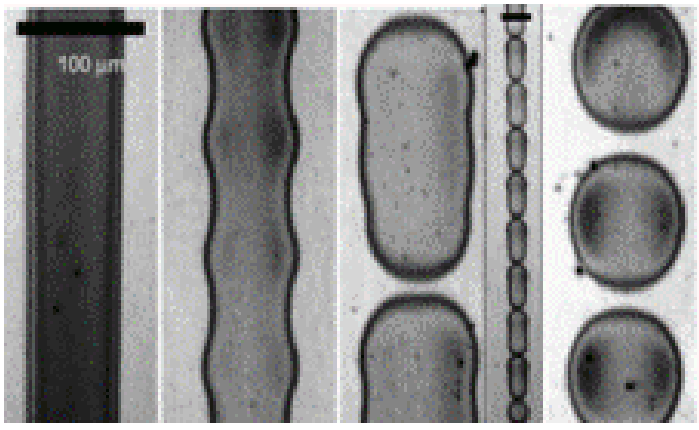

FIGURE 5.7: Non-uniform deposition pattern in inkjet printing (Soltman and Subramanian, 2008).

The formation of the coffee-ring pattern can be useful in biological applications. As the droplet evaporates, the volume fraction of the solute in the liquid increases. The interactions between solutes, forming large lumps and aggregates can

be functional as a cost-effective and robust method to detect biological sample(Han and Lin, 2012; Li et al., 2015). Wen and coworkers introduced a novel, inexpensive and ultra-sensitive method to detect bio-molecules (DNA, RNA and proteins) from the concentration of the coffee-ring formed upon the evaporation process (Wen, Ho, and Lillehoj, 2013). This provides an alternative and practical tool for clinical diagnosis and also water, food and environmental analysis (Torres-Chavolla and Alocilja, 2009).

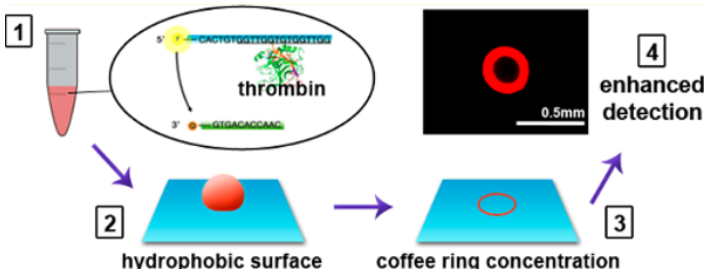

FIGURE 5.8: The detection of thrombin through the coffee-ring concentration (Wen, Ho, and Lillehoj, 2013).

5.1.3 Project aim

This work focuses on the behaviour of suspended particles in evaporating non-aqueous solvents. Fundamentally, the motivation of this work is not to suppress the 'ring'-shaped deposition pattern, but to elaborate and extend the investigation made in the past, from the perspective of evaporation kinetics and interparticle interactions. Most past work on the evaporation of colloidal droplet prioritizes the evaporation kinetics, using a single particle model, which is not ideal in practice.

Next, we will elaborate the experimental methods and setups to image the deposition pattern of an evaporating colloidal droplet on a glass substrate using a confocal microscopy technique. In the later subchapter, we will discuss the role of evaporation kinetics which depends on the properties of the solvent used on the deposition pattern of a colloidal droplet. Then we will discuss the main topic of interest, which is the role of interparticle interactions in the deposition patterns that was induced by the addition of an anionic surfactant, sodium dioctyl sulfosuccinate (AOT) and an oil-soluble organic electrolyte, tetradodecylammonium tetrakis (3,5-bis (trifluoromethyl) phenyl) borate (TDAT) (discussed in Chapter 3). Interestingly, we also found that AOT affected the deposition pattern differently when we changed the solvent.

5.2 Experimental

The synthesis of PMMA, IM-PMMA colloids and TDAT electrolyte are outlined in Chapter 2. All solvents and AOT were purified and the procedure was discussed in Chapter 2.

5.2.1 Preparation of hydrophobic glass slide

To make the glass substrate hydrophobic, microscope glass slides were coated with trichloro(octadecyl)silane (OTS) solution. OTS was purchased from Merck and stored in a desiccator due to hygroscopic properties of OTS (Drioli, Criscuoli, and Molero, 2017). The silane functional groups in OTS bind with the silicates in the glass, thus forming a layer of hydrocarbon coating on the glass substrate. Microscope glass slides were thoroughly washed to remove dirt and impurities by immersing them into an 0.1 wt. % alkaline Hellmannex aqueous solution and sonicated for 30 minutes. Then, the glass slides were rinsed and immersed with distilled water and left for sonication for another 20 minutes. Next, the glass slides were dried in a vacuum oven for 12 hours. To make the OTS solution, 0.2 ml of OTS were dispensed and mixed with 100 ml of hexane. The washed and dried glass substrates then were fully immersed in the OTS solution and kept away from the moisture-bound environment. The immersion was left for 4-5 hours. The coated slides then were rinsed and sonicated in hexane for 30 minutes. Finally, the coated glass substrates were left in the vacuum oven at room temperature for an overnight for drying.

5.2.2 Preparation of stock solutions

PMMA particles were centrifuged in dodecane and hexane separately using a Sorvall centrifuge for 10 minutes at 5000 rpm. After separation by centrifugation, the particles were resuspended in clear, dry solvent and the process repeated. The conductivity of the supernatant was measured after every two washes and the centrifuging process stopped when the conductivity of the supernatant approached the conductivity of the dried solvent. Then the particles were dried in a vacuum oven at 70^0C until the dry mass achieved a constant weight. The drying process took up to 24 hours.

Then, 0.1 wt.% of PMMA was made up in dodecane and hexane separately with varying concentrations of Dioctyl Sodium Sulfosuccinate surfactant (AOT). AOT was used as a charging species at a range of concentration from 0 mM to 100 mM to develop particles charge in the system. The stocks were mixed and shaken by a vortex mixer and placed on an electric roller to give a better dispersion.

PMMA functionalized with Poly (Ionic Liquid) (IM-PMMA) particles stocks were made up in hexane using similar AOT concentrations. The concentration of the particles was fixed at 0.1 wt.% in all stocks. Similar procedures used to prepare PMMA/dodecane dispersions with TDAT electrolyte. TDAT was added at a concentration range from 100 μM to 1 mM. TDAT was used to study the electrostatic interactions between PMMA colloids.

To dispense 2-3 μL droplets of the PMMA dispersions on the OTS coated slides, a 10 μL syringe was used. Slides were placed on a microscope stage. A total of 8 drops were placed on a microscope glass slide. Prior to being observed under the confocal microscope, the slides were then left undisturbed for 72-96 hours (for dodecane stocks) and 3-6 hours for hexane stocks, to allow solvent evaporation, leaving deposited PMMA particle.

5.2.3 Confocal Imaging and Droplet Model

The working principle of the confocal microscopy imaging was discussed in Chapter 2. The images were analyzed using ImageJ or FIJI (Schneider, Rasband, and Eliceiri, 2012; Schindelin et al., 2012). The radial profile analyzer plugin was used to examine the relative particle density across the droplet. The radial profile analyzer gives a plot of particle intensity throughout the droplet radius and takes account of the surface area of the droplet. The overall analysis of radial profile is based on Figures 5.9 and 5.10. From Figure 5.9, the particle density with respect to the radial distance $\rho(r,d)$ can be calculated from the intensity. R is the overall droplet radius and r is the radial distance of the droplet from the centre. Figure 5.10 shows the droplet model, where the droplet is subdivided into ten equivalent radial sections, known as the percentile. The region between red circles resembles the particle intensity/density at the edge while the region in the yellow circle resembles the droplet centre. The relative particle intensity at the edge and the centre (or any particular percentile in the drop) can be calculated by using equation 5.2 (we take the intensity at the droplet edge as an example), where I is denoted as the particle intensity, and the coordinate system is used to identify the location of particle intensity and density measured. As the droplet is segmented into ten radial profiles (percentiles) as featured in 5.10, for instance, the coordinate for the droplet centre is (r,d) = (0,1), while the coordinate for the droplet edge or occasionally referred as the 'ring' is (r,d) = (1,1).

The intensity at the 'ring' is equal to the fraction of the total intensity at the inner part of the droplet within the 'ring' to the total intensity of the droplet base radius R,

$$I_{ring} = \frac{I_{r,d}}{I_o} = \frac{\sum_{r-d}^{r} I_i}{\sum_{i<R} I_i} \tag{5.2}$$

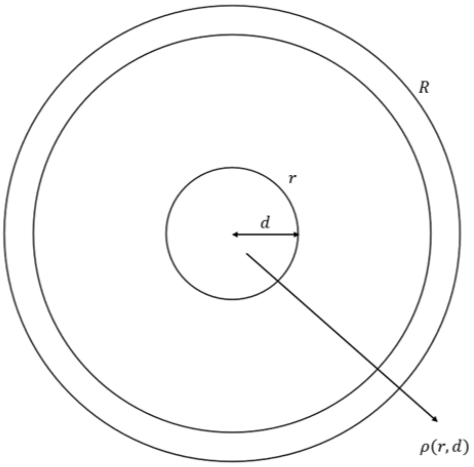

FIGURE 5.9: A droplet model with radius R

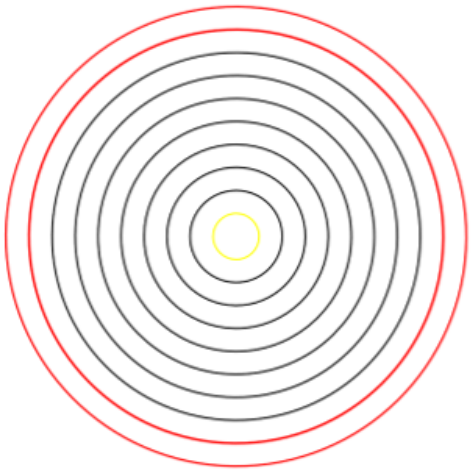

FIGURE 5.10: Droplet percentile

and the total area of the droplet is denoted as A_d,

$$A_d = \pi R^2 \tag{5.3}$$

and the area of any position (percentile) in the droplet is denoted as A_i, in this case, the area of the first (centre) and last (edge) percentiles were calculated using,

$$A_i = \pi(r-d)^2 \tag{5.4}$$

Finally, the number of particles per unit area is calculated as the average particles density at specific position (percentile),

$$\frac{\rho(r,d)}{\rho_o} = \frac{\sum_{r-d}^{r} I_i}{\sum_{i<R} I_i}\left(\frac{\pi R^2}{\pi r^2[1-(\frac{1-d}{r})]^2}\right) \tag{5.5}$$

Based on Figure 5.10, the average particle density at the first and last percentiles were calculated. The particles density for first percentile portrays particles aggregation at the droplet centre and the last percentile for the particles accumulation on the glass surface at the droplet edge.

5.3 Evaporation Kinetics

In this section, we will discuss the fundamentals of evaporation flow and the quantification of Peclet number *Pe* and how the evaporation properties and lubrication model can be used to determine the final deposition pattern of an evaporating non-aqueous colloidal droplet.

5.3.1 Peclet Number and Evaporation Flux

As mentioned in the previous subchapter, the evaporation of a liquid to vapour requires both convection and diffusion processes. The combination and distinction between these two effects are often combined into the Peclet number *Pe*. Fluid Peclet number Pe_{liq} is a dimensionless number and can be defined as the ratio of thermal energy convected to the liquid to thermal energy conducted within the liquid system. The thermal energy conducted within the fluid resulted in the mass diffusion of the component in the system. Fick's first law accounts for the diluted fluid flux due to diffusion, which only depends on the particles interaction with solvent, by the diffusion coefficient, D. D is the magnitude of molar flux through a surface per unit concentration gradient out-of-plane,

$$D \equiv \frac{N_i}{\nabla c_i} \tag{5.6}$$

Diffusion of a molecular species in gas is typically faster than in liquid, which is about 10^{-6} to 10^{-5} m^2/s in gas and about 4 times of magnitude lower in aqueous solution. A Maxwell-Boltzmann distribution predicts the mean free path and average velocity of molecules in an ideal gas from which the diffusion coefficient obeys the correlation with temperature and pressure as expressed in equation 5.7. This shows that diffusion is much faster at a higher temperature.

$$D \propto \frac{T^{3/2}}{P} \tag{5.7}$$

Convection is a process when a mass transfer or mass loss occurred due to the bulk motion of the fluid. The convective component of an evaporation process results in mass transport due to velocity changes of the bulk fluid rather than randomization of single molecular species in the system (diffusion). The bulk motion contributes in the flux of dilute species and it can be expressed as,

$$N_{i,conv} = c_i v_f \tag{5.8}$$

where c_i is the concentration of a species and v_f is the fluid velocity, resulting from the convection process. From the mass continuity equation, the change in concentration of a fluid at a point can be substituted to,

$$(\frac{dc_i}{dt})_{conv} = -\nabla.N_{i,conv} = -c_i\nabla.u - u.\nabla c_i \tag{5.9}$$

For an incompressible fluid, the first term on the right hand side equals to zero as a result of the conservation of volume of fluid, which yields equation 5.10 and it is known as the time-dependent convection equation.

$$(\frac{dc_i}{dt})_{conv} = -u.\nabla c_i \tag{5.10}$$

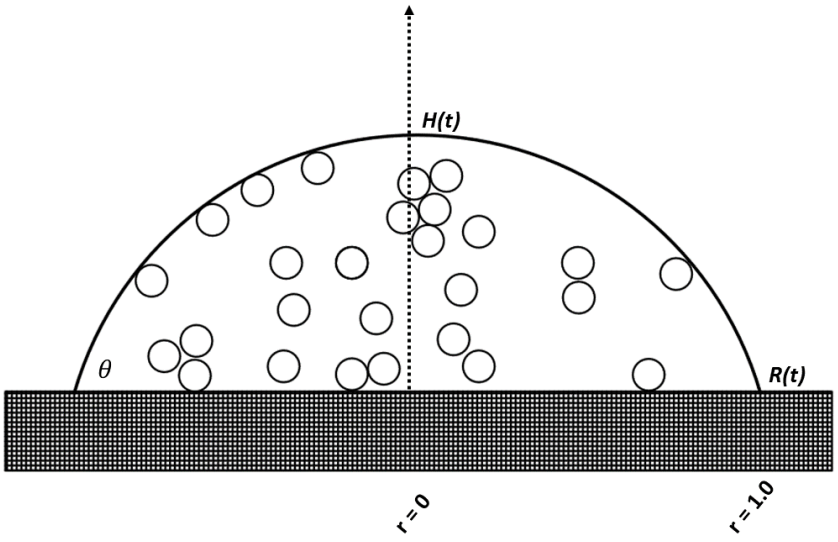

FIGURE 5.11: Schematic of a colloidal droplet

Let us consider an evaporating droplet suspended with significantly-charged colloidal particles as depicted in Figure 5.11. Referring back to Deegan approach, which is the most accurate explanation on the evaporation kinetics of a droplet so far, the evaporation flux $J(r,t)$ depends on the rate-limiting step, whether the transfer rate from the droplet surface to the droplet base as presented in Figure 5.1, or the immediate diffusive relaxation of the saturated vapour on the droplet surface. Initially, they outlined that the evaporation flux is non-uniform across the droplet radius but in the latter case, the flux is uniformly distributed. Next, we will discuss the limiting boundary conditions for our droplet system.

For a particle-laden liquid suspension, the Peclet number of particle Pe_p can be expressed as equation 5.11, where R is the droplet radius, v_o is the droplet initial evaporating velocity, H is the droplet height and D is the diffusivity of the

particles. Diffusion of particles with radius r in a solvent with viscosity η can be calculated using the Stokes-Einstein relation as expressed in equation 5.12,

$$Pe_p = \frac{R^2 v_o}{H.D} \tag{5.11}$$

$$D = \frac{kT}{6\pi\eta r} \tag{5.12}$$

where k is the Boltzmann constant and T is the absolute temperature. From this expression, it is postulated that solute particles obey Stokes law for drag, in which a drag force is exerted on the diffusing particles by the solvent molecules. From equation 5.11, the v_O of the solvent was simply calculated using the Navier-Stokes mass conservation equation,

$$\dot{m} = \rho v A \tag{5.13}$$

where $\dot{m}, \rho, v$, and A are the mass flow rate, density, velocity and the cross-sectional flow area respectively. The solvent was left to evaporate on a petri dish, then the mass loss of the solvent over time was recorded. The evaporation flux for a liquid containing solid particles can be expressed as,

$$J(r,t) \propto (R-r)^{-\lambda} \tag{5.14}$$

where the droplet is axisymmetric in which the evaporation flux always induced a height-averaged radial flow towards the contact line with λ depends on the contact angle θ, $\lambda = \frac{\pi - 2\theta}{2\pi - 2\theta}$. R is the pinned radius of the droplet and r is the moving radius of the droplet when the evaporation takes place. At the droplet edge, where $r = R$, the evaporation flux is zero, considering the evaporation is complete and the velocity v is zero. The local evaporation velocity v_o was calculated from mass loss rate from solvent evaporation and the non-uniform velocity is considered. Taking the analogy that electrostatics is crucial in evaporation of the system, the flux is assumed increases with droplet radius and can be expressed as,

$$v(r) = v_o R^{0.5} (R-r)^{-0.5} \tag{5.15}$$

where R is the radius of the droplet and r is the local radius at any point in the droplet. In order to qualify the droplet as a spherical cap model system, the height of the droplet $H(t)$ must be smaller than the base radius of the droplet $R(t)$,

$\frac{H^2}{R^2} << 1$ and the contact angle θ is small enough to provide the parabolic function given in the expression,

$$h(r,t) = H(t)\left[1 - \frac{r^2}{R^2(t)}\right] \tag{5.16}$$

The contact angle $\theta(t) = \frac{2H(t)}{R(t)}$ is small enough to ignore the depth-wise sedimentation and gradient of the droplet subsitutents, therefore the liquid is thin enough to consider the lubrication approximation.

The droplet radius R is approximately 1000 μm and to ignore the gravitational effect on the droplet interface over the surface tension effect, the Bond number Bo must be small,

$$Bo = \frac{\rho_o.g.R^2}{\gamma_o} \approx 10^{-3} \tag{5.17}$$

where ρ_o is the solvent density (655 kg m^{-3} for hexane and 750 kg m^{-3} for dodecane), g is the acceleration due to the gravity (9.81 N kg $^{-1}$) and γ_o is the interfacial surface tension of air-solvent (18 mN m^{-1} for hexane and 24 mN m^{-1} for dodecane) at a standard temperature and pressure. To consider the creeping flow limit and lubrication flow approximation into the consideration, the Reynolds number Re must be less than unity to neglect the inertial terms. The Reynolds number measures the scale of inertial effect to the viscous effect. The Re for dodecane and hexane are $\sim 10^{-6}$ and $\sim 10^{-3}$ respectively. It can be expressed as,

$$Re = \frac{\rho_o.v_o.R}{\eta} \tag{5.18}$$

In the next section, we discuss the effect of solvent evaporative properties on the deposition pattern of an evaporating colloidal droplet.

5.3.2 Effect of Solvent Evaporation and Thermodynamics on Droplet Evaporation

The whole point of this chapter is to compare the outcome of two main key elements modified in the project on the final pattern of evaporating colloidal droplet,

namely thermodynamics and hydrodynamics. The thermodynamics effect is influenced by the evaporation properties of the solvent itself, which has been discussed extensively in previous works mainly on an aqueous solvent. We used two hydrocarbon solvents with a contrast of thermodynamic properties as discussed in section 4.1. PMMA particles were suspended in dodecane and hexane, and the deposition pattern of each droplet system is presented in Figures 5.12 and 5.13. From these figures, the enrichment of particle density at the edge can be spotted, which represent the formation of a 'coffee-ring' pattern. This can be postulated to be due to the migration of particles from the centre or other locations in the droplet towards the droplet edge induced by the capillary flow as discussed by Deegan (Deegan et al., 1997). The integrated intensity plots explain the raw intensity of the fluorophore in the particles detected using the confocal microscopy technique and both plots show that the particle intensity increases at the droplet edge.

As mentioned earlier, we added AOT surfactant to alter the electrostatic interaction between PMMA particles in both hexane and dodecane. The primary effect of AOT on the deposition pattern will be discussed ilater. However, this effect was not dominantly seen in hexane system due to the thermodynamic properties of hexane controlled the system, yielding the formation of a fine 'ring'-liked pattern.

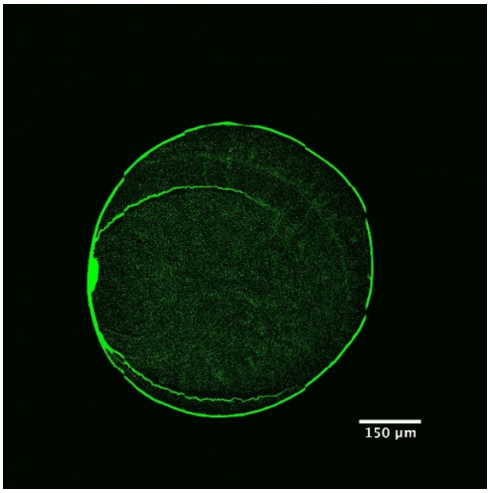

(A) PMMA/hexane Droplet

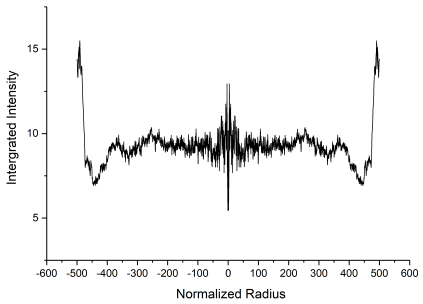

(B) Intensity of deposited particles in PMMA/hexane droplet with respect to the droplet radius

FIGURE 5.12: Deposition pattern of PMMA/hexane droplet

$$\tau_{mix} = \frac{a^2}{\pi 2D} \tag{5.19}$$

From the diffusional mixing time τ_{mix} of particles with radius a in a solvent (Reid et al., 2018), with D the diffusivity of the particle in a solvent, the τ_{mix} in dodecane is six times higher than in hexane. The increase in τ_{mix} indicates that the particles have more time to form interactions between each other, where the colloidal hydrodynamics are not controlled by the fluid flow of the carrying solvent. From

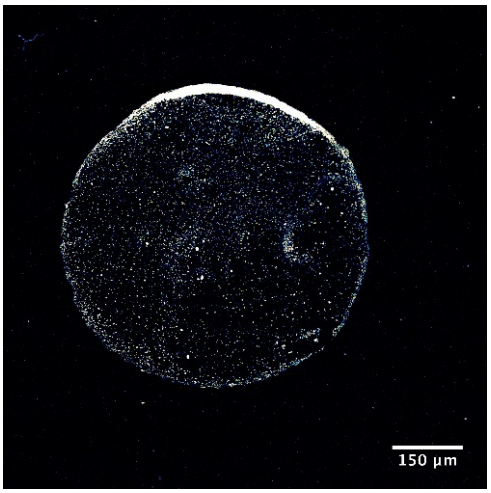

(A) PMMA/dodecane Droplet

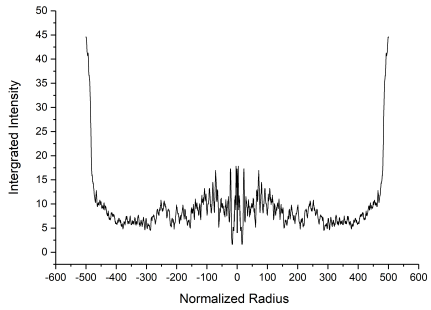

(B) Intensity of deposited particles in PMMA/dodecane droplet with respect to the droplet radius

FIGURE 5.13: Deposition pattern of PMMA/dodecane droplet

the calculation of evaporation velocity across the droplet radius, it is shown that the evaporative flux in our system obeys the first Deegan approach, where the velocity is not uniform across the droplet behaviour. Figure 5.14 shows the evaporation velocity profile for both solvents across the droplet radius. The non-uniformity of the solvent evaporation strengthens then capillary flow in the system, thus enhancing the formation of 'coffee-ring' pattern (Eales et al., 2015).

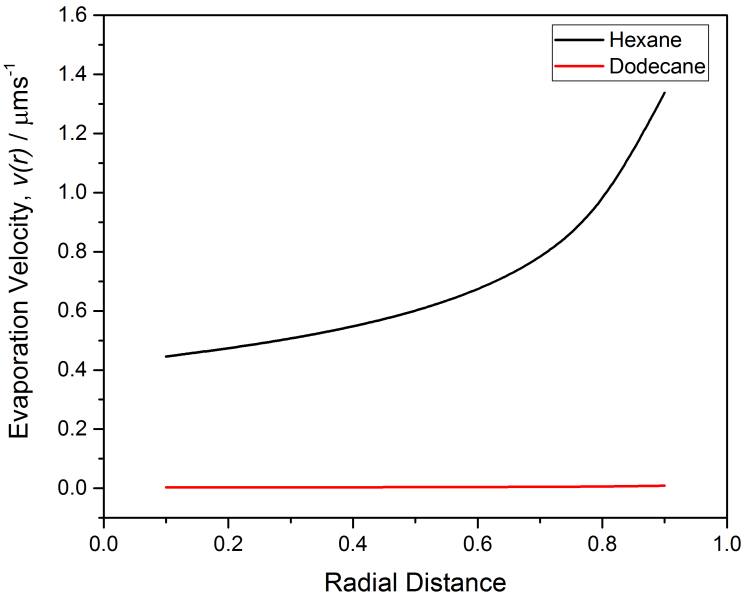

FIGURE 5.14: The evaporation velocity profile of dodecane and hexane with respect to droplet radius

Eales and co-workers also mentioned the effect of *Pe* on the influence of diffusivity of solute in the solvent. Lower *Pe* resulted in the progression of a diffusional

mechanism in the system, thus opposing the outward capillary flow and diminishing the formation of a 'coffee-ring' pattern. When Pe is approaching to zero, the 'coffee-ring' pattern is completely eliminated (Eales et al., 2015). We calculated the Pe for hexane system is four times larger than the dodecane droplet, indicating that the evaporation of hexane was dominantly driven by convection. From a theoretical approach made by Man and Doi, the retraction of the contact angle occurred at a faster rate in a highly evaporative solvent, in which the initial contact angle of the drop θ_o is much larger than the equilibrium contact angle when the evaporation halted, θ_e. In the case, for low Pe, the $\theta_o \sim \theta_e$ and this can be seen in dodecane droplet. Finally, the evaporation timescale of the droplet characterizes the final deposition pattern (Man and Doi, 2016). Man and Doi clarified that the evaporation timescale coefficient can be represented as $k_{ev} = \frac{\tau_{re}}{\tau ev}$, which represents the ratio of relaxation time to evaporation characteristic time. The relaxation time τ_{re} measures the rate of contact angle changes $d\theta/dt$ as the evaporation takes place with $\tau_{ev} \propto d\theta/dt$. Hexane in this case has high k_{ev} value, where τ_{re} is high, indicating that the hexane drop evaporates rather quickly and having low $\tau_{ev} \sim \frac{1}{dV/dt}$, where dV/dt is the change of droplet volume over time.

5.4 Contact Line Mobility

The pinning of the contact line at the droplet edge is an undebatable requirement for the appearance of the 'coffee-ring' pattern. Since it was first addressed by Deegan and coworkers (Deegan et al., 1997), there has been an increasing interest to suppress the 'ring' pattern by modifying the contact line pinning phenomena.

Man and Doi (Man and Doi, 2016) proposed a model of a drying droplet with a moving contact line, and how it affects the deposition patterns. They proposed two important parameters which modify the deposition pattern of an evaporating droplet. The first parameter known as the contact line friction coefficient k_{cl}, which characterizes the extra contact line friction ξ_{cl} relative to normal hydrodynamic friction ξ_{hydro} (Man and Doi, 2016). They postulated that k_{cl} depends largely on the material parameter determined by the droplet and the substrate, and can be simplified as ξ_{cl}/ξ_{hydro}, and $\xi_{hydro} = 3C\eta/\theta$ with θ is contact angle of the drop and C equals to ln[R(t)/2($10^{-6}R_o$] ($R(t)$ is the evaporated droplet radius and R_o is the radius of the drop), calculated from the energy dissipation function (Man and Doi, 2016). The energy dissipation function is based on the lubrication approximation, which considers the energy dissipation due to hydrodynamics and the contact line motion over the substrate. From the expressions, we know that k_{cl} depends on the viscosity of the carrier solvent. Lets consider droplets of multiple solvents and for a water droplet, the dynamic viscosity, η at 20 ^{o}C is 0.89 mPa.s and for a viscous solvent, dodecane, for example, the η = 1.36 mPa.s, while the least viscous solvent,

hexane has the dynamic viscosity at about 0.3 mPa.s at room temperature. The ξ_{hydro} for dodecane is about 5 times larger than hexane and 2 times larger than water. This predicts that k_{cl} is small for a viscous solvent, yielded from a small ξ_{cl} value. Theoretically, when ξ_{cl} is small, the hydrodynamic friction dominates the system, so the pinning of the contact line is known to be temporary, thus inducing the mobility of the contact line.

For an evaporating droplet suspended with solid particles, the hydrodynamic friction is enhanced when the separation between solid particles with the glass substrate becomes closer and the separation between these is denoted as d_{hydro} in Figure 5.15. This region is often referred as the liquid pocket as presented in 5.16. When the separation between contacting particles and glass substrate becoming really closed (the liquid pocket gets smaller), the friction behaviour can be explained by the transition from hydrodynamic to mixed and boundary lubrication regimes eventually. The contact line is pinned indefinitely if the no liquid pocket formed between the two asperities as the extra friction constant is high, resulted to high value of $K_{cl} \sim 1$. For a liquid droplet with a moving contact line, the lubrication approximation model used is the hydrodynamic lubrication. The boundary and mixed lubrication models are less accurate for this system due to the lubrication between solid particles and glass substrate depends on the properties of the solvent rather than the surfaces of the solid. Referring back to the expression $\xi_{hydro} = 3C\eta/\theta$, the hydrodynamic friction ξ_{cl} is dependent on the viscosity of the liquid. Higher viscosity liquid such dodecane will enhance more drag force between the interacting particles and solid substrate rather than friction due to the asperities of the contacting surfaces. Finally, the correlation between the contact line friction coefficient k_{cl} and the viscosity of the solvent η can be expressed as,

$$k_{cl} = \frac{\xi_{cl}\theta}{3C\eta} \tag{5.20}$$

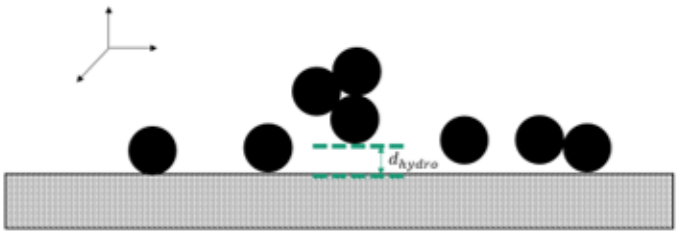

FIGURE 5.15: Lubrication model of liquid droplet. The distance between particles surfaces and glass substrate is denoted by d_{hydro}, and also known as liquid pocket

The depinning process of the droplet can be characterized by the retraction

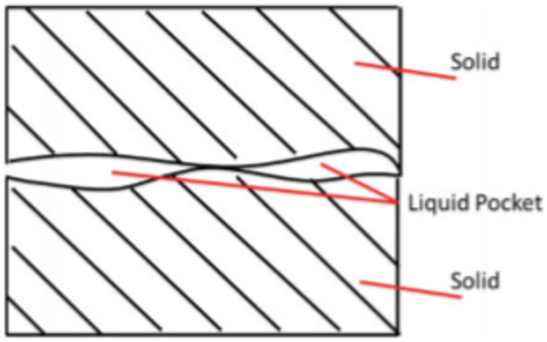

FIGURE 5.16: Liquid Pocket location between two asperities Schirru, 2017

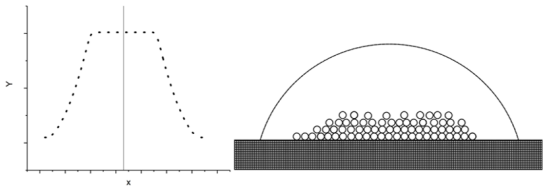

(A) Mountain-like deposition pattern

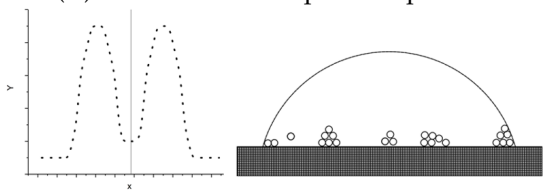

(B) Volcano-like deposition pattern

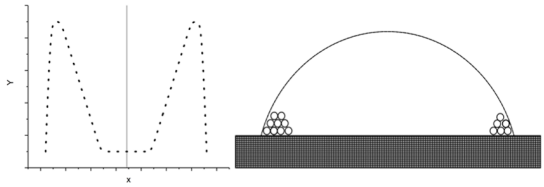

(C) Coffee-Ring deposition pattern

FIGURE 5.17: Three deposition patterns of evaporating colloidal droplet as proposed by Man and Doi Man and Doi, 2016

of the contact angle θ, and the mobilization of the contact line. From observation, in order for the 'ring' pattern to be suppressed, Man and Doi mentioned that they saw the deposition pattern of 'volcano-like' as presented in Figure 5.17. The pattern transition from the 'coffee-ring' to 'volcano' and finally to the 'mountain'-like shape can be triggered by the modifying k_{cl} value. Experimentally, we observed that AOT has largely influenced the k_{cl} value and at [AOT] $>$ 30 mM, we saw the contact line mobilization occurred, migrating the solid particles from the edge towards the centre at the droplet at [AOT] = 100 mM. Referring to Figure 5.18, the PMMA density across the dodecane droplet radius varied with [AOT] is clearly shown. Focusing on the shifting of the peak in Figure 5.19, which represents the maximum density of PMMA particles at respective radius of the droplet r/R, without any AOT, the enhancement

of particles density towards the droplet edge can be seen, which indicates the formation of 'ring'-like pattern. As the AOT concentration increased to 30 mM (light blue profile), the formation of two peaks were spotted, mimicking the 'volcano'-liked pattern and the profile peak starts to shift towards the inner part of the droplet radius at 50 mM of AOT (purple) and eventually at 100 mM (green), the maximum peak appeared at r/R = 0.15 to 0.35, which resembles the 'mountain'-shaped pattern. This transition can be illustrated by the deposition patterns presented in Figure 5.20.

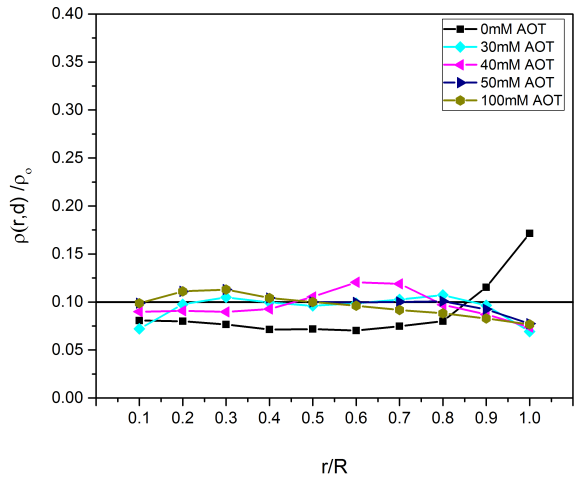

FIGURE 5.18: The particle density in evaporated dodecane across the droplet radius with varying [AOT]

From the observation and particle density profile $\frac{\rho(r,d)}{\rho_o}$ across the droplet radius $\frac{r}{R}$ in Figure 5.18, the peak at droplet edge (r=R) was gradually shifted towards the inner part of the droplet ($0.1 \geqslant r \leqslant 0.8$) with AOT concentration. This is owing to the lubrication effect of AOT towards the contacting particles and glass substrate surfaces. Generally, surfactants are widely used as a part of ingredients in lubricants for automotive. It is also widely known that surfactant has a significant role in enhancing the lubricative characteristic in aqueous solution, to improve the friction between two working mechanical steel surfaces (Kumar, Singh, and Mishra, 2016). The tribological behaviour of some surfactants they used in the study, namely Tween 20, Tween 80 and oleic acid in water, between two contacting steel surfaces can be explained using the Stribeck curve. Without any surfactant, the friction coefficient between two plates of steel was high and the curve shifted towards the lower friction regime when surfactant was incorporated in. The lubricating effect of a surfactant-containing fluid becomes prominent when surfactant was added at high concentration (>>CMC), in order to provide sufficient coverage on the interacting surfaces (Kumar and Biswas, 2008).

In our case, AOT molecules formed reverse micelles in dodecane and these reversed micelles were adsorbed on the particle surface. As more AOT was added to the non-aqueous system, the AOT coverage on PMMA particle surface could

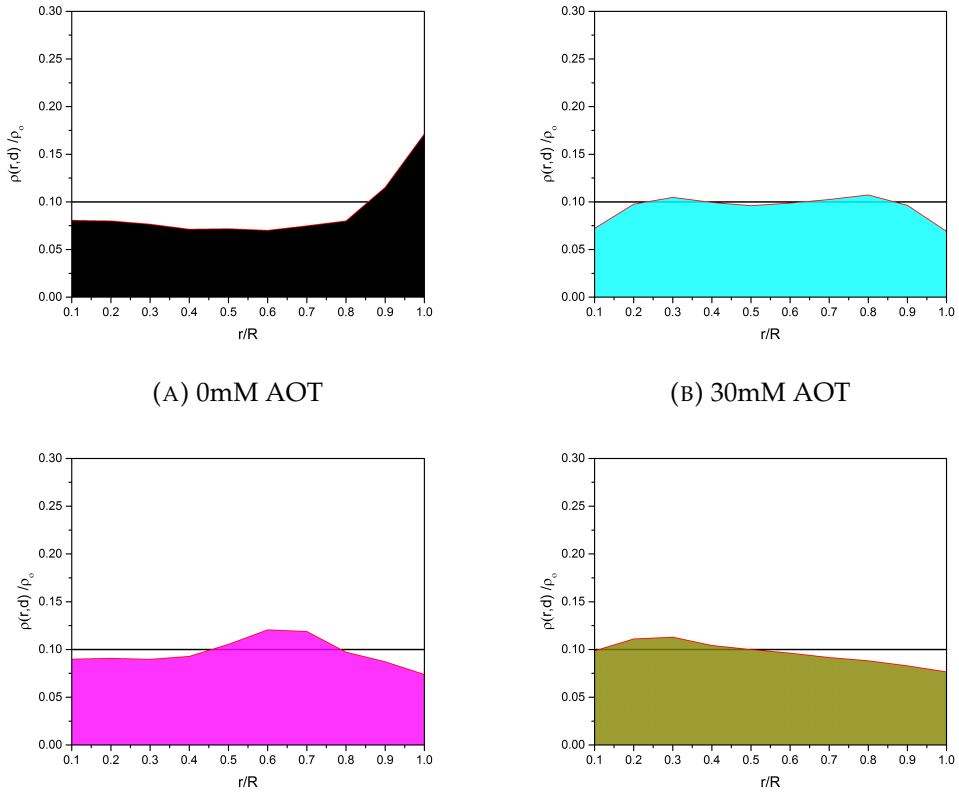

(A) 0mM AOT

(B) 30mM AOT

(C) 40mM AOT

(D) 100mM AOT

FIGURE 5.19: The shifting of maximum particle density across the droplet radius with [AOT] in evaporated dodecane

be enhanced. The mechanism on how AOT behaves in the non-aqueous solvent will be thoroughly discussed in the next chapter. Increasing AOT concentration in PMMA/Dodecane system will not only increase the number of micelles formed and attracted on the PMMA surface, but some reverse micelles can possibly form a layer on the glass substrate. This layer formation may originate from the electrostatics between reversed charged micelles and charged glass substrate. Marglewski and Plaza indicated that the formation of tribofilm on the solid surface largely influenced by the degree of packing and orientation of surfactant molecules in the system. In a solution containing surfactant molecules, there are two significant equilibria involved; the formation of micelles and the adsorption of the micelles and molecules on the solid surface as depicted in Figure 5.21 (Margielewski and Płaza, 2010).

Interestingly, this phenomenon is not seen in hexane droplets, regardless of the type of particles used. We used two particles with different magnitude of surface effective charge $\frac{Z\lambda_b}{a}$, where λ_b is the Bjerrum length with particle radius a. PMMA is less charged than IM-PMMA and in the later subchapter, we will explain how the particle charge affects the deposition patterns of the colloidal particles-laden non-aqueous droplet. Briefly, when the particles are highly-charged, we observed the suppression of 'ring'-like pattern even in hexane droplet. As discussed in the earlier

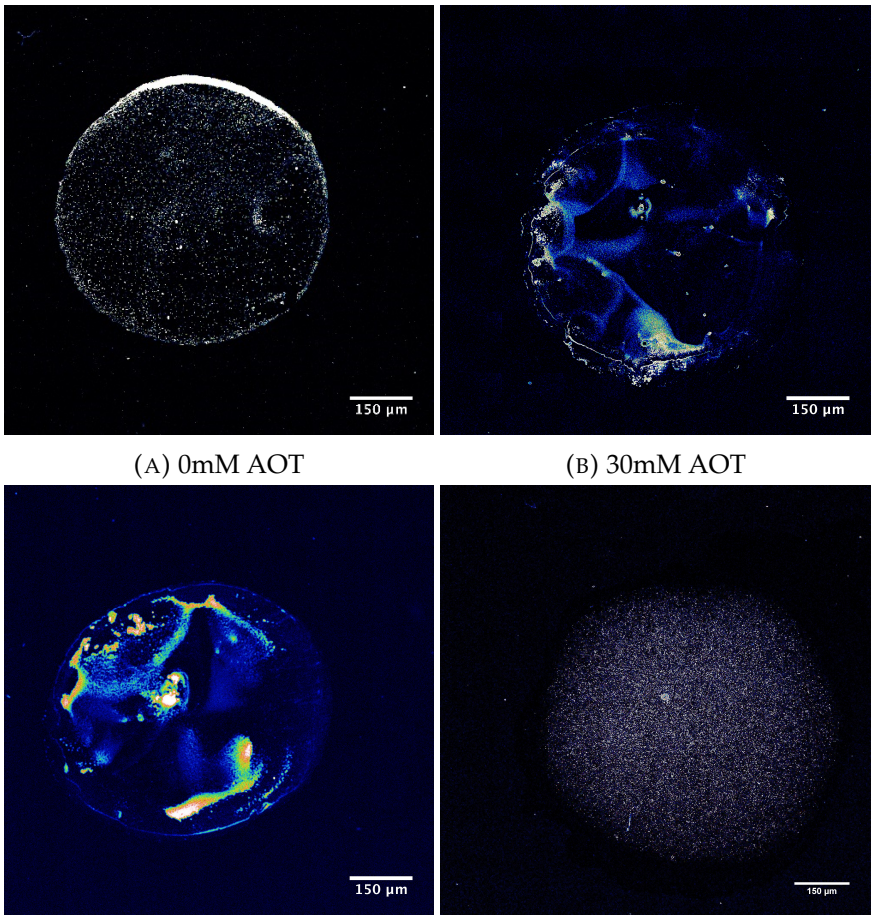

(A) 0mM AOT (B) 30mM AOT

(C) 40mM AOT (D) 100mM AOT

FIGURE 5.20: Deposition patterns of evaporated dodecane droplets

subsection, hexane is highly evaporative and the drying process of hexane droplet is convection-dominant, hence leaving particles deposited at the edge and formed a fine ring. Figures 5.22a and 5.22b show the particles (PMMA and IM-PMMA) density profile with respect to the radial distance in the evaporated hexane droplets. Regardless of AOT concentration, we see the enhancement of particles density towards the droplet edge (r=R), which explains the formation of 'ring'-shaped pattern. The particles density value at the droplet edge tends to be maximum at all AOT concentration. However, with increasing AOT concentration, we noticed that the intensity of the density of the particles at r=R starts to reduce, indicating that AOT reduces the 'ring' intensity in hexane rather than inhibiting the contact line mobility as observed in dodecane droplets. This can be seen in Figure 5.23 where the intensity of the 'ring' reduces with AOT concentration, despite the 'ring' pattern is observed in all hexane systems. The k_{cl} value in evaporated hexane droplet is always ~ 1 as the evaporation of the system is dominated by a thermodynamic process. From Figure 5.22b, the density profile across the droplet radius behaves similarly for highly-charged IM-PMMA particles in hexane, but without any AOT, where the surface particle charge is maximum, we observed that the reduction in particles density at $r \geq 0.6$, indicating the formation of 'mountain'-shaped deposition pattern.

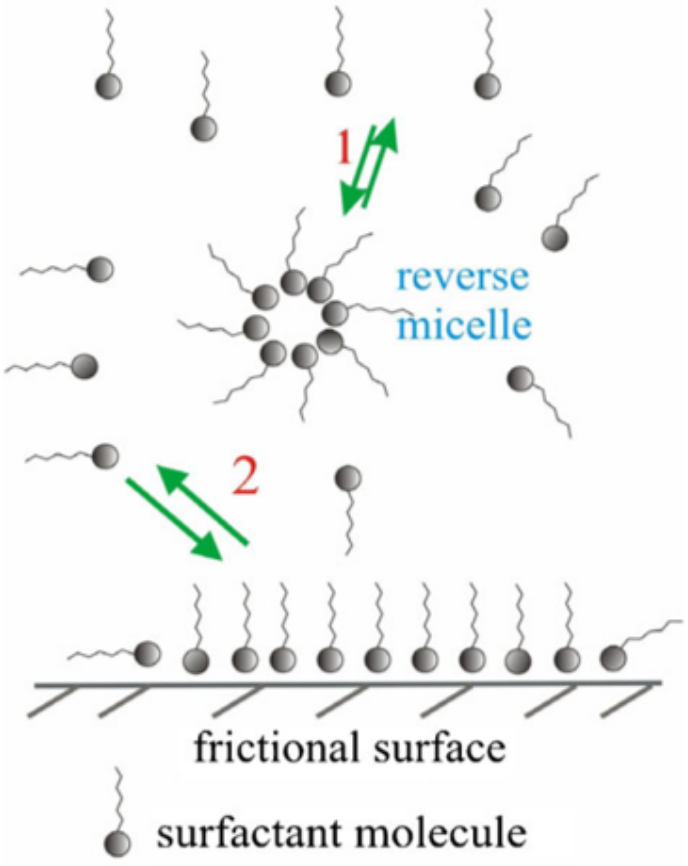

FIGURE 5.21: Equilibrium in solution containing surfactant molecules forming reverse micelle and adsorption on the solid surface (Margielewski and Płaza, 2010)

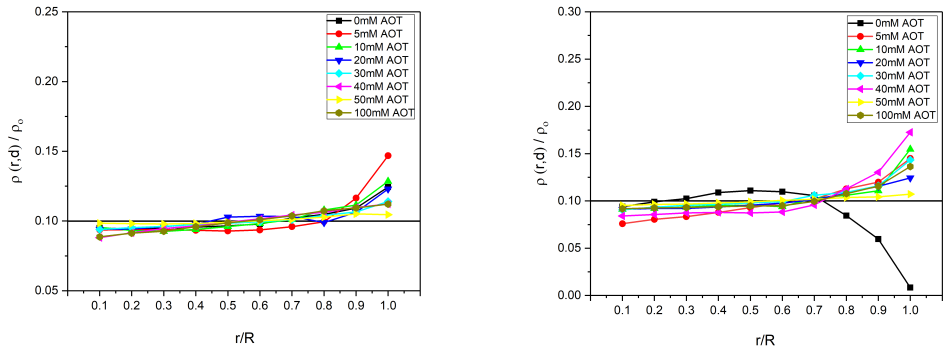

(A) PMMA (B) Highly-charged IM-PMMA

FIGURE 5.22: Particles density in evaporated hexane across the droplet radius with varying [AOT]

5.5 Summary

A uniform deposition pattern is favourable in industries which dealing with processes that involved evaporation such as inkjet printing, layering and coating. The

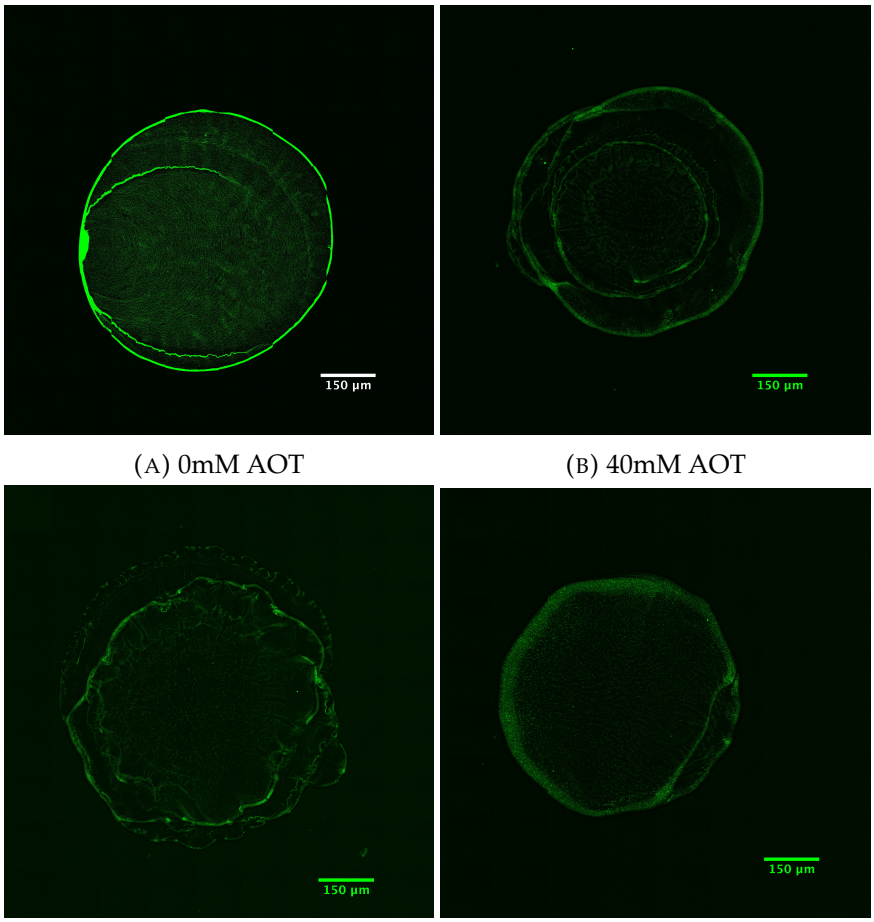

(A) 0mM AOT (B) 40mM AOT

(C) 50mM AOT (D) 100mM AOT

FIGURE 5.23: Deposition patterns of evaporated hexane droplets

need for non-aqueous solvents as the base medium for inks and pigments is demanding yet the non-uniform deposition pattern sometimes is unavoidable. The deposition patterns of evaporating colloidal droplets are mainly driven by the evaporation kinetics of the solvent. The precise comparison between the effect of fluid flow and interparticle interactions on the deposition patterns will be discussed in Chapter 5. Importantly, the Peclet number defines the mechanism of solvent transfer rate and then it is concluded that hexane droplets undergo convective driven evaporation and dodecane droplets follow the diffusional mechanism. Resulting in these, hexane droplets produced fine rings when evaporated despite the concentration of AOT added while AOT concentration has significantly affected the deposition pattern of PMMA in dodecane droplets. The contact line friction coefficient, known as k_{cl}, which altered by AOT concentration reveals that the mobility of the contact line can be enhanced by increasing [AOT] in dodecane. This leads to the transition of 'ring'-like pattern to the 'volcano' and subsequently to the 'mountain'-shaped deposition pattern, which resembles the uniform deposition pattern.

Chapter 6

Evaporation of Colloidal Droplet: Role of Intercolloidal Forces

This chapter is a continuation from Chapter 5 and focuses on the role of intercolloidal interactions on the deposition pattern of an evaporating colloidal droplet. The intercolloidal interactions, namely attraction and repulsion are both vital in yielding a uniform deposition pattern. We will also relate and discuss the observation and experimental results with relevant theories. Finally, we will compare two vital factors in determining the uniformity of an evaporating colloidal droplet, namely the evaporation kinetics and interparticle interactions.

6.1 Particle-Particle Interaction

6.1.1 Background

In most work performed on the evaporation of colloidal droplet, the interparticle interaction is often neglected due to its negligible effect on the deposition patterns of the droplet containing colloidal particles compared to evaporation kinetics, as claimed by most researchers. It is indisputable that the particle-substrate interaction is vital in determining the final deposition pattern of an evaporating droplet, but it is also known that particle-particle interactions has a crucial role too. As an example, we take the evaporation of an ink solution. The ink formulation is composed of colloidal particles, either solid pigment particles or molecular dyes, the interparticle behaviour and stability of these substituents in the suspension is paramount to determine the final properties of the ink formulation (Hoath, 2016). Colloidal ink suspensions are normally prepared by dispersing pigment particles of $\sim$ 50 to 100 nm to produce a stable dispersion. However, these inks need to be stabilized against aggregation and sedimentation. Therefore surfactants and polymers are commonly used as a part of the ingredients in preparing a stable ink dispersion (Hoath, 2016; Koo et al., 2006).

This chapter discusses the role of particle-particle interactions in an evaporating colloidal droplet and how it affects the final deposition pattern of the evaporated droplet. Two substituents were used to alter the interaction between microspheres in non-aqueous solvents, namely AOT surfactant and TDAT organic electrolyte. The underlying theory and background of the TDAT electrolyte-induced attraction in bulk solution have been explicitly discussed in Chapter 3. In this chapter, we discuss mainly on the behaviour of AOT in a non-aqueous solvent and subsequently influence the final deposition pattern of an evaporating solute particles laden colloidal droplet.

6.1.2 DLVO interactions on the evaporation of colloidal droplet

When discussing the stability of colloids in a liquid, the classical Derjaguin, Landau, Verwey and Overbeek (DLVO) theory has a fundamental importance as it described the interactions between charged particles as thoroughly discussed in chapter 1. Since the theory was developed in the 1940s, it remains valid and useful to insight the interactions and stability of particles in an evaporating colloidal droplet.

In determining the pattern or organization of particles in a liquid, the electrostatic interaction is crucial and this interaction largely depends on the pH and ionic strength of the overall system. For instance, the structure of lipid and biomembranes change based on the pH and ionic strength of the system. By varying the pH and ionic strength, the transition from less ordered structure to more compact and ordered of lipid membranes was observed due to the tuning of electrostatic energy (Manning, 1972). This is due to the electrostatic repulsion between charged membrane surfaces. Träuble et al demonstrated that the expansion of charged dimyristoyl-MPA surfaces in water due to electrostatic free energy can modify the membrane structure. The tuning of electrostatic free energy from high to low can generate phase separation and condensation of the membrane structure (Träuble et al., 1976).

Bhardwaj and coworkers investigated the role of DLVO interactions on an evaporating water droplet suspended with titania particles. The electrostatic interactions between the particles and the solid substrate were controlled by varying the pH of the system (Bhardwaj et al., 2010). The electrostatic repulsion in this work was measured between titania particles while the van der Waals attraction was determined between the particles and the substrate. At the high and low pH, where the particles were highly negatively or positively-charged particles, they observed the formation of a 'ring'-like pattern and it originated from the repulsion between particles and the substrate. At intermediate pH, the surface charge of the particle is near to the charge neutralization and the electrostatic repulsion becomes less dominant and the attraction from the van der Waals interaction between the substrate and particles is relevant. The pH and ion concentration dependence on the surface

charge can be attributed to the dissociation of the surface group on the particles and this phenomenon is very unlikely in the non-aqueous systems as discussed in chapter 1 (Bhardwaj et al., 2010; Roberts et al., 2008). The paramount factors in determining charging phenomena in the solvent with known dielectric value are the Bjerrum length λ_B, where the coulombic interaction is compared to the thermodynamic equilibrium, and the Born energy, which correlates the permittivity of a solvent with Gibbs free energy of solvation of ions in bulk solvent (Jayaram, 1994).

The van der Waals (vdW) attraction between particles and particle-substrate are both crucial in finalizing the pattern of an evaporated droplet. Dugyala and coworkers measured both interaction potentials of hematite particles in water and found that at a high van der Waals interaction (reduced repulsion), with high Hamaker constant value, small particle aggregates formed in the bulk which tend to attract to the glass surface and the particle-substrate interaction is further aided when the glass substrate is strongly negatively-charged (Dugyala and Basavaraj, 2014). This shows that the equilibrium between particle-particle interaction in the bulk and particle-substrate affinity can be critical in manipulating the deposition pattern of an evaporating droplet. Fundamentally, the uniformity of the deposition pattern can be tuned by reducing the strength of electrostatic repulsion, and later in this thesis, we will prove that both electrostatic repulsion and attraction can potentially yield a uniform deposition pattern.

Lebedev-Stepanov and Vlasov performed a theoretical study on the particle dynamics in an evaporating colloidal aqueous droplet (Lebedev-Stepanov and Vlasov, 2013). As most works performed to investigate the interactions between particles and particle-substrate in the system, they took DLVO interactions into account. If the electrostatic repulsion barrier is small, the particles tend to form aggregates and clusters, subsequently adsorbed on the substrate (Figure 6.1). From a study of inkjet printing on a substrate, the domains and clustering are formed as a result of a competition between electrostatic repulsion between particles and particle-substrate and also the capillary compression due to the reduction of the droplet height and volume as the evaporation process takes place (Park and Moon, 2006).

6.1.3 Non-DLVO interactions on the evaporation of colloidal droplet

In most cases, the failure of van der Waals attraction and electrostatic repulsion forces outlined by DLVO theory is originated when two surfaces approach each other closer than a few nanometers. When particles are interacting at a very small separation, the interacting forces can be larger than the ones described in DLVO interactions and these forces are mostly referred to as non-DLVO interactions. The most common non-DLVO forces are solvation (attractive hydrophobic and repulsive hydration) and steric forces. These forces obviously have a significant effect in the

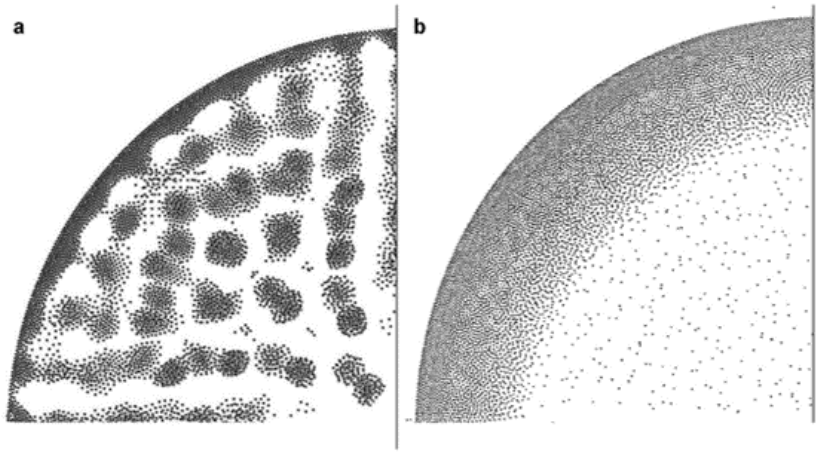

FIGURE 6.1: Particle clustering due to low electrostatic energy barrier (Left) and strong electrostatic repulsion prevents particle clustering (Right) (Lebedev-Stepanov and Vlasov, 2013)

ordering and structuring of the colloidal particles and hugely affect the deposition patterns of an evaporating colloidal droplet (Israelachvili, 2011).

In an aqueous colloidal droplet, using negatively charged particles, polystyrene-g-acrylic acid (PS-AA), two oppositely charged surfactants were used to alter the surface charge, namely CTAB (cationic surfactant) and SDS (anionic surfactant). For the like-charged system, PS-AA with SDS surfactant, the particles repel each other and the electrostatic repulsion was also observed between the particles and the glass substrate, hence yielding the formation of the 'ring'-like pattern when the solvent is fully evaporated (Anyfantakis and Baigl, 2015). As the authors altered the surface charge of the particles with CTAB surfactant decorating on the surface, a surface charge neutralization is achieved when the number of counterions is similar to the number of available charge sites. These neutral particles occupy at the liquid-gas interface due to the hydrophobic effect as interpreted in Figure 6.2. At the point of neutralization, the polar particles become non-polar and the net surface charge is zero, thus interacting hydrophobically in polar solvent (Tanford, 1962). When the solvent in the droplet was fully evaporated, the particles form a uniform deposition pattern. Hydrophobic interaction has been a well-known interparticle interaction where hydrophobic bonds spontaneously form between nonpolar groups in order to minimize their contacts with water, thus forming aggregates and clusters (Tanford, 1980; Ben-Naim, 2012). The addition of an electrolyte and salt into this system enhances the formation of aggregates. In the case of aggregation of molecules due to physisorption such as surfactants, a number of techniques such as AFM and SFA proved that the long-ranged attraction originates from molecular arrangements resulting in an electrostatic response between hydrophilic surfaces with patches of negative or positive side (Meyer, Rosenberg, and Israelachvili, 2006). However, in a non-aqueous solvent or oil, the hydrophobic interaction is not observed, simply as amino acid molecules will not be coiled up in oil as they do in water (Chandler,

2002).

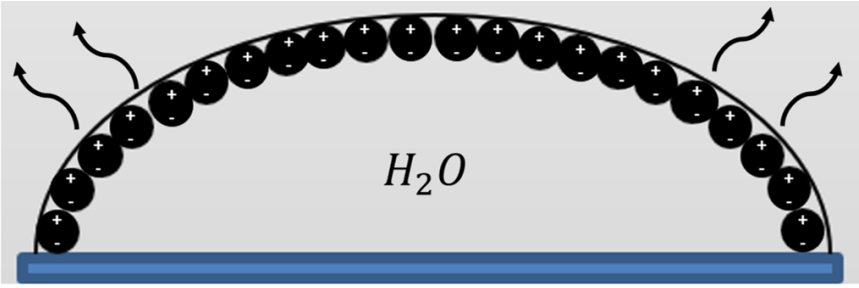

FIGURE 6.2: Interpretation of neutral particles occupying at the droplet interface in water due to the hydrophobic interaction. The + and - signs indicate the neutrality of the particles. Complete evaporation of water resulted to a uniform deposition pattern.

Polymers are commonly used to aid the suppression of 'ring'-liked deposition pattern in an evaporating colloidal droplet. These polymeric materials do not just alter the 'coffee-ring' effect by its viscosity but also the interaction on the interfaces in liquid. Seo et al. compare the effect of adding SDS surfactant and poly(ethylene glycol) (PEG) in a particles-laden aqueous droplet. They found that adding PEG enhances the balance flow between outward capillary and Marangoni flows, thus suppressing the formation of a non-uniform deposition pattern (Seo et al., 2017). The entropic- driven depletion interaction between polymers and colloids is not necessarily suppressing the 'ring'-like pattern. The flocculation and aggregation of colloids depends largely on the colloid size, hence affecting the deposition patterns of an evaporating droplet differently. Small colloids (r<1 μm) have more tendency to form clusters compared to the large ones (r>1 μm) (Ryu et al., 2017). In order to obtain an effective depletion attraction, the size of the polymer must be ordered with the size of the colloid (Tuinier, Rieger, and De Kruif, 2003; Lekkerkerker and Tuinier, 2011). The concept of adding polymer in a colloidal system is normally biased to the formation of depletion interactions, which induce attraction between colloidal particles as particles attraction is a well-discussed interparticle interaction effect to suppress the 'coffee-ring' pattern. The repulsion between two steric material-decorated surfaces is mainly due to unfavourable entropy related to the polymeric chains on the surfaces as they become confined and overlapped. This is referred to as a steric stabilization of colloids where polymers are added to reverse coagulation (Israelachvili, 2011).

6.2 AOT surfactant on particle charging

As mentioned in Chapter 1, surfactants are generally used to generate the charge on the particle surface in a non-polar colloidal system. In this work, AOT was added to both hexane and dodecane systems using PMMA and IM-PMMA colloidal particles.

In non-polar solvents, AOT molecules form inverse micelles, with the polar head aggregating in the middle of the micelle and long-chain hydrocarbon tail extending in the bulk. The mechanism of charging phenomena in non-aqueous solvents is still uncertain and there has been a number of proposals describing the charging process. AOT was used to facilitate charging of colloidal particles in oil and the plausible mechanisms are explained by Morrison (Morrison, 1993):

- (A) As the surfactant is added into the non-aqueous system, the individual surfactant molecular ions form aggregates and eventually, charged micelles form. These entities are adsorbed on the particle surfaces, thus affecting the net surface charge.
- (B) The transfer of the molecular ions into the reverse micelles core result from the entropy and kinetics of dissociated surface group.
- (C) Adsorption of surfactant aggreggates and micelles onto the particle surface and the formation of ion complex with the surface group and subsequent exchange and desorption of the molecular ions into the solution micelles.

In a decane system containing slightly negatively-charged silica particles, the magnitude of the charge increased with AOT concentration, until the surface charge reached a maximum negative value at 0.1mM of AOT. Charge reversal was observed at a high AOT concentration and the magnitude went to a maximum positive value at 100mM of AOT. This is predominantly due to the competition between the surface binding of the sulfosuccinate anions of AOT at low concentration and positively charged species at high concentration (Keir et al., 2002). The charging of particles in non-aqueous solvent arises from a site model as described in mechanism (A) by Morrison and it was proven to be useful in the charging behaviour of toner particles using non-aqueous solvent in inkjet printing. For mechanism (A), at low concentrations of AOT, the surfactant molecules dissolve in the non-aqueous solvent and initially exist as single molecules or monomers, then form aggregates of molecules such as dimers or trimers and these species are referred to as premicellar species (Eicke, Hopmann, and Christen, 1975). Below the CMC, there is an equilibrium between these species. The collision of premicellar species in non-aqueous solvent induced a charge transfer via sodium ion of AOT, yielding positively and negatively charged species and the process can be described as below.

$$n(AOT) \rightleftharpoons M \tag{6.1}$$

$$M + M \rightleftharpoons M^{+} + M^{-} \tag{6.2}$$

n is the number of AOT molecules, M is the neutral premicellar AOT aggregate while M^+ and M^+ are positively and negatively charged premicellar aggregates respectively. These charged species can adsorb onto the particles surface and at very low concentration regime, the negatively-charged premicellar species are more prone to be adsorbed on the surface via acid-base interactions. The mechanism can be described as:

$$S + M^- \rightleftharpoons SM^- \tag{6.3}$$

where S is the neutral particle surface and SM^- is particle surface anchored with negatively charged species, making the particles having negative charge. In the electrical double layer, the excess positively-charged species M^+ start to neutralize the negatively-charged particle surface, due to the anchoring of negative-charged premicelles. The adsorption process continues until all the negative-charged species on the surface were neutralized and the process can be represented as:

$$S + M^- M^+ \rightleftharpoons SMM \tag{6.4}$$

The adsorption of positively-charged species continues to increase and decorate the surface charge and it can be described as:

$$S + M^+ \rightleftharpoons SM^+ \tag{6.5}$$

and this is likely to be a positively-charged micelle. The negatively charged headgroup of AOT molecules, AOT^- become the counterions and form an electrical double layer around the particle surface. The particle surface becomes overcrowded with counterion dissociated from AOT molecules with increasing AOT concentration and some of the counterions were very close promixity to the positively-decorated surface and eventually neutralize the surface yielding SM-AOT as below (Keir et al., 2002):

$$SM^+ + AOT^- \rightleftharpoons SM - AOT \tag{6.6}$$

Hsu and coworkers proposed that the dependency of the particle charge on AOT concentration is a consequence of a change in charging mechanism, which is the dissociation of the surface group (mechanism B), rather than the adsorption of ionic species on the particle surface, which is commonly discussed in the case of AOT-induced charging (Hsu, Dufresne, and Weitz, 2005b). They also mentioned that the surface potential is independent of AOT concentration and determined by

electrokinetics and direct interaction measurements. In a system with lower AOT concentration (<CMC), the particles manifest no response to electric field and when reverse micelles present, the colloids move in an opposite direction of the electric field, indicating that the particles are negatively charged.

Roberts et al. re-examined the charging mechanism of PMMA stabilised with PHSA layer in low dielectric solvents, aided with AOT and $Zr(Oct)_2$ surfactants using single-particle optical microelelectrophoresis (SPOM). They outlined that the magnitude of charging in non-aqueous colloidal system is independent on the number of micelles added, over a wider concentration range of AOT. The particle charge is essentially generated thermodynamically by the competitive adsorption between positively and negatively charged micelles on the particle surfaces (Roberts et al., 2008). Our investigation on the deposition patterns affected by the electrostatics in the bulk induced by AOT is based on the study performed by Roberts and coworkers.

6.2.1 Conductivity and debye screening length of AOT solution

In solution, the neutral uncharged reverse micelles exist in a dynamic equilibrium. The exchange between mobile ions in solution and the hydrophilic core of reverse micelles occurred when the micelles collide with each other, due to thermal fluctuation and consequences to the fluctuating net charge of each micelle. This is due to the nature of non-aqueous solvents. The investigation on the charge fluctuation model for conductivity has been extensively studied by Eicke et al. based on the water-in-oil microemulsion (Eicke, Borkovec, and Das-Gupta, 1989). For a microemulsion system; a system containing oil, water and surfactant, the amount of water in the oil determines the radius of nanodroplet formed in oil and the conductivity value of the microemulsion. This indicates that the nanodroplets carries excess charge species, either positive or negative, and the specific conductivity value rises due to the migration of these charged species under the application of an electric field (Eicke and Denss, 1979). The conductivity value immediately implies to the number of charge in the droplet. From the correlation of the conductivity, number density of ions and charge, if each droplet typically carries 10^4 ionic surfactant molecules, each droplet would carry 10^2 elementary charges as $\rho_{ion} \propto \sqrt{e}$.

To explain the effect of ion concentration and the role of AOT in the screening of electrostatic interactions, we calculate the independent values of ion concentration, conductivity and debye length without colloidal particles based on Roberts et al and Hsu et al. As discussed in Chapter 1, the Bjerrum length λ_B,

$$\lambda_B = \frac{e^2}{4\pi\epsilon_r\epsilon_o k_B T} \tag{6.7}$$

can be simply defined as when the strength of electrostatic interaction between two point of charges is comparable to the thermal energy k_BT. We know that the λ_B of dodecane and hexane are 28 and 29.4 nm respectively. A micelle of radius r carrying an excess charge ze possesses an electrostatic energy $\beta U_{el}(z) = z^2\lambda_B/2r$ where $\beta = (k_BT)^{-1}$. The net charge carried by each micelle fluctuates with time when the charges freely exchange between micelles. Since $U_{el} \propto z^2$, the number of multiple-charged micelles is significantly smaller than the number of singly-charged micelles and if the radius of charged micelle is smaller than λ_B (r$< \lambda_B$), the concentration of multiple-charged micelles can be ignored, considering that only monovalent micelles exist in the solution as the magnitude of βU_{el} is high (Roberts et al., 2008). From the charge exchange reaction through charge fluctuation and thermodynamic collision,

$$A + A \overset{k}{\rightleftharpoons} A^+ + A^- \tag{6.8}$$

where A is the uncharged micelle, A^+ and A^- are positively and negatively charged micelle respectively. The equilibrium constant k can be written as:

$$k = \frac{n_+.n_-}{n_o^2} \tag{6.9}$$

where n_+, n_- and n_o are the number densities of positively charged, negatively charged and uncharged micelles respectively. The value of $n_+ = n_- = n_{ion}$ due to practical absence of free ions in the solution. We calculated the density of AOT micelles and charged micelles formed in dodecane with respect to AOT concentration based on Roberts et al. and Hsu et al., with the fraction charged micelle $\chi_{micelle} = n_{ion}/n_o = 1.2 \text{ X } 10^{-5}$, where n_{ion} and n_o is the number density of charged micelles and total micelles respectively and it can be represented in Figure 6.3. The value of $\chi_{micelle}$ is independent of AOT concentration. The fraction of charged micelle can also be written as $\chi_{micelle} = 2\sqrt{K}$ and the electrostatic potential energy of monovalent charged micelles is reduced to $\beta U_{el}(z) = \lambda_B/2r$, then rearranged to $\chi_{micelle} = 2 \exp[-\beta U_{el}]$.

The conductivity measurements determine the degree of charge fluctuations in solution and the conductivity K of a solution containing same-sized monovalent ions with radius r can be expressed as:

$$K = \frac{e^2 n_{ion}}{6\pi\eta r} \tag{6.10}$$

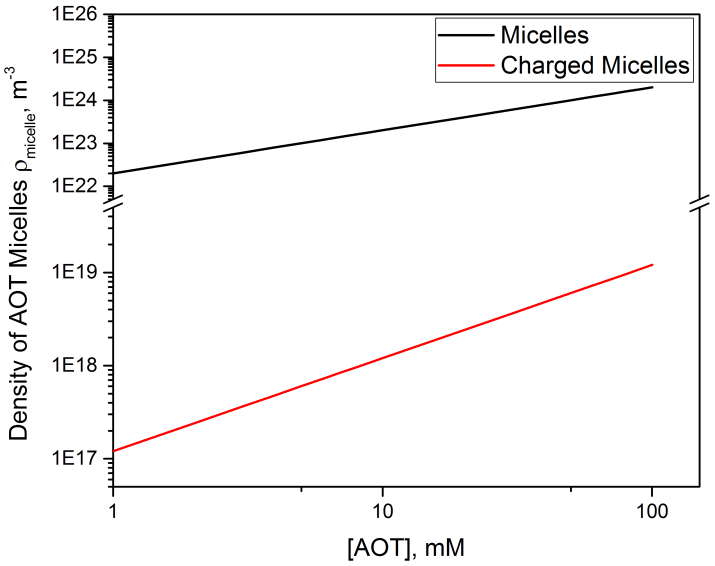

FIGURE 6.3: The density of micelles and charged micelles with respect to [AOT]

The denominator of the conductivity expression is referred to as the hydrodynamic friction of the micelles via Stokes equation $\xi = 6\pi\eta R_H$, where R_H is the hydrodynamic radius of the micelle. The number of ions here is referred to the number density of charged micelles and it can be calculated from the fraction of ionized micelles, given that the volume fraction $\varphi_{micelle} = n_o v_{micelle}$ where $v_{micelle}$ is the volume of micelle, then the conductivity expression in equation 6.10 can be rearranged to:

$$K = \frac{e^2}{6\pi\eta r v_{micelle}} \cdot \chi_{micelle} \varphi_{micelle} \tag{6.11}$$

The conductivity of pure solvent used in this work; dodecane and hexane is 6 order of magnitude lower than the conductivity of water (about 2 μScm^{-1}). Adding AOT at concentrations up to 100mM as depicted in Figure 6.4 increasing the range to about 2 order of magnitude. From the number density of ions present with respect to AOT concentration, we can calculate the Debye length κ^{-1},

$$\kappa^{-1} = (\sqrt{4\pi\lambda_B n_{ion}})^{-1} \tag{6.12}$$

The dependency of the Debye screening length with the number of charged AOT micelles is depicted in Figure 6.5. From the plot, it is shown that these charged micelles are interacting at a long range with the value of Debye length ranging from 0.3 to 3 μm.

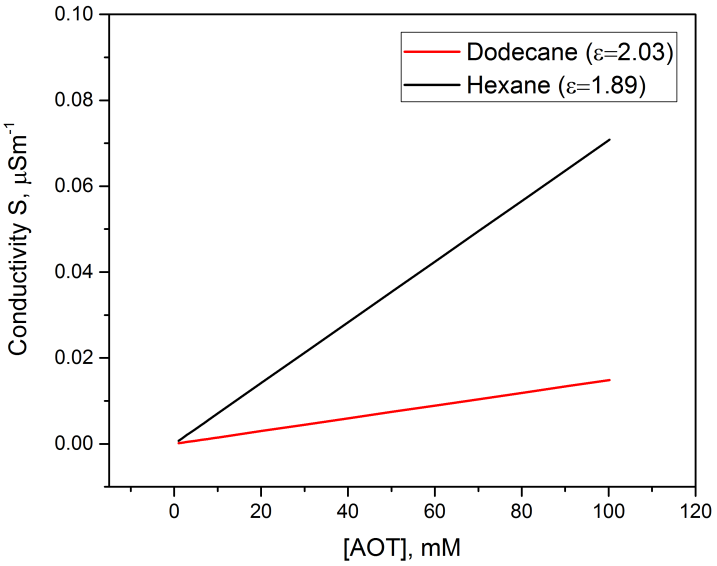

FIGURE 6.4: Conductivity of AOT solution in dodecane and hexane

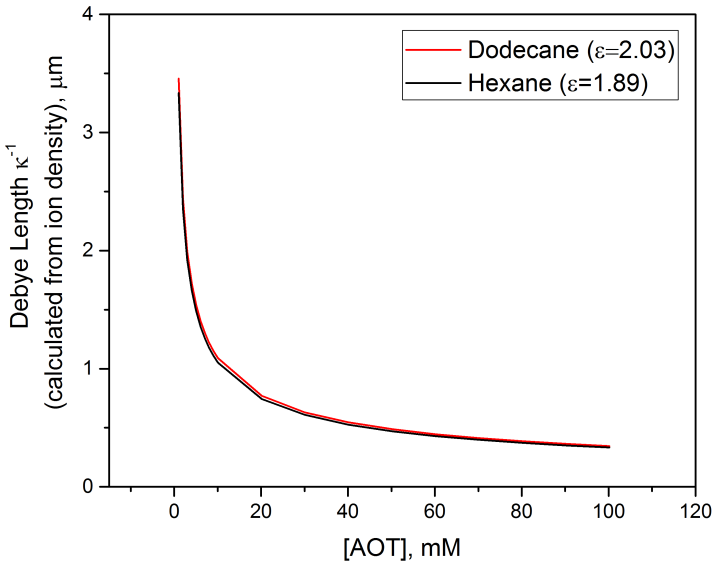

FIGURE 6.5: Debye screening length of AOT solution in dodecane and hexane

6.2.2 The adsorption of AOT on PMMA and the charging of particles

The adsorption of AOT surfactant on the PMMA surface has been measured by Kitahara and coworkers. At low concentrations of AOT, the adsroption increases abruptly with AOT concentrations, suggesting that the high affinity of AOT on the

PMMA surfaces before the plot reaches a plateau at high AOT concentrations (Kitahara, 1998). There are several methods to find how AOT molecules are adsorbed on the PMMA surface. Smith el al. performed small-angle neutron scattering (SANS) measurements of nano-sized sterically-stabilized PMMA with AOT (Smith et al., 2015). They found that AOT is adsorbed into the PHSA-PMMA latex cores as the normalized SANS measurement shows no difference between PMMA particle with PMMA/AOT system in dodecane. The adsorption of AOT into the latex core is due to the colloid core sometimes is considered as a 'solvent', in which it can be penetrated by small molecules. If this justifies that there is no adsorption of AOT on the PMMA surfaces, the addition of AOT will not enhance the charging effect of the particle. On a contrary, Roberts et al. used electrokinetics to determine the adsorption of AOT on the PMMA surface. Theoretically, when the charged AOT reverse micelles are adsorbed on the PMMA surfaces, the number of free charged micelles in solution must decrease (Roberts et al., 2008). Conductivity measurements were made on systems with constant colloid volume fraction and increasing AOT volume fraction. Due to the low conductivity value of non-polar solvent, a fixed amount of water was added to increase the number of reverse AOT micelles and from SANS measurement, it is confirmed that the radius of micelles is fixed and independent of AOT concentration. The resulting dispersion with a conductivity value K_d is the total sum of the motion of charged particles with associated diffuse layer of counterions K_p and the excess micellar ions in the solution K_∞, $K_d = K_p + K_\infty$. The solution containing particles and AOT micelles were centrifuged and the sedimented particles were separated and the conductivty of the supernatant is equal to the conductivty of free charged micelles in the solution K_∞. The conductivity of the particles was then calculated from the difference of conductivty of dispersion and free charged micelles, $K_d = K_d - K_\infty$.

From Figure 6.6, it is shown that at low AOT micelle volume fractions ($<$ 0.005), there are no charged micelles left as the conductivity of the supernatant (free charged micelles) K_∞ is zero. The conductivity of dispersion K_d increases rapidly with AOT micelle volume fraction $\varphi_{micelle}$ and the diference between K_d and K_∞ yields K_p. The dependency of the conductivity to the volume fraction AOT and the rapid increase of conductivity of low concentration indicate that the affinity of AOT on the particle surface. Wholly, this explains that the particles charged by the adsorption of charged micelles.

The mechanism of particle charging by surfactants in nonpolar dispersions has been extensively studied over the years. However, there is no clear line to justify which mechanism is favoured due to the low permittivity of the non-aqueous solvent. As discussed, the oil-soluble surfactant is widely used to induce the particle charging in non-polar media by incorporating single ions in the hydrophilic core of the surfactant inverse micelle. This molecular arrangement reduces the ionic Born

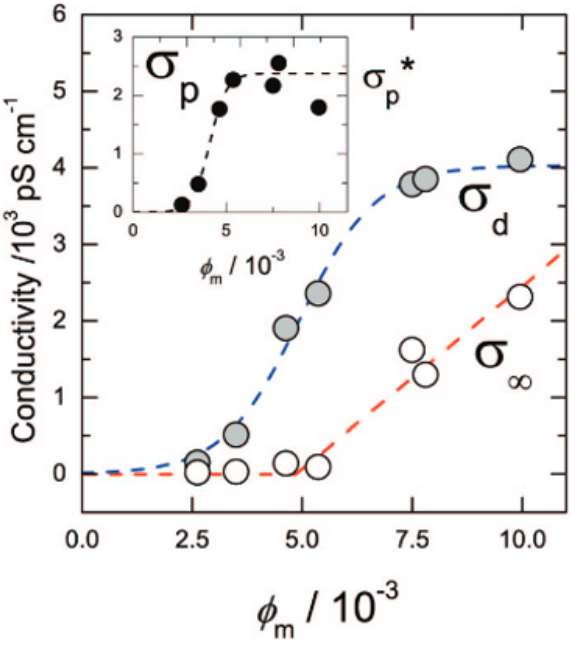

FIGURE 6.6: The conductivity of dispersion containing PMMA particles and AOT in decane as a function of swollen AOT reverse micelle volume fraction. The conductivity of the dispersion is denoted as σ_d and the conductivity of the free micellar ions is σ_∞. The conductivity of the particle with associated diffuse layer of counterions σ_d is calculated from σ_d and σ_∞ (Roberts et al., 2008). The symbol of conductivity in this thesis is referred as K and volume fraction is φ.

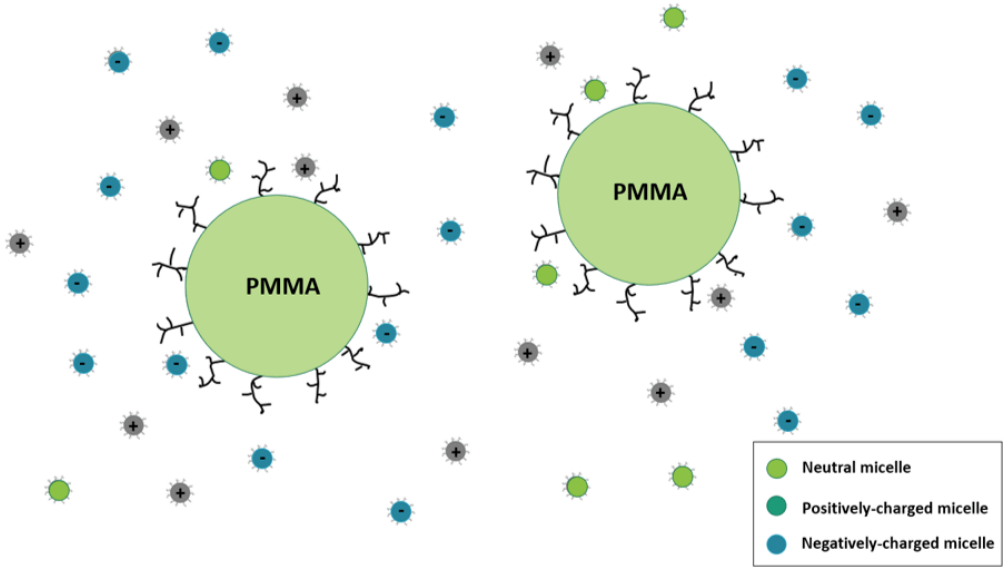

FIGURE 6.7: Presentation of uncharged and charged AOT micelles near PMMA-PHSA surfaces

energy by increasing the permittivity of the localised ion (Strubbe et al., 2006). Figure 6.7 illustrates the presence of neutral charged, positively and negatively-charged micelles decorated near the PMMA-PHSA particle surface. We predict the charging mechanism for our nonpolar system is based on the competitive adsorption of

charged micelles on the particle surfaces.

6.2.3 Electrokinetic Phenomena and Particle Surface Charge

The electrokinetic properties of charged particles depend on the surface potential and diffuse double layer formed on the charged particle surface. In a liquid suspension containing charged colloidal particles with applied electric field, the exerted field will drive the particles in the liquid with a force balancing the viscous drag on the particles. In a stationary position, both electric field and viscous drag forces are balanced with each other so that the colloids are able to move with a constant velocity in a liquid. The mobility of charged particles induced by an electric field is known as electrophoresis (Hunter, 2013; Ohshima and Furusawa, 1998; Ohshima, 2006b; Gillespie, 2016). The electrophoretic velocity for a single charged colloidal particle of radius a in response to an applied electric field E can be calculated by balancing the Stokes frictional resistance (drag force), F_d (left hand side of the expression) and electric force acting F_E (right hand side) on the particle, ($F_d = F_E$) with solvent viscosity η,

$$6\pi\eta a v_e = ZeE \tag{6.13}$$

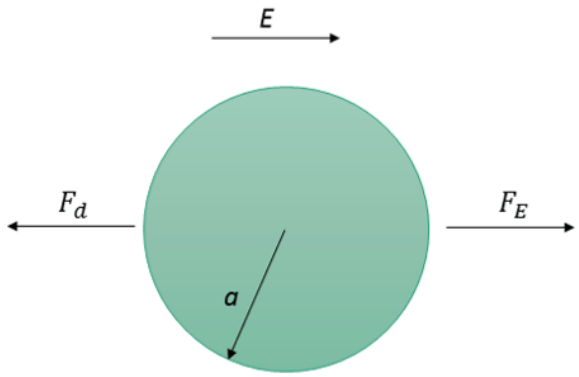

FIGURE 6.8: Schematic of a charged particle with radius a with the balance of drag force f_d and electric force F_E

The electrophoretic mobility μ_e can be expressed as,

$$\mu_e = \frac{v_e}{E} \tag{6.14}$$

and finally the electrophoretic mobility can be correlated with the charge Z as,

$$\mu_e = \frac{Ze}{6\pi\eta a} \tag{6.15}$$

This expression can be used to calculate the charge for a system without any salt, obeying H*ü*ckel limit considering that the particle radius is much smaller than the Debye length κ^{-1}, $\kappa a \ll 1$. For our system with AOT with Debye length of 1 μm, the $\kappa a \sim 0.25$. The electokinetic (zeta) potential ζ can be expressed as,

$$\zeta = \frac{Ze}{4\pi\epsilon_r a} \tag{6.16}$$

and the zeta potential and mobility can be correlated as,

$$\mu_e = \frac{2}{3}\frac{\epsilon_r}{\eta}\zeta \tag{6.17}$$

where ϵ_r is the relative permittivity of the solvent and the reduced electrostatic potential ψ_{red} can be calculated by averaging the electrostatic potential ϕ with the thermal energy $k_B T$, yielding,

$$\psi_{red} = \frac{e\phi}{k_B T} \tag{6.18}$$

The reduced zeta potential ζ_{red} is used when considering electrostatic screening close to the particle surface and this defines the bare surface charge Z. The reduced zeta potential or charge (effective charge Z_{eff}) then can be expressed as,

$$\zeta_{red} = \frac{e\zeta}{k_B T} \tag{6.19}$$

$$Z_{red} = \frac{Ze}{4\pi\epsilon R}\frac{e}{k_B T} = \frac{Z\lambda_B}{a} = Z_{eff} \tag{6.20}$$

We see the effect of AOT on the effective charge of PMMA and IM-PMMA in both dodecane and hexane, calulated from electrophoretic mobility measurements. From Figure 6.9, the effective charge for PMMA in dodecane and hexane varied with AOT. The particles possess a signicant amount of positive charge without any AOT and at about 5 mM of AOT, the effective charge reached the surface charge neutralization or (the point of zero charge (PZC)). As AOT was added at up to 20 mM, the particles were negatively-charged and the magnitude of effective charge plateaued until about 100 mM of AOT. Generally, similar to that trend observed in Figure 6.10 when IM-PMMA particles were used in hexane. Comparing the figures, without any

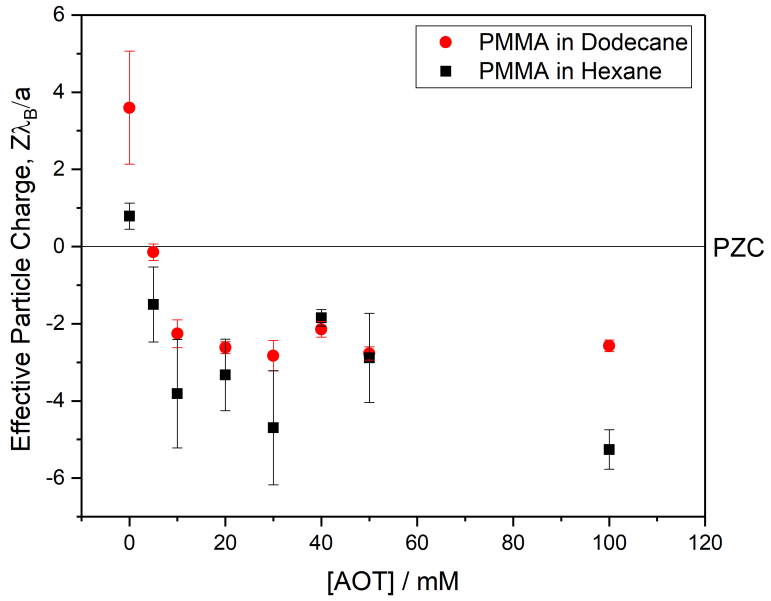

FIGURE 6.9: Effective Charge $Z\lambda_B/a$ of PMMA in dodecane and hexane varied with AOT concentration

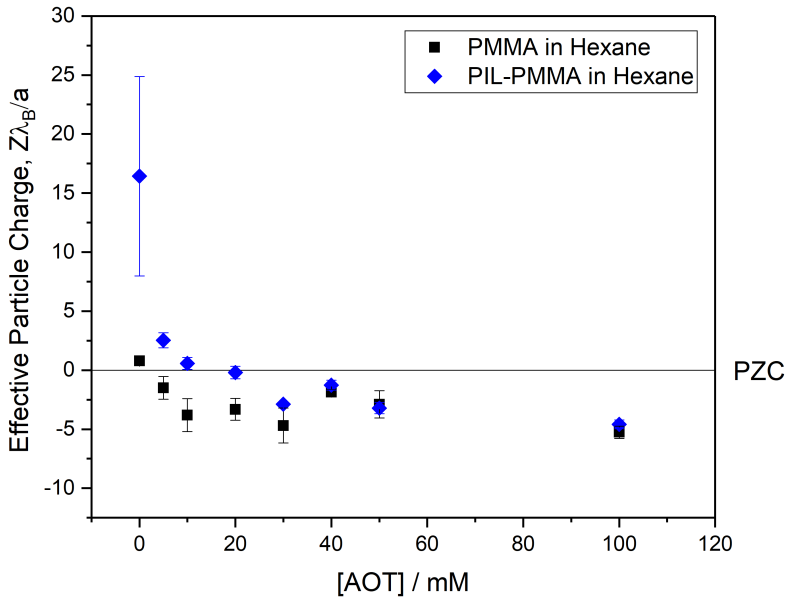

FIGURE 6.10: Effective Charge $Z\lambda_B/a$ of IM-PMMA in hexane varied with AOT concentration

AOT, the particles were highly positively-charged, about four times more charged than PMMA. This is due to the presence of ionic monomer group anchoring on the PMMA surfaces. We needed more AOT to neutralize the IM-PMMA system, reaching the PZC value at about 20 mM of AOT.

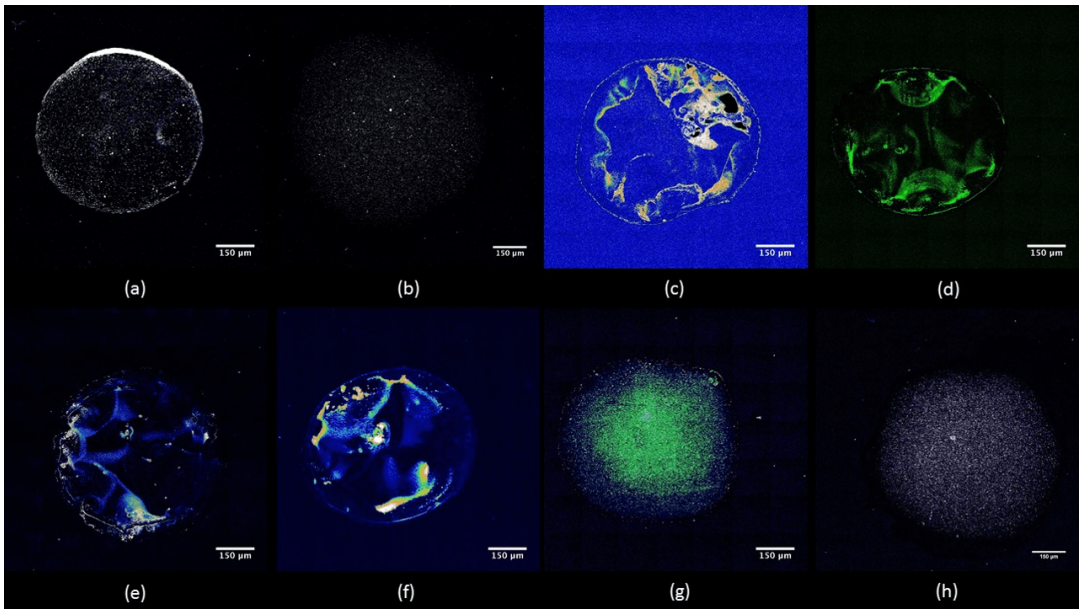

FIGURE 6.11: Deposition Patterns of PMMA colloids in dodecane with (a) 0mM AOT; (b) 5mM AOT; (c) 10mM AOT; (d) 20mM AOT; (e) 30mM AOT; (f) 40mM AOT; (g) 50mM AOT and (h) 100mM AOT

We relate the deposition patterns of an evaporating colloidal droplet with the charging phenomena we witnessed in the bulk affectED by the addition of AOT. As depicted in Figure 6.11, the concentration of AOT influenced the deposition patterns of the dodecane droplets. The effect of interparticle interactions on the deposition patterns was seen in dodecane droplets, but not in hexane droplets. This is due to the dominant effect of evaporation kinetics of hexane. However, we only used the highly-charged particle IM-PMMA in hexane, so we compare the effect of particle effective charge on the deposition pattern despite of the type of solvent, considering both solvents are similar in terms of electronic properties and Bjerrum length.

Figure 6.12 compares the number density of both PMMA in dodecane and IM-PMMA in hexane at the droplet edge, the region where $0.9 \leqslant \frac{\rho}{\rho_o} \leqslant 1.0$ or ρ_{ring}. If the number density of particle at all radial distance $\frac{\rho(r,d)}{\rho_o} = 0.1$, we see a uniform distribution for the deposit formed. Generally, we see that the particles density of PMMA/dodecane droplets with AOT were distributed below 0.1, $\rho_{ring} < 0.1$. Without any AOT, the PMMA particles in dodecane were fairly charged ($Z_{eff} \sim 3$) compared to IM-PMMA in hexane, with the magnitude of effective charge is four times larger. We can see that the number density of ring for IM-PMMA in hexane is below 0.1, despite the dominance of evaporation kinetics driving the particle migration towards the edge. It is seen that the contrast of the trend for dodecane and hexane droplets in Figure 6.12 The ring density for hexane droplets were always more than 0.1 ($\rho_{ring} > 0.1$), except for the system without any AOT, where the effective charge of the particles was enhanced.

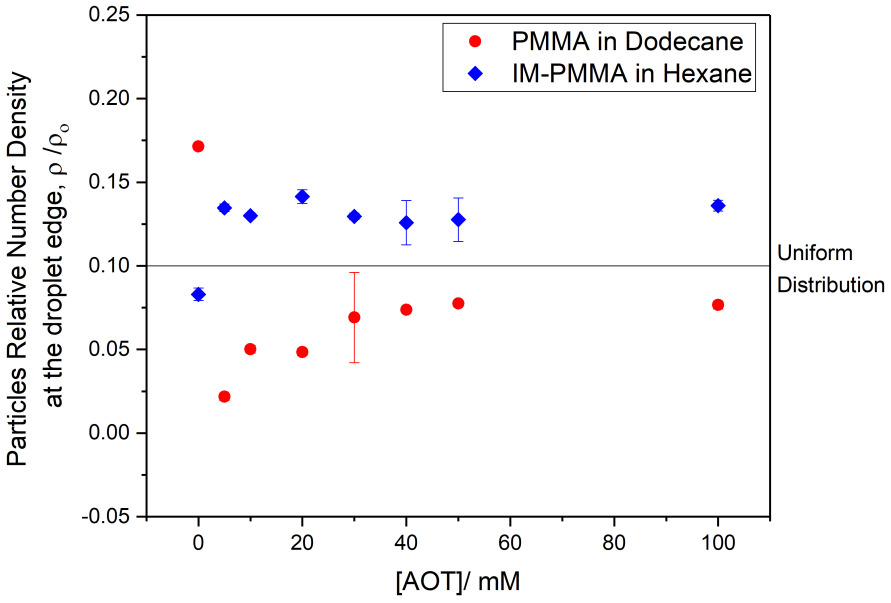

FIGURE 6.12: Relative Number Density of PMMA in dodecane and IM-PMMA in hexane at the droplet edge with varied AOT concentration

We postulate that the particle surface charge has largely influenced the deposition pattern of non-aqueous colloidal droplet. In most work concerning interparticle interactions, a highly-charged system triggered the migration of particles away from the the glass substrate, thus forming a 'ring'-liked pattern, but most of these works were focused on particle-substrate interaction rather than particle-particle interactions (Bhardwaj et al., 2010; Anyfantakis and Baigl, 2015). We consider our systems contain multi-particle rather than a single particle, thus interparticle interactions is a vital element determining the final deposition pattern of evaporating colloidal droplets. We confirm the magnitude of charge of both PMMA and IM-PMMA by comparing the fitted data from the measurement of force between two charged particles using blinking optical tweezer (BOT) performed by Finlayson and Bartlett (Finlayson and Bartlett, 2016). From Figure 6.13, the IM-PMMA is denoted as *LL* and PMMA particle is referred as *SS*. Here they compared the electrostatic potential energy between two particles and the differentiation of the energy with respect to distance yield the force between the particles with respect to distance between them. The interactions between two symmetric pair should behave in a purely Coulombic manner as there is no known electrolyte or salt in the non-aqueous solvent. Due to that, the Debye screening length cannot be measured and only a direct and simple Coulombic repulsion between particles observed (Finlayson, 2016a). The plot is generated from the derivation of repulsive DLVO energy,

$$U(r) = \frac{Z^2}{4\pi\epsilon_o\epsilon_r}\frac{exp(-(r-2a)/\lambda_D}{(1+a/\lambda_D)^2 r} \tag{6.21}$$

$$F(r) = -\frac{dU(r)}{dr} = \frac{Z^2}{4\pi\epsilon_o\epsilon_r}\frac{exp(-(r-2a)/\lambda_D}{(1+a/\lambda_D)^2}(\frac{1}{r^2}+\frac{1}{r\lambda_D}) \tag{6.22}$$

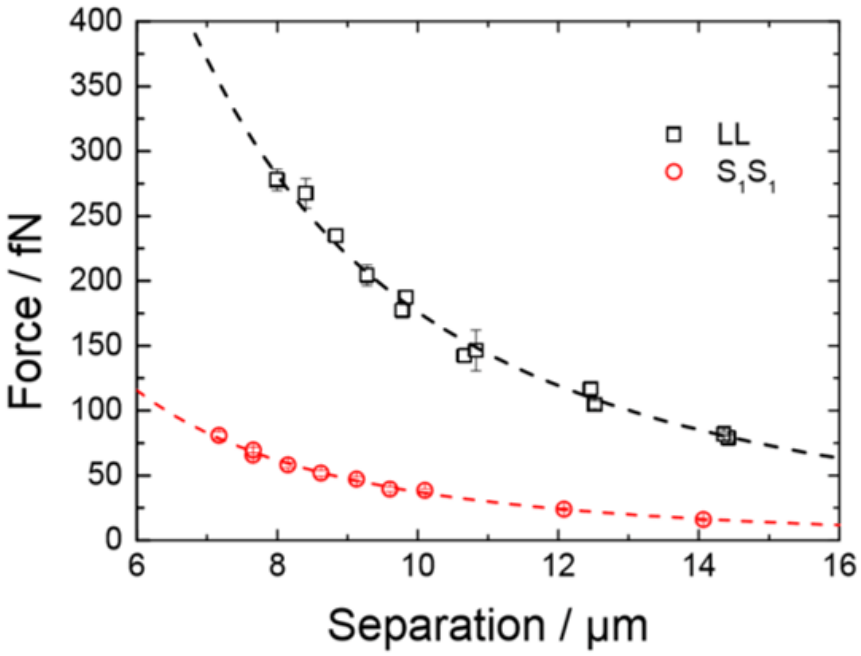

FIGURE 6.13: Force between two pairs of PMMA particles (S_1S_1) and IM-PMMA particles (LL) with respect to their separation (Finlayson, 2016a)

For IM-PMMA (denoted as LL) in Figure 6.13, it is clear than the pair are able to withhold a substantial amount of force when they were brought closer to each other due to the high electrostatic potential and the magnitude of force is about four times larger than PMMA particles (S_1S_1). Finlayson confirmed that for IM-PMMA (LL in Figure 5.11) system, the charge is independent of the separation between particles or the debye length, justifying the system is modelled as the constant surface charge (CSC) system (Finlayson, 2016a). From the conductivity measurement to investigate the ion density in the system, it is found that the density of ions is of the order of 10^{-9} mol m^{-3} compared to the systems with electrolyte in Chapter 3, where the ion density is higher by about 2 orders of magnitude (Finlayson, 2016a). This shows that the Debye length for IM-PMMA system is very long, indicating the particles are interacting over a very long range in a counterion only system. Bowen and Williams explained the dependency of electrostatic potential on the osmotic pressure Π of a bovine serum albumin (BSA) colloid in water. The osmotic pressure is highly dependent on the entropic pressure, and the repulsion between a pair of particles is mainly due to the overlapping of their diffuse layer hence, enhancing

the entropic pressure in the system. They used a range of pH to alter the electrostatics between the particles and they found that the osmotic and entropic pressures increased exponentially with the colloid concentration in the system (Bowen and Williams, 1996). The effect of pH in this case, contributes to the balance between electrostatic repulsion and van der Waals attraction of the system has significantly enhanced the osmotic pressure of between the interacting colloids at a higher colloid volume fraction as depicted in Figure 6.14.

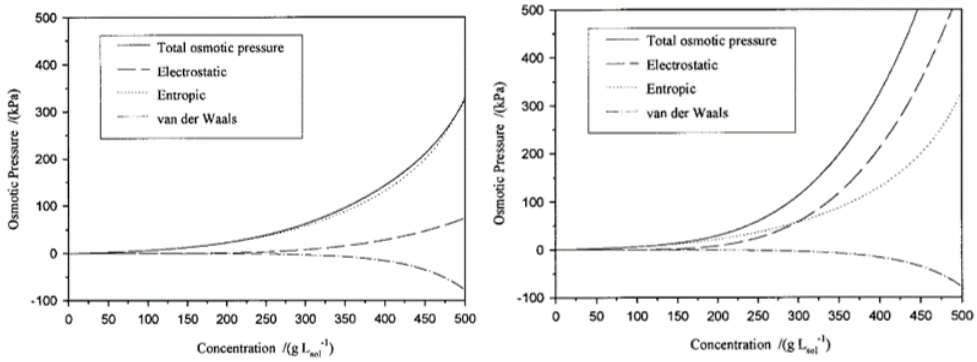

(A) pH=5.4 (B) pH=7.4

FIGURE 6.14: Contributions to the total osmotic pressure changes with concentration of BSA particle (Bowen and Williams, 1996)

Theoretically, a highly-charged dispersion contributes to a high electrostatic interaction and the particles are evenly dispersed throughout the solvent as depicted in Figure 6.15a and such configurations keep the particles away from each other, considering the surface charge is uniform throughout the surface area. However, this is observed when the particle volume fraction is high enough and the interaction between particles depends on the configurational entropy rather than the DLVO interactions, which are mainly applied to a dilute systems (Bowen and Jenner, 1995). The ordering of the particles reduces their degree of freedom in the solvent due to the transformation from repulsive forces due to high surface charges into the configurational electrostatic surface energy as discussed in Chapter 1. Assuming the particles are arranged in the hexagonal-closed packing (HCP) system (pictured in Figure 6.15); a particle surrounded by twelve nearest neighbouring particles which exist in a structure where the energy is minimum (Hiltner and Krieger, 1969). The relation of configurational electrostatic energy $\frac{dG}{dr}$ to the electrostatic force $f(D)$ can be expressed as,

$$-\frac{dG}{dr} = 12f(D)\frac{1}{2} \tag{6.23}$$

$$f(D) = \frac{1}{3}S_{cell}n^{o}kT(cosh\frac{ze\varphi}{kT} - 1) \tag{6.24}$$

We relate the evaporation process that takes place on a droplet containing

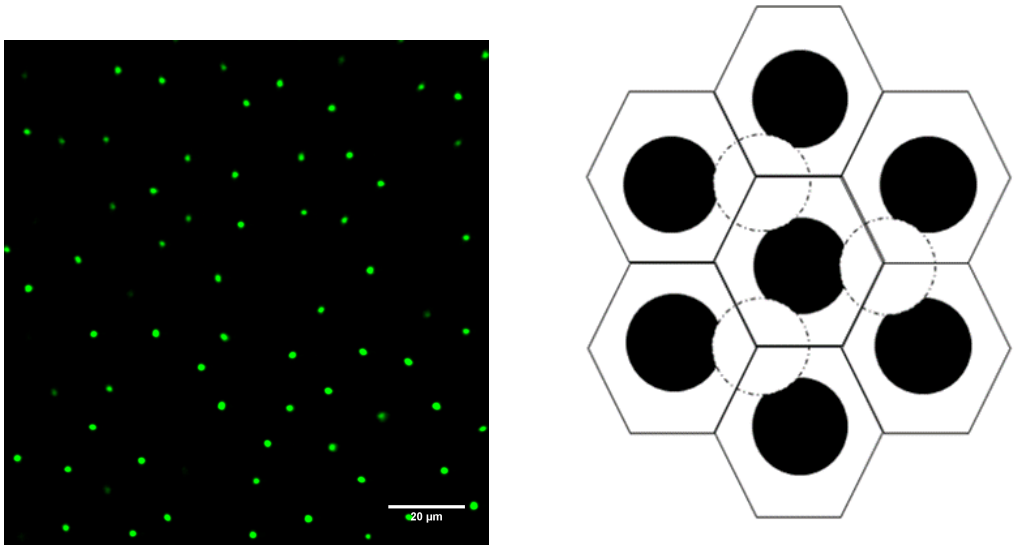

(A) Highly-charged particles in bulk solution evenly-spaced among each other

(B) Schematic presentation of a hexangonal-closed packed array

FIGURE 6.15: Comparison of a stable (highly-charged) dispersion with the HCP structure

highly-charged dispersion with the deposition pattern observed. From the ρ_{ring} plot, it is obvious that the number density of particle at the edge is below 0.1, suggesting the 'ring'-liked pattern is suppressed in a highly-charged system, IM-PMMA in hexane with the magnitude of effective charge Z_{eff} is four times larger than PMMA in dodecane. The configurational entropy due to enhanced entropic and osmotic pressures overcome the evaporation kinetics of the solvent thus the well-structured particles remain unaffected by the fluid flow and less or no migration occured from the droplet centre towards the edge, simultaneously suppressing the 'ring'-liked deposition pattern.

6.3 Surface Charge Neutralization/ Point of Zero Charge (PZC)

The point of zero charge (PZC) was discussed in studies of the flocculation originating from hydrophobic interaction. The term PZC carries the literal meaning of the pH where the surface charge of a particle is zero. For an aqueous solution with electrolyte, the net total charge is developed from the reaction with ionic species and contributed by the charging operations of structural origin $\sigma_{structural}$, adsorbed proton σ_{proton} and adsorbed ion Δq, where $\Delta q = q_+ + q_-$ (Sposito, 1998; Tewari and McLean, 1972). At electroneutrality, the balance of these surface charge contributing species can be expressed as,

$$\sigma_{structural} + \sigma_{proton} + \Delta q = 0 \tag{6.25}$$

For a non-aqueous system with an added electrolyte, the expression can be simplified as $\sigma_s + \Delta q$, where σ_s is the surface charge of the colloid and Δq is the contribution of dissociated ions from the electrolyte or salt. To achieve the PZC, the amount of salt or electrolyte has to be added where $\Delta q = \sigma_s$. The adsorption mechanism of AOT charged micelles was discussed previously and the transition of positively-charged PMMA particles to the zero charge and subsequently to negatively charge particles are depicted in Figures 6.9 and 6.10.

6.3.1 Attraction at Point of Zero Charge (PZC)

In this subchapter, we discuss the effect of particle attractions on the deposition pattern of evaporating colloidal droplet, particularly the effect of addition of AOT, at the surface charge neutralization or point of zero of charge (PZC). We encountered the total suppression of 'ring'-liked pattern when 5mM of AOT was added into PMMA/dodecane suspension as presented in Figure 6.16. From the $\rho_{density}$ plot in Figure 6.12, the particle density at the edge was at a minimum value and obviously below 0.1. Referring to Figure 6.9, the effective charge was at the point of zero charge (PZC), $Z\lambda_B/a \sim 0$. For PMMA in hexane system the PZC was achieved when 5 mM of AOT was added into the system, meanwhile for the highly-charged droplet, IM-PMMA in hexane, we needed about 10 mM of AOT to achieve surface charge neutralization. However the 'ring' pattern suppression due to attraction at PZC was not observed in hexane droplet systems as the interparticle interaction was less effective in hexane droplets. There are a number of physical explanations postulated on the origin of particle attraction at PZC, however the ideal physical explanation has not yet been postulated.

6.3.2 Ion Correlation Effect

The ion correlation effect was postulated as the origin of attraction due to the prediction of the strength of ion-ion correlations on the particle surface. Consider a particle surface, condensed with counterions with the amount of counterions similar to the magnitude of surface charge, when another particle with similar surface decoration comes close to another, the ions on the particle surface can be strongly-correlated. This happens typically when ions are multivalent and the ion-ion interactions are significantly stronger than the ion-particle surface interaction.

Figure 6.17 illustrates a positively-charged particles condensed with counterions on the surface. The strength of ion binding on the surface can be quantified by the electostatic coupling parameter χ,

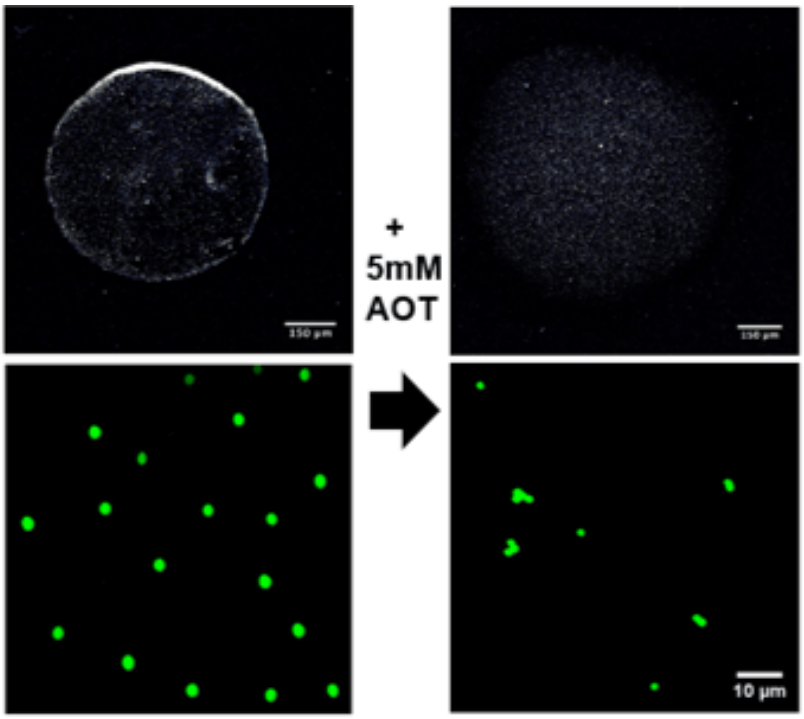

FIGURE 6.16: Deposition of evaporated dodecane droplet containing PMMA and 5mM of AOT (top) and particles attraction observed in the bulk via confocal microscopy (bottom)

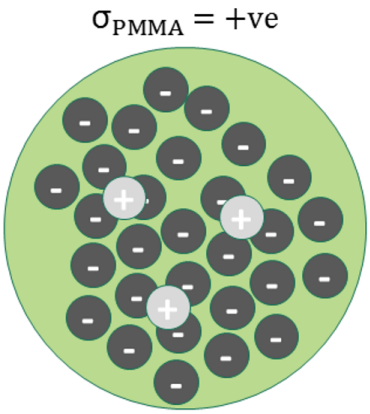

FIGURE 6.17: Presentation of counterions on a particle with positively-charged surface

$$\chi = \frac{q^2 \lambda_B}{\mu_{GC}} = 2\pi q^3 \lambda_b^2 \sigma_s \tag{6.26}$$

where μ_{GC} is the Gouy-Chapman length and σ_s is the surface charge density of a particle. The counterions form clouds, that are bound electrostatically in the vicinity of the macroions and the bound layer containing these counterions on the charged surface is referred to as the Gouy-Chapman length, $\mu_{GC} = \frac{1}{2\pi q \lambda_B \sigma_s}$ which

measures the distance at which the thermal energy k_bT equals to the counterion-wall energy. If μ_{GC} is small, the Bjerrum length is large, indicating that the counterions are strongly bound to the charged surface. This also indicates that χ is large (from equation 6.26), which can be classified as the strong coupling (SC) limit. These counterions in the SC regime ($\chi \geqslant 1$) form a 2d quasi-layer and become laterally correlated, thus inducing attraction between charged particles. From our confocal observations, the argument is valid but we calculate the electrostatic coupling parameter and found $\chi = 0.5$, at all AOT concentrations, which is inadequate to be considered as a strong coupling regime at the PZC where multivalence ions were not present (Naji et al., 2005).

6.3.3 Charge Fluctuations

The Kirkwood Schumaker (KS) theory of charge fluctuations has been a well-known mechanism of electrostatic interactions between proteins in aqueous systems. The charge heterogeneity between two interacting proteins is dependent on dissociation of charge-carrying species on the surface such as nitrogen and carbon, and the reversible protonation of amino acid side groups. The surface net charge is affected by the correlation between the fluctuating monopole charges, which cannot be explained by the fixed charge distribution in the CSC model system (Adžić and Podgornik, 2015). The KS charge fluctuations are analogous to the Casimir effect of the van der Waals forces, which arises from thermal fluctuations of the electromagnetic field when two dielectric surfaces come into a confinement (Klimchitskaya and Mostepanenko, 2015). The surface charge of the macroion is regulated by the surrounding conditions in the solution such as electrostatic potential, salt concentration and the presence of charge bearing entities. The fluctuation interaction is applicable to a system with nonzero capacitance with flexible charge equilibrium and scales as an inverse power of squared of the separation between point of ions (KS $\sim r^{-2}$) while the van der Waals interactions are scaled to the power of six ($U_A \sim r^{-6}$), which only consider the fluctuations of dipoles (Adžić and Podgornik, 2015; Parsegian, 2005).

Imagine two surface charges approaching each other as illustrated in Figure 6.18 with the different surface charge distribution (r_i, Z_i) and (r_j, Z_j), the correlation between two surfaces fluctuating as a form of charge regulation (CR) depending on the separation R between these two surfaces (Adžić and Podgornik, 2015; Lund and Jönsson, 2013). The centre-to-centre separation between these two particles is R and the distance between two charges i and j is $r_{ij} = |R + r_j - r_i|$. We assume a simple dilute ion approach where the interactions are unscreened and the interaction energy can be simply correlated to the Coulomb interaction between two charge interactions,

$$\beta U(R) = \sum_i \sum_j = \frac{\lambda_B Z_i Z_j}{r_{ij}} \tag{6.27}$$

where λ_B is the Bjerrum length and $\beta = (k_B T)^{-1}$ is the electrostatic coupling constant. The electrical capacitance C here can be expressed as,

$$C =< Z^2 > - < Z >^2 \tag{6.28}$$

and C can be defined as the measure of how much can be induced under applied external electrical field. For molecules with titrable sites, the C must be a non-zero value and for identical charge species, the charge is $< Z_i >=< Z_j >=< Z >$. The estimation of free energy is composed of the correlation between two charges (charge-charge) and charge-induced charge and can be written as:

$$\beta A(R) = \frac{\lambda_B < Z >^2}{R} - 2(< Z >^2 + C^2) \tag{6.29}$$

The charge fluctuation is analogous to the van der Waals (vdW) dipole fluctuations, just that in this case, the surface charge regulation results to a fluctuation of particle's monopole, thus the particles could be attracted to each other despite of having similar charge sign. At the PZC, the charge $Z \sim 0$, and the first term (charge-charge correlation) diminishes and the correlation between charge and induced charge becomes dominant, which yields equation 6.29 to:

$$\beta A(R) = \frac{(\lambda_B C)^2}{2R^2} \tag{6.30}$$

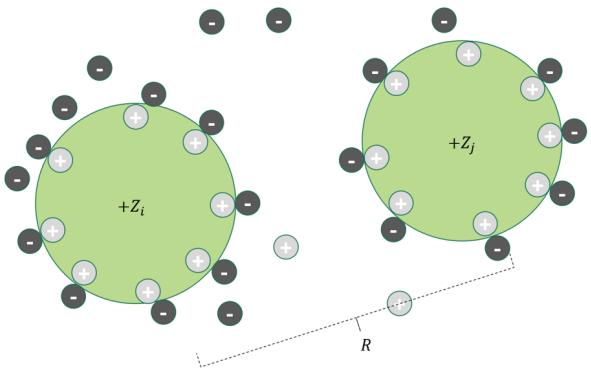

FIGURE 6.18: Presentation of two macroions interacting with charge on the surface fluctuating

6.4 The Effect of TDAT electrolyte on the evaporation of colloidal droplet

In Chapter 3, we used an organic electrolyte, TDAT to alter the electrostatic interactions in a non-polar colloidal system. We discuss the effect of TDAT electrolyte on the deposition pattern of an evaporating colloidal droplet. Deposition patterns of an evaporating colloidal droplets have gained interests from scientists since the 'coffee-ring' phenomenon was first introduced by Deegan in 1997, as this concerns industries in various applications. The effort to suppress the existence of non-uniform deposition patterns are limited not only to modifying physical properties of the contacting droplet and glass substrate but also towards the microscopic level of the formulations and interactions of the whole colloidal system.

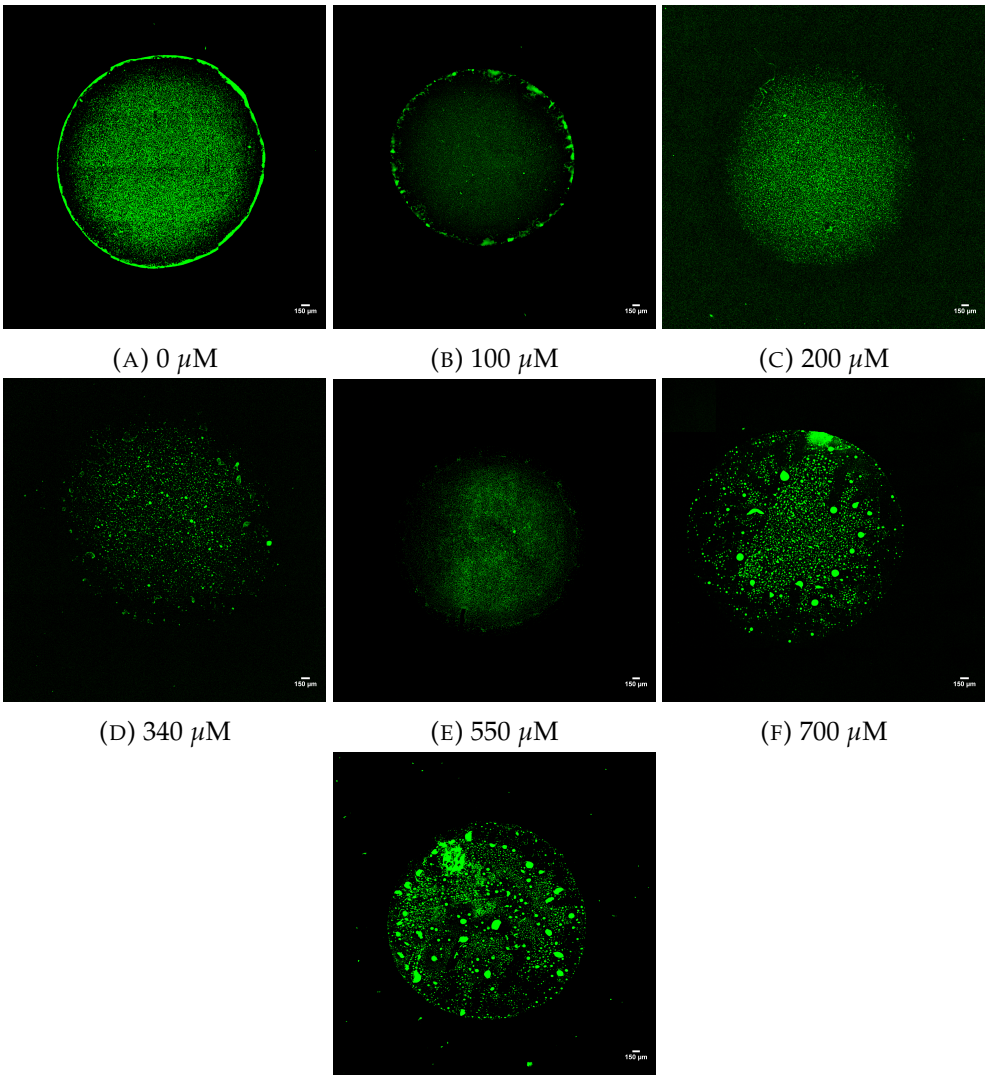

(A) 0 μM (B) 100 μM (C) 200 μM

(D) 340 μM (E) 550 μM (F) 700 μM

(G) 740 μM

FIGURE 6.19: Deposition patterns of evaporated PMMA droplets in dodecane varied with TDAT concentration

Figure 6.19 shows the deposition patterns of dodecane droplets containing PMMA colloids with varied concentration of TDAT. It is obvious that in the system without any TDAT, the deposit formed a fine 'ring' pattern and eventually the 'ring' pattern starts to disappear with increasing TDAT concentration. At about 200 μM of TDAT, a uniform deposition was achieved. When TDAT was added to concentrations more than 650 μM, we observed numerous particle aggregates deposited on the glass substrate. Figure 6.19 presents the particles relative density at the droplet edge, referred as ρ_{ring}. We analyzed the density profile based on percentiles of the overall droplet, where the droplet was divided into ten equivalent radial sections and the ρ_{ring} represents the number density at the droplet edge. If the ρ_{ring} or the density at any part of the droplet = 0.1, a uniform deposition is achieved. Referring to Figure 6.20, in region I, the ρ_{ring} is more than 0.1, indicating that the 'ring' pattern is formed. The 'ring' is surpressed when TDAT was added into the system as presented in regime II. However, the ρ_{ring} starts to develop when TDAT was added at > 650 μM even though the ρ_{ring} < 0.1. This matches with our observation in 6.20. Looking back at Figures 3.2 and 3.6, particle clusters and aggregates formed immediately in bulk solvent when TDAT was added into the system. The ρ_{ring} decreases with TDAT concentration initially owing to the particle clustering formed in the bulk solvent and eventually settled on the glass substrate. At TDAT > 650 μM, the reappearance of the micro-'ring' pattern is mainly due to the particles were weakly repelling each other, interacting at a much shorter range as presented in the force-profile trend in Figure 3.7. Instead, after aggregating in the bulk, the aggregates were compensating the evaporation kinetics and settled locally.

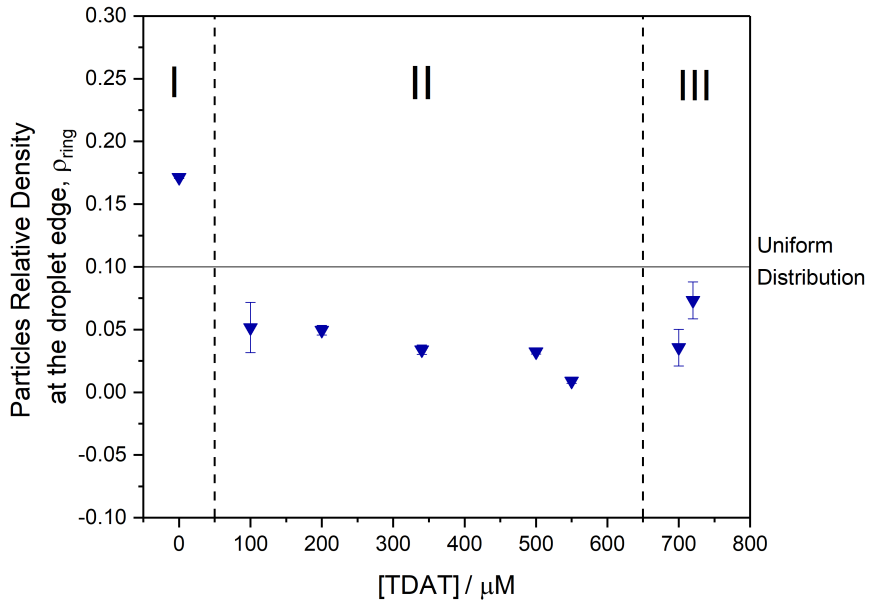

FIGURE 6.20: Particle relative density at droplet edge changes with TDAT concentration

6.5 Summary: Competitive Effect of Solvent Evaporation Kinetics and Interparticle Interactions of Evaporating Colloidal Droplet

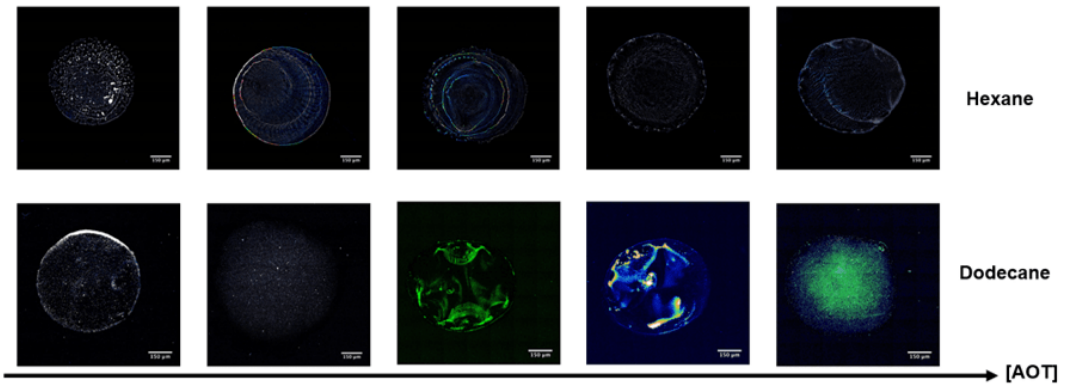

FIGURE 6.21: Phase diagram of droplet deposition pattern changes with [AOT] in both hexane and dodecane

Figure 6.21 shows an overall summary of the competitive effect between evaporation kinetics and interparticle interactions of evaporating colloidal droplets. Evaporation kinetics of the solvent has an influence in controlling the final deposition pattern of evaporating droplets as discussed in Chapter 4. The interparticle interaction suppresses the 'coffee-ring' effect but the study of this effect is limited, especially for non-aqueous droplets. Collectively, there are three main factors affecting the droplet evaporation pattern of non-aqueous colloidal systems combining both evaporation kinetics and particle interaction forces in the bulk droplet. Firstly, the pattern is governed by the evaporation kinetics of the solvent based on the thermodynamic properties of the solvent. The dominance of interparticle forces is lesser when the evaporation kinetics are faster. We can compare the deposition pattern of hexane and dodecane droplets from Figure 6.21 and the concentration of AOT has no effect on the deposition pattern of hexane droplets. This brings us to the second factor which is the contact line mobility. The three-phase contact point is the point where the droplet is pinned and the 'ring'-liked pattern is observed. The addition of AOT adjusts the pinning state of the contact line at the droplet periphery where it reduces the contact line friction, and results in the 'volcano'-shaped pattern and eventually to the 'mountain'-shaped deposition at a high AOT concentration. This effect was observed in dodecane dropletS as presented in Figure 5.19. The intensity of the 'ring' in hexane systems is reduced with AOT concentration as observed in Figure 5.23 and quantitatively analyzed in Figure 5.22a.

The final factor is the interparticle forces which are governed by two interactions underlying the stabilization of colloidal systems, namely electrostatic repulsion and attractions. Most of our work were analyzed in the bulk system and

compared with the observation and analysis made on the surface of the glass substrate. The origin of particle attraction here is not due to the van der Waals interaction but charge fluctuation and dipolar interactions. We found that at extremes of electrostatic repulsion and attraction, for our systems at least, the 'ring' pattern is suppressed and more uniform deposition patterns were observed in systems with less repulsive colloidal interactions. The interparticle repulsion we generated in the hexane system was adequate to suppress the 'ring' pattern but a uniform distribution was not observed. Particle attraction at the point of zero charge was only seen in the dodecane system as it was not sufficient to combat the strong evaporation kinetics of hexane. We postulate that if the attraction between particles in hexane are high enough to overcome the evaporation kinetics of the solvent, the uniform deposition pattern of an evaporating hexane droplet could be achieved as well.

The particle attraction induced by TDAT has effectively influenced the deposition patterns of an evaporating colloidal droplet. The large aggregates formation at very high TDAT concentrations triggered a formation of 'ring'-liked pattern due to a weaker electrostatic interaction between colloids causes the aggregates to settle on a local position, thus favouring the fluid flow upon evaporation process.

Chapter 7

Conclusion

The ubiquitous influence of intercolloidal interactions in industrial processes enabled scientists to explore and modify the practicability of colloidal systems to suit various applications ranging from nano to macroscale processes and manufacturing. This thesis was made up of both fundamental theoretical studies on the colloids interactions in non-aqueous solvents and the implications on the evaporation process, which mainly concerns industries dealing with painting, printing, coating and layering processes.

The magnitude of interparticle repulsion (and attraction) can be manipulated by adding the TDAT electrolyte, AOT surfactant and increasing the surface charge by using ionic monomer particles. These variables effectively alter the electrostatic interactions between colloids differently. Firstly, colloids in the TDAT electrolytic non-aqueous system interacting based on the charge regulation (CR) model. The CR model lies in between the two extremities of charging behaviour, namely the constant surface potential (CSP) and constant surface charge (CSC) models. The AOT-laden colloidal system adapts the CSP model, whereas the highly-charged colloidal system witnesses the CSC model. The magnitude of the long-range interactions between colloids in the bulk liquid was quantified using the blinking optical tweezers (BOT) and imaged using the confocal microscope.

For the electrolytic system, the increasing concentration of TDAT leads to the formation of particle clusters and aggregates. The BOT data revealed the charge instability of the PMMA particles with TDAT concentration, suggesting that the system is adapting the CR model. This is further justified by the preliminary experimental findings on the formation of dipole-like or Janus-like particles. The non-uniform charge distribution on the particle surface becomes more intense with reducing the separation between particles and this drives the formation of colloidal charge patchiness on the hemispheres of the colloids. The formation of dipole-like particle induced particle attractions and consequently affect the deposition pattern of an evaporating colloidal droplet.

We studied the colloidal behaviour in an ionic liquid solution mainly to further investigate the effect of ion concentration on the particle attraction and the screening length, resulted from the experimental findings in the TDAT system. The disagreement between the calculated Debye length and measured screening length in the TDAT system was observed at [TDAT] > 450 μM was not observed in the ionic liquid system, even though the ion concentration in this system is much higher, incomparable to the TDAT system. The cluster and aggregates formation in the ionic liquid colloidal system was incomparable to the TDAT system, with the average number of particles clustered is just ~ 4, whereas, in the TDAT system, the average number of particles clustered together is ~ 100000. The stability of PMMA colloids was achieved at very high ionic liquid concentrations predominantly caused by the slow particle aggregation rate due to the viscosity of the solvent.

The CSP model which adapted by the AOT surfactant-laden colloids fundamentally obeys the classical DLVO theory. In this system, the particle surface charges are altered to adapt to the constant surface potential model. The anionic head of AOT molecules largely affected the charge magnitude of the positively-charged PMMA and IM-PMMA. Charge neutralization was observed as predicted theoretically that the amount of counterions attached on the particle surface is equal to the number of available adsorption sites. Further increase in AOT concentration leads to the charge reversal and this has a large influence on the deposition pattern of the colloidal droplet.

All the above systems were used to observe and analyze the deposition patterns of evaporating colloidal droplets. However, no deposition patterns were studied for the ionic liquid solution system as ionic liquid exists as a liquid at room temperature. The underlying theories of the effect of intercolloidal interactions in the deposition patterns were discussed based on these systems. Importantly, both attraction and repulsion are vital in determining the uniformity of the deposition pattern but above all these interactions, for our systems at least, the evaporation kinetics is always the dominant effect in controlling the deposition pattern. We studied colloidal systems using non-polar solvents by different thermodynamic properties; dodecane and hexane. From the Peclet number calculation, it is known that hexane droplets undergo convective drying and the evaporation of dodecane droplets is diffusion-driven. In the system with convective evaporation, the particles always accumulated at the droplet edge, forming a non-uniform deposition or ring-like pattern. The addition of AOT in dodecane has a dominant effect on both evaporation kinetics and interparticle interactions. The contact line mobility was evidently affected by the concentration of AOT as increasing AOT concentration triggered the contact line mobility, yielding the formation of uniform deposition pattern. However, this phenomenon was not observed in hexane droplets. Finally, the interparticle interactions influenced the deposition differently. In AOT systems, the attraction observed at the charge neutralization point suppressed the formation of the ring-like

pattern. Similarly in TDAT system, where increasing TDAT concentration leading to the formation of larger PMMA aggregates and clusters in dodecane, and this leads to the formation of uniform particle distribution. However, at very high TDAT concentrations, where larger aggregates observed formed in the bulk, a fine and weak ring-like pattern was spotted formed on the glass substrate. On the other hand, when we used the highly-charged particles, IM-PMMA in hexane, the ring-like pattern was suppressed. This shows that both interparticle attraction and repulsion can evidently produce a uniform deposition pattern of an evaporating droplet. We also postulated if the strength of interparticle attraction can be enhanced in the hexane droplets, the uniform deposition pattern could also be achieved.

Bibliography

Adar, Ram M, Tomer Markovich, and David Andelman (2017). "Bjerrum pairs in ionic solutions: A Poisson-Boltzmann approach". In: *The Journal of Chemical Physics* 146.19, p. 194904.

Adžić, Nataša and Rudolf Podgornik (2015). "Charge regulation in ionic solutions: Thermal fluctuations and Kirkwood-Schumaker interactions". In: *Physical Review E* 91.2, p. 022715.

Allahyarov, E et al. (2007). "Interaction between charged colloids in a low dielectric constant solvent". In: *EPL (Europhysics Letters)* 78.3, p. 38002.

Allebrod, Frank et al. (2012). "Electrical conductivity measurements of aqueous and immobilized potassium hydroxide". In: *international journal of hydrogen energy* 37.21, pp. 16505–16514.

Ambrose, D and IJ Lawrenson (1972). "The vapour pressure of water". In: *The Journal of Chemical Thermodynamics* 4.5, pp. 755–761.

Antl, L et al. (1986). "The preparation of poly (methyl methacrylate) latices in non-aqueous media". In: *Colloids and Surfaces* 17.1, pp. 67–78.

Anyfantakis, Manos and Damien Baigl (2015). "Manipulating the Coffee-Ring Effect: Interactions at Work". In: *ChemPhysChem* 16.13, pp. 2726–2734.

Arulanandam, Sarah and Dongqing Li (2000). "Liquid transport in rectangular microchannels by electroosmotic pumping". In: *Colloids and Surfaces A: Physicochemical and Engineering Aspects* 161.1, pp. 89–102.

Ashkin, Arthur (1970). "Acceleration and trapping of particles by radiation pressure". In: *Physical review letters* 24.4, p. 156.

Bahadori, Alireza, Chikezie Nwaoha, and Malcolm William Clark (2013). *Dictionary of oil, gas, and petrochemical processing*. CRC Press.

Barros, Kipton and Erik Luijten (2014). "Dielectric effects in the self-assembly of binary colloidal aggregates". In: *Physical review letters* 113.1, p. 017801.

Behrens, Sven Holger and Michal Borkovec (2000). "Influence of the secondary interaction energy minimum on the early stages of colloidal aggregation". In: *Journal of colloid and interface science* 225.2, pp. 460–465.

Belloni, Luc and Olivier Spalla (1997). "Attraction of electrostatic origin between colloids". In: *The Journal of chemical physics* 107.2, pp. 465–480.

Ben-Naim, Arieh Y (2012). *Hydrophobic interactions*. Springer Science & Business Media.

Bertrand, G et al. (1977). "Characteristic features of the evaporation of liquids". In: *Physics and Chemistry of Liquids* 6.3, pp. 215–224.

Bhardwaj, Rajneesh et al. (2010). "Self-assembly of colloidal particles from evaporating droplets: role of DLVO interactions and proposition of a phase diagram". In: *Langmuir* 26.11, pp. 7833–7842.

Binnemans, Koen (2005). "Ionic liquid crystals". In: *Chemical Reviews* 105.11, pp. 4148–4204.

Bondy, C (1939). "The creaming of rubber latex". In: *Transactions of the Faraday Society* 35, pp. 1093–1108.

Borkovec, Michal and Sven H Behrens (2008). "Electrostatic double layer forces in the case of extreme charge regulation". In: *The Journal of Physical Chemistry B* 112.35, pp. 10795–10799.

Bowen, W Richard and Frank Jenner (1995). "Dynamic ultrafiltration model for charged colloidal dispersions: a Wigner-Seitz cell approach". In: *Chemical Engineering Science* 50.11, pp. 1707–1736.

Bowen, W Richard and Paul M Williams (1996). "The osmotic pressure of electrostatically stabilized colloidal dispersions". In: *Journal of colloid and interface science* 184.1, pp. 241–250.

Cai, Yangjun and Bi-min Zhang Newby (2008). "Marangoni flow-induced self-assembly of hexagonal and stripelike nanoparticle patterns". In: *Journal of the American Chemical Society* 130.19, pp. 6076–6077.

Cameron, Richard L and Golin B Bull (1962). "The thermal diffusivity and thermal conductivity of glacial ice at Wilkes Station, Antarctica". In: *Antarctic Research: The Matthew Fontaine Maury Memorial Symposium*. Vol. 7. Wiley Online Library, pp. 178–184.

Chanamai, Ratjika and D Julian McClements (2000). "Creaming stability of flocculated monodisperse oil-in-water emulsions". In: *Journal of Colloid and Interface Science* 225.1, pp. 214–218.

Chandler, David (2002). "Hydrophobicity: Two faces of water". In: *Nature* 417.6888, p. 491.

Cui, Liying et al. (2012). "Suppression of the coffee ring effect by hydrosoluble polymer additives". In: *ACS applied materials & interfaces* 4.5, pp. 2775–2780.

Dahirel, Vincent and Marie Jardat (2010). "Effective interactions between charged nanoparticles in water: What is left from the DLVO theory?" In: *Current Opinion in Colloid & Interface Science* 15.1-2, pp. 2–7.

Daubert, Thomas E (1989). "Physical and thermodynamic properties of pure chemicals: data compilation". In: *Design Institute for Physacal Property Data (DIPPR)*.

De Gans, B-J, Paul C Duineveld, and Ulrich S Schubert (2004). "Inkjet printing of polymers: state of the art and future developments". In: *Advanced materials* 16.3, pp. 203–213.

Deàk, John C et al. (2004). "Vibrational energy transfer across a reverse micelle surfactant layer". In: *Science* 306.5695, pp. 473–476.

Deegan, Robert D et al. (1997). "Capillary flow as the cause of ring stains from dried liquid drops". In: *Nature* 389.6653, p. 827.

Derby, Brian (2010). "Inkjet printing of functional and structural materials: fluid property requirements, feature stability, and resolution". In: *Annual Review of Materials Research* 40, pp. 395–414.

Dong, Lei (2009). "Dielectric properties of colloidal suspensions". PhD thesis. Teknillinen korkeakoulu: University of Technology Espoo, Finland.

Drioli, Enrico, Alessandra Criscuoli, and Louis Peña Molero (2017). *Membrane distillation*. MDPI.

Dugyala, Venkateshwar Rao and Madivala G Basavaraj (2014). "Control over coffee-ring formation in evaporating liquid drops containing ellipsoids". In: *Langmuir* 30.29, pp. 8680–8686.

Eales, Adam D et al. (2015). "Evaporation of pinned droplets containing polymer–an examination of the important groups controlling final shape". In: *AIChE Journal* 61.5, pp. 1759–1767.

Eicke, Hans Friedrich, Michal Borkovec, and Bikram Das-Gupta (1989). "Conductivity of water-in-oil microemulsions: a quantitative charge fluctuation model". In: *The Journal of Physical Chemistry* 93.1, pp. 314–317.

Eicke, HF and A Denss (1979). "Micellar Catalysis and Concept in Apolar Media". In: *Croatica Chemica Acta* 52.2, pp. 105–113.

Eicke, HF, RFW Hopmann, and H Christen (1975). "Kinetics of conformational change during micelle formation in apolar media". In: *Berichte der Bunsengesellschaft für physikalische Chemie* 79.8, pp. 667–673.

Elimelech, Menachem, John Gregory, and Xiadong Jia (2013). *Particle deposition and aggregation: measurement, modelling and simulation*. Butterworth-Heinemann.

Eral, HB, JM Oh, et al. (2013). "Contact angle hysteresis: a review of fundamentals and applications". In: *Colloid and polymer science* 291.2, pp. 247–260.

Erbil, H Yildirim, Glen McHale, and MI Newton (2002). "Drop evaporation on solid surfaces: constant contact angle mode". In: *Langmuir* 18.7, pp. 2636–2641.

Everett, Douglas H (2007). *Basic principles of colloid science*. Royal society of chemistry.

Finlayson, Samuel (2016a). "A Direct Investigation of Electrostatics in Nonpolar Colloids". PhD thesis. School of Chemistry, University of Bristol.

Finlayson, Samuel D and Paul Bartlett (2016). "Non-additivity of pair interactions in charged colloids". In: *The Journal of chemical physics* 145.3, p. 034905.

Finlayson, Samuel David (2016b). "A direct investigation of electrostatics in nonpolar colloids". An optional note. PhD thesis. University of Bristol: School of Chemistry.

Freemantle, Michael (2010). *An introduction to ionic liquids*. Royal Society of chemistry.

Fuoss, Raymond M and Charles A Kraus (1933a). "Properties of electrolytic solutions. II. The evaluations of $\Lambda 0$ and of K for incompletely dissociated electrolytes". In: *Journal of the American Chemical Society* 55.2, pp. 476–488.

Fuoss, Raymond M and Charles A Kraus (1933b). "Properties of Electrolytic Solutions. IV. The Conductance Minimum and the Formation of Triple Ions Due to the Action of Coulomb Forces1". In: *Journal of the American Chemical Society* 55.6, pp. 2387–2399.

Gebbie, Matthew A et al. (2013). "Ionic liquids behave as dilute electrolyte solutions". In: *Proceedings of the National Academy of Sciences* 110.24, pp. 9674–9679.

Gebbie, Matthew A et al. (2017). "Long range electrostatic forces in ionic liquids". In: *Chemical Communications* 53.7, pp. 1214–1224.

Gillespie, David (2016). "Electrokinetic and Electrostatic Properties of Highly-Charged Colloids in Low Dielectric Media". PhD thesis. School of Chemistry, University of Bristol.

Good, Robert J (1992). "Contact angle, wetting, and adhesion: a critical review". In: *Journal of adhesion science and technology* 6.12, pp. 1269–1302.

Gorski, Nikolai and Yurii M Ostanevich (1990). "Inverted Micelles in a Ternary System AOT-Water-Benzene as Studied by Small-Angle Neutron Scattering". In: *Berichte der Bunsengesellschaft für physikalische Chemie* 94.7, pp. 737–741.

Grier, David G (1997). "Optical tweezers in colloid and interface science". In: *Feb* 5, pp. 264–274.

Guo, Qiong, Virendra Singh, and Sven Holger Behrens (2009). "Electric charging in nonpolar liquids because of nonionizable surfactants". In: *Langmuir* 26.5, pp. 3203–3207.

Guo, Qiong et al. (2013). "Surfactant mediated charging of polymer particles in a nonpolar liquid". In: *Journal of colloid and interface science* 392, pp. 83–89.

Hallett, James E et al. (2018). "Charge regulation of nonpolar colloids". In: *Soft matter* 14.3, pp. 331–343.

Han, Wei and Zhiqun Lin (2012). "Learning from "Coffee Rings": Ordered Structures Enabled by Controlled Evaporative Self-Assembly". In: *Angewandte Chemie International Edition* 51.7, pp. 1534–1546.

Harada, Liliam K et al. (2018). "Insights into Protein-Ionic Liquid Interactions Aiming at Macromolecule Delivery Systems". In: *Journal of the Brazilian Chemical Society* 29.10, pp. 1983–1998.

Hauser, EA and Bradley Dewey Jr. (1941). "Creaming of rubber latex". In: *Industrial & Engineering Chemistry* 33.1, pp. 127–130.

Hendarto, E (2013). *Applications of Marangoni forces in actuating solid phase objects*. University of Michigan: Addison-Wesley.

Hepler, Loren G (1969). "Thermal expansion and structure in water and aqueous solutions". In: *Canadian Journal of Chemistry* 47.24, pp. 4613–4617.

Hieronimus, Reint, Simon Raschke, and Andreas Heuer (2016). "How to model the interaction of charged Janus particles". In: *The Journal of Chemical Physics* 145.6, p. 064303.

Hill, Terrell L (1949). "Statistical mechanics of adsorption. V. Thermodynamics and heat of adsorption". In: *The Journal of Chemical Physics* 17.6, pp. 520–535.

Hiltner, P Anne and Irvin M Krieger (1969). "Diffraction of light by ordered suspensions". In: *The Journal of Physical Chemistry* 73.7, pp. 2386–2389.

Hisatake, Kazuo, Satoko Tanaka, and Youko Aizawa (1993). "Evaporation rate of water in a vessel". In: *Journal of applied physics* 73.11, pp. 7395–7401.

Hoath, Stephen D (2016). *Fundamentals of inkjet printing: the science of inkjet and droplets*. John Wiley & Sons.

Hogg, RTWDW, To Wo Healy, and DW Fuerstenau (1966). "Mutual coagulation of colloidal dispersions". In: *Transactions of the Faraday Society* 62, pp. 1638–1651.

Holmberg, Jenny Perez et al. (2013). "Surface charge and interfacial potential of titanium dioxide nanoparticles: experimental and theoretical investigations". In: *Journal of colloid and interface science* 407, pp. 168–176.

Horwitz, William (1939). "The theory of electrokinetic phenomena". In: *Journal of Chemical Education* 16.11, p. 519.

Hsu, Ming F, Eric R Dufresne, and David A Weitz (2005a). "Charge stabilization in nonpolar solvents". In: *Langmuir* 21.11, pp. 4881–4887.

— (2005b). "Charge stabilization in nonpolar solvents". In: *Langmuir* 21.11, pp. 4881–4887.

Hu, Hua and Ronald G Larson (2006a). "Marangoni effect reverses coffee-ring depositions". In: *The Journal of Physical Chemistry B* 110.14, pp. 7090–7094.

— (2006b). "Marangoni effect reverses coffee-ring depositions". In: *The Journal of Physical Chemistry B* 110.14, pp. 7090–7094.

Huang, Dinghai, Sindee L Simon, and Gregory B McKenna (2005). "Chain length dependence of the thermodynamic properties of linear and cyclic alkanes and polymers". In: *The Journal of chemical physics* 122.8, p. 084907.

Hunt, Patricia A, Ian R Gould, and Barbara Kirchner (2007). "The structure of imidazolium-based ionic liquids: Insights from ion-pair interactions". In: *Australian journal of chemistry* 60.1, pp. 9–14.

Hunter, Robert J (2013). *Zeta potential in colloid science: principles and applications*. Vol. 2. Academic press.

Hussain, Ghulam, Amy Robinson, and Paul Bartlett (2013). "Charge generation in low-polarity solvents: poly (ionic liquid)-functionalized particles". In: *Langmuir* 29.13, pp. 4204–4213.

Huyskens, Pierre L, Werner AP Luck, and Therese Zeegers-Huyskens (2012). *Intermolecular forces: an introduction to modern methods and results*. Springer Science & Business Media.

Hynninen, Antti-Pekka, Marjolein Dijkstra, and Athanassios Z Panagiotopoulos (2005). "Critical point of electrolyte mixtures". In: *The Journal of chemical physics* 123.8, p. 084903.

Israelachvili, Jacob N (2011). *Intermolecular and surface forces*. Academic press.

Jayaram, B (1994). "Free Energy of Solvation, Interaction, and Binding of Arbitrary Charge Distributions Imbedded in a Dielectric Continuum". In: *The Journal of Physical Chemistry* 98.22, pp. 5773–5777.

Kadokawa, Jun-ichi (2013). "Polymerizable ionic liquids: Development to photo functional poly (ionic liquid) materials". In: *Short Topic: More ways to use reagents*, p. 2.

Kavehpour, Pirouz, Ben Ovryn, and Gareth H McKinley (2002). "Evaporatively-driven Marangoni instabilities of volatile liquid films spreading on thermally conductive substrates". In: *Colloids and Surfaces A: Physicochemical and Engineering Aspects* 206.1-3, pp. 409–423.

Keir, Roland I et al. (2002). "Charging behavior in the silica/Aerosol OT/decane system". In: *Langmuir* 18.5, pp. 1463–1465.

Khan, Ibrahim, Khalid Saeed, and Idrees Khan (2017). "Nanoparticles: Properties, applications and toxicities". In: *Arabian Journal of Chemistry*.

Kitahara, Ayao (1998). "Nonaqueous systems". In: *Surfactant science series*, pp. 135–150.

Klimchitskaya, Galina L and Vladimir M Mostepanenko (2015). "Casimir and van der Waals forces: Advances and problems". In: *arXiv preprint arXiv:1507.02393*.

Kobayashi, Motoyoshi et al. (2005). "Aggregation and charging of colloidal silica particles: effect of particle size". In: *Langmuir* 21.13, pp. 5761–5769.

Kölle, Philipp and Richard Dronskowski (2004). "Synthesis, crystal structures and electrical conductivities of the ionic liquid compounds butyldimethylimidazolium tetrafluoroborate, hexafluorophosphate and hexafluoroantimonate". In: *European Journal of Inorganic Chemistry* 2004.11, pp. 2313–2320.

Koo, HS et al. (2006). "Fabrication and chromatic characteristics of the greenish LCD colour-filter layer with nano-particle ink using inkjet printing technique". In: *Displays* 27.3, pp. 124–129.

Kraus, Charles A and Raymond M Fuoss (1933). "Properties of Electrolytic Solutions. I. Conductance as Influenced by the Dielectric Constant of the Solvent Medium1". In: *Journal of the American Chemical Society* 55.1, pp. 21–36.

Kumar, Deepak and Sanjay Kumar Biswas (2008). "Microscopic frictional response of sodium oleate self-assembled on steel". In: *Tribology Letters* 30.3, pp. 199–204.

Kumar, Deepak, Abhay Singh, and Devesh K Mishra (2016). "Role of surfactant head group and chain length in aqueous lubrication: Steel- steel contact". In: *Proceedings of the Institution of Mechanical Engineers, Part J: Journal of Engineering Tribology* 230.8, pp. 968–973.

Lebedev-Stepanov, Peter and Konstantin Vlasov (2013). "Simulation of self-assembly in an evaporating droplet of colloidal solution by dissipative particle dynamics". In: *Colloids and Surfaces A: Physicochemical and Engineering Aspects* 432, pp. 132–138.

Lee, Alpha A et al. (2014). "Are room-temperature ionic liquids dilute electrolytes?" In: *The journal of physical chemistry letters* 6.1, pp. 159–163.

Lekkerkerker, Henk NW and Remco Tuinier (2011). "Depletion interaction". In: *Colloids and the Depletion Interaction*. Springer, pp. 57–108.

Li, Dongqing (2004). *Electrokinetics in microfluidics*. Vol. 2. Elsevier.

Li, Yuanhang et al. (2015). "Hybridization-induced suppression of coffee ring effect for nucleic acid detection". In: *Sensors and Actuators B: Chemical* 206, pp. 56–64.

Li, Yueh-Feng, Yu-Jane Sheng, and Heng-Kwong Tsao (2013). "Evaporation stains: suppressing the coffee-ring effect by contact angle hysteresis". In: *Langmuir* 29.25, pp. 7802–7811.

Light, Truman S et al. (2005). "The fundamental conductivity and resistivity of water". In: *Electrochemical and Solid-State Letters* 8.1, E16–E19.

Lindell, Ismo V (1992). "Electrostatic image theory for the dielectric sphere". In: *Radio Science* 27.1, pp. 1–8.

Love, John D (1977). "On the van der Waals force between two spheres or a sphere and a wall". In: *Journal of the Chemical Society, Faraday Transactions 2: Molecular and Chemical Physics* 73.5, pp. 669–688.

Lund, Mikael and Bo Jönsson (2013). "Charge regulation in biomolecular solution". In: *Quarterly reviews of biophysics* 46.3, pp. 265–281.

Lyklema, Johannes (2005). *Fundamentals of interface and colloid science: soft colloids*. Vol. 5. Elsevier.

Majer, Vladimír, Václav Svoboda, and Henry V Kehiaian (1985). *Enthalpies of vaporization of organic compounds: a critical review and data compilation*. Vol. 32. Blackwell Scientific Oxford.

Mampallil, Dileep and Huseyin Burak Eral (2018). "A review on suppression and utilization of the coffee-ring effect". In: *Advances in colloid and interface science* 252, pp. 38–54.

Man, Xingkun and Masao Doi (2016). "Ring to mountain transition in deposition pattern of drying droplets". In: *Physical review letters* 116.6, p. 066101.

Manning, Gerald S (1972). "On the application of polyelectrolyte "limiting laws" to the helix-coil transition of DNA. I. Excess univalent cations". In: *Biopolymers: Original Research on Biomolecules* 11.5, pp. 937–949.

Margielewski, L and S Płaza (2010). "Surfactant dithiophosphates lubricating oil additives". In: *Tribology-Materials, Surfaces & Interfaces* 4.2, pp. 43–53.

Martin, Maurice L and JC Youings (1980). "Vapour pressures and excess Gibbs free energies of cyclohexane+ n-hexane,+ n-heptane and+ n-octane at 298. 150 K". In: *Australian Journal of Chemistry* 33.10, pp. 2133–2138.

Martín-Badosa, Estela et al. (2007). "Design strategies for optimizing holographic optical tweezers set-ups". In: *Journal of optics A: pure and applied optics* 9.8, S267.

Masliyah, Jacob H and Subir Bhattacharjee (2006). *Electrokinetic and colloid transport phenomena*. John Wiley & Sons.

Mavroyannis, C and MJ Stephen (1962). "Dispersion forces". In: *Molecular Physics* 5.6, pp. 629–638.

Meyer, Emily E, Kenneth J Rosenberg, and Jacob Israelachvili (2006). "Recent progress in understanding hydrophobic interactions". In: *Proceedings of the National Academy of Sciences* 103.43, pp. 15739–15746.

Miller, John F, Klaus Schätzel, and Brian Vincent (1991). "The determination of very small electrophoretic mobilities in polar and nonpolar colloidal dispersions using phase analysis light scattering". In: *Journal of colloid and interface science* 143.2, pp. 532–554.

Mitchell, DJ and BW Ninham (1972). "Van der Waals forces between two spheres". In: *The Journal of Chemical Physics* 56.3, pp. 1117–1126.

Molesa, Steven et al. (2003). "High-quality inkjet-printed multilevel interconnects and inductive components on plastic for ultra-low-cost RFID applications". In: *MRS Online Proceedings Library Archive* 769.

Morrison, Ian D (1993). "Electrical charges in nonaqueous media". In: *colloids and surfaces A: Physicochemical and engineering aspects* 71.1, pp. 1–37.

Nagata, Yuki, Kota Usui, and Mischa Bonn (2015). "Molecular mechanism of water evaporation". In: *Physical review letters* 115.23, p. 236102.

Naji, Ali et al. (2005). "Electrostatic interactions in strongly coupled soft matter". In: *Physica A: Statistical Mechanics and its Applications* 352.1, pp. 131–170.

Nguyen, Van X and Kathleen J Stebe (2002). "Patterning of small particles by a surfactant-enhanced Marangoni-Bénard instability". In: *Physical Review Letters* 88.16, p. 164501.

Ninham, Barry W and V Adrian Parsegian (1971). "Electrostatic potential between surfaces bearing ionizable groups in ionic equilibrium with physiologic saline solution". In: *Journal of Theoretical Biology* 31.3, pp. 405–428.

Ohno, Hiroyuki, Masahiro Yoshizawa, and Wataru Ogihara (2004). "Development of new class of ion conductive polymers based on ionic liquids". In: *Electrochimica Acta* 50.2-3, pp. 255–261.

Ohshima, Hiroyuki (2006a). *Theory of colloid and interfacial electric phenomena*. Vol. 12. Elsevier.

— (2006b). *Theory of colloid and interfacial electric phenomena*. Vol. 12. Elsevier.

Ohshima, Hiroyuki and Kunio Furusawa (1998). *Electrical phenomena at interfaces, Second Edition*. Vol. 76. Marcel Dekker.

Oldham, Keith B (2008). "A Gouy–Chapman–Stern model of the double layer at a (metal)/(ionic liquid) interface". In: *Journal of Electroanalytical Chemistry* 613.2, pp. 131–138.

Papancea, A, S Patachia, and A Porzsolt (2015). "Conductivity studies of imidazolium-based ionic liquids in aqueous solution". In: *Bulletin of the Transilvania University of Brasov. Engineering Sciences. Series I* 8.1, p. 67.

Parent, Mary E et al. (2011). "Influence of surfactant structure on reverse micelle size and charge for nonpolar electrophoretic inks". In: *Langmuir* 27.19, pp. 11845–11851.

Paria, Santanu and Kartic C Khilar (2004). "A review on experimental studies of surfactant adsorption at the hydrophilic solid–water interface". In: *Advances in colloid and interface science* 110.3, pp. 75–95.

Park, Jungho and Jooho Moon (2006). "Control of colloidal particle deposit patterns within picoliter droplets ejected by ink-jet printing". In: *Langmuir* 22.8, pp. 3506–3513.

Parsegian, V Adrian (2005). *Van der Waals forces: a handbook for biologists, chemists, engineers, and physicists*. Cambridge University Press.

Pérez-Rodríguez, Martín et al. (1998). "A comparative study of the determination of the critical micelle concentration by conductivity and dielectric constant measurements". In: *Langmuir* 14.16, pp. 4422–4426.

Perkin, Susan (2012). "Ionic liquids in confined geometries". In: *Physical Chemistry Chemical Physics* 14.15, pp. 5052–5062.

Prabhu, K Narayan, Peter Fernades, and Girish Kumar (2009). "Effect of substrate surface roughness on wetting behaviour of vegetable oils". In: *Materials & design* 30.2, pp. 297–305.

Rana, Suman et al. (2017). "Interfacial engineering of nanoparticles for cancer therapeutics". In: *Nanostructures for Cancer Therapy*. Elsevier, pp. 177–209.

Rashin, Alexander A and Barry Honig (1985). "Reevaluation of the Born model of ion hydration". In: *J. Phys. Chem* 89.26, pp. 5588–5593.

Reid, Jonathan P et al. (2018). "The viscosity of atmospherically relevant organic particles". In: *Nature communications* 9.1, p. 956.

Roberts, G Seth et al. (2008). "Electrostatic charging of nonpolar colloids by reverse micelles". In: *Langmuir* 24.13, pp. 6530–6541.

Roij, René van (2000). "Attraction or repulsion between charged colloids? A connection with Debye-Hückel theory". In: *Journal of Physics: Condensed Matter* 12.8A, A263.

Russel, William Bailey et al. (1991). *Colloidal dispersions*. Cambridge university press.

Rydberg, Jan (2004). *Solvent extraction principles and practice, revised and expanded*. CRC Press.

Ryu, Seul-a et al. (2017). "Drying-mediated patterns in colloid-polymer suspensions". In: *Scientific Reports* 7.1, p. 1079.

Salazar, Agustin (2003). "On thermal diffusivity". In: *European journal of physics* 24.4, p. 351.

Schellman, John A and Dirk Stigter (1977). "Electrical double layer, zeta potential, and electrophoretic charge of double-stranded DNA". In: *Biopolymers: Original Research on Biomolecules* 16.7, pp. 1415–1434.

Schindelin, Johannes et al. (2012). "Fiji: an open-source platform for biological-image analysis". In: *Nature methods* 9.7, p. 676.

Schirru, Michele (2017). *Development of an Ultrasonic Sensing Technique to Measure Lubricant Viscosity in Engine Journal Bearing In-Situ*. Springer.

Schneider, Caroline A, Wayne S Rasband, and Kevin W Eliceiri (2012). "NIH Image to ImageJ: 25 years of image analysis". In: *Nature methods* 9.7, p. 671.

Schröer, Wolffram (2001). "Generalization of the Kirkwood-Fröhlich theory of dielectric polarization for ionic fluids". In: *Journal of Molecular Liquids* 92.1-2, pp. 67–76.

Scriven, LE and CV Sternling (1960). "The marangoni effects". In: *Nature* 187.4733, p. 186.

Sen, D et al. (2012). "Nanocomposite silica surfactant microcapsules by evaporation induced self assembly: tuning the morphological buckling by modifying viscosity and surface charge". In: *Soft Matter* 8.6, pp. 1955–1963.

Seo, Changdeok et al. (2017). "Altering the coffee-ring effect by adding a surfactant-like viscous polymer solution". In: *Scientific reports* 7.1, p. 500.

Shanks, PC and EI Franses (1992). "Estimation of micellization parameters of aqueous sodium dodecyl sulfate from conductivity data". In: *The Journal of Physical Chemistry* 96.4, pp. 1794–1805.

Singh, Harjinder (2004). "Heat stability of milk". In: *International Journal of Dairy Technology* 57.2-3, pp. 111–119.

Smith, Alexander M, Alpha A Lee, and Susan Perkin (2016). "The electrostatic screening length in concentrated electrolytes increases with concentration". In: *The journal of physical chemistry letters* 7.12, pp. 2157–2163.

Smith, Gregory N et al. (2013). "Evidence for a critical micelle concentration of surfactants in hydrocarbon solvents". In: *Langmuir* 29.10, pp. 3252–3258.

Smith, Gregory N et al. (2015). "Surfactants with colloids: Adsorption or absorption?" In: *Journal of colloid and interface science* 449, pp. 205–214.

Smith, Gregory N et al. (2017). "Electrolyte-induced Instability of Colloidal Dispersions in Nonpolar Solvents". In: *The journal of physical chemistry letters* 8.19, pp. 4668–4672.

Soltman, Dan and Vivek Subramanian (2008). "Inkjet-printed line morphologies and temperature control of the coffee ring effect". In: *Langmuir* 24.5, pp. 2224–2231.

Sposito, Garrison (1998). "On points of zero charge". In: *Environmental science & technology* 32.19, pp. 2815–2819.

Stigter, D and KJ Mysels (1955). "Tracer electrophoresis. II. The mobility of the micelle of sodium lauryl sulfate and its interpretation in terms of zeta potential and charge". In: *The Journal of Physical Chemistry* 59.1, pp. 45–51.

Still, Tim, Peter J Yunker, and Arjun G Yodh (2012). "Surfactant-induced Marangoni eddies alter the coffee-rings of evaporating colloidal drops". In: *Langmuir* 28.11, pp. 4984–4988.

Strubbe, Filip et al. (2006). "Generation current of charged micelles in nonaqueous liquids: Measurements and simulations". In: *Journal of colloid and interface science* 300.1, pp. 396–403.

Swartzen-Allen, S Lee and Egon Matijevic (1974). "Surface and colloid chemistry of clays". In: *Chemical Reviews* 74.3, pp. 385–400.

Szilagyi, Istvan et al. (2014). "Particle aggregation mechanisms in ionic liquids". In: *Physical Chemistry Chemical Physics* 16.20, pp. 9515–9524.

Tanford, Charles (1962). "Contribution of hydrophobic interactions to the stability of the globular conformation of proteins". In: *Journal of the American Chemical Society* 84.22, pp. 4240–4247.

— (1980). *The hydrophobic effect: formation of micelles and biological membranes 2d ed*. J. Wiley.

Tewari, PH and AW McLean (1972). "Temperature dependence of point of zero charge of alumina and magnetite". In: *Journal of Colloid and Interface Science* 40.2, pp. 267–272.

Thomas, P, RS Ernest Ravindran, and KBR Varma (2012). "Dielectric properties of Poly (methyl methacrylate)(PMMA)/CaCu 3 Ti 4 O 12 composites". In: *2012 IEEE 10th International Conference on the Properties and Applications of Dielectric Materials*. IEEE, pp. 1–4.

Tokuda, Hiroyuki et al. (2006). "How ionic are room-temperature ionic liquids? An indicator of the physicochemical properties". In: *The Journal of Physical Chemistry B* 110.39, pp. 19593–19600.

Torres-Chavolla, Edith and Evangelyn C Alocilja (2009). "Aptasensors for detection of microbial and viral pathogens". In: *Biosensors and bioelectronics* 24.11, pp. 3175–3182.

Träuble, Hermann et al. (1976). "Electrostatic interactions at charged lipid membranes: I. Effects of pH and univalent cations on membrane structure". In: *Biophysical chemistry* 4.4, pp. 319–342.

Tuinier, R, J Rieger, and CG De Kruif (2003). "Depletion-induced phase separation in colloid–polymer mixtures". In: *Advances in colloid and interface science* 103.1, pp. 1–31.

Ueno, Kazuhide and Masayoshi Watanabe (2011). "From colloidal stability in ionic liquids to advanced soft materials using unique media". In: *Langmuir* 27.15, pp. 9105–9115.

Valeriani, Chantal et al. (2010). "Ion association in low-polarity solvents: comparisons between theory, simulation, and experiment". In: *Soft Matter* 6.12, pp. 2793–2800.

Verwey, EJW and J Th G Overbeek (1948). "Theory of the Stability of Hydrophobic Colloids Elsevier". In: *New York, NY*.

Visser, J (1972). "On Hamaker constants: A comparison between Hamaker constants and Lifshitz-van der Waals constants". In: *Advances in colloid and interface science* 3.4, pp. 331–363.

Vold, Marjorie J (1982). *Zeta potential in colloid science. Principles and applications: By RJ Hunter, Academic Press, New York/London. 386 pp.* 84.00.

Waggett, Franceska (2019). "Direct Measurement of Electrostatic Forces between Colloids". PhD thesis. School of Chemistry, University of Bristol.

Waggett, Franceska, Mohamad Shafiq, and Paul Bartlett (2018). "Failure of Debye-Hückel Screening in Low-Charge Colloidal Suspensions". In: *Colloids and Interfaces* 2.4, p. 51.

Wang, Haizhong et al. (2004). "Friction and wear behaviors of ionic liquid of alkylimidazolium hexafluorophosphates as lubricants for steel/steel contact". In: *Wear* 256.1-2, pp. 44–48.

Washburn, Edward W (1921). "The dynamics of capillary flow". In: *Physical review* 17.3, p. 273.

Wellens, Sil (2014). "Ionic liquid technology in metal refining: Dissolution of metal oxides and separation by solvent extraction". PhD thesis. Katholieke University Leuven, Belgium.

Wen, Jessica T, Chih-Ming Ho, and Peter B Lillehoj (2013). "Coffee ring aptasensor for rapid protein detection". In: *Langmuir* 29.26, pp. 8440–8446.

Yamamuro, Osamu et al. (2006). "Heat capacity and glass transition of an ionic liquid 1-butyl-3-methylimidazolium chloride". In: *Chemical physics letters* 423.4-6, pp. 371–375.

Yuan, Yuehua and T Randall Lee (2013). "Contact angle and wetting properties". In: *Surface science techniques*. Springer, pp. 3–34.

Yunker, Peter J et al. (2011a). "Suppression of the coffee-ring effect by shape-dependent capillary interactions". In: *Nature* 476.7360, p. 308.

— (2011b). "Suppression of the coffee-ring effect by shape-dependent capillary interactions". In: *Nature* 476.7360, p. 308.

Yushkevich, V Yu, IN Maksimova, and VG Bullan (1967). "Electrical conductivity of potassium hydroxide solutions at high temperatures". In: *Elektrokhimiya* 3, pp. 1491–3.

Zakerhamidi, MS et al. (2010). "Isotropic and anisotropic environment effects on the UV/vis absorption spectra of three disperse azo dyes". In: *Journal of Molecular Liquids* 154.2-3, pp. 94–101.

Zhang, Lei et al. (2012). "Inkjet printing high-resolution, large-area graphene patterns by coffee-ring lithography". In: *Advanced Materials* 24.3, pp. 436–440.

Zhang, Peng, Qingbai Wu, and Cuicui Mu (2017). "Influence of temperature on methane hydrate formation". In: *Scientific reports* 7.1, p. 7904.

Zhao, Xiucai, Martin J Blunt, and Jun Yao (2010). "Pore-scale modeling: Effects of wettability on waterflood oil recovery". In: *Journal of Petroleum Science and Engineering* 71.3-4, pp. 169–178.